Ultrasound Elastography for Intra-Operative Use and Renal Tissue Imaging

by

Caitlin Marie Schneider

B.Sc., Johns Hopkins University, 2009

M.A.Sc., The University of British Columbia, 2011

A THESIS SUBMITTED IN PARTIAL FULFILLMENT
OF THE REQUIREMENTS FOR THE DEGREE OF

Doctor of Philosophy

in

THE FACULTY OF GRADUATE AND POSTDOCTORAL STUDIES

(Electrical and Computer Engineering)

The University of British Columbia

(Vancouver)

April 2017

Abstract

The kidney is a vital organ within the human body and improvements in the ability to characterize the kidney tissue can create benefits for patients with kidney tumours and for kidney transplant recipients. Often, changes in tissue health or development of cancer are manifested in changes in tissue structure that affect tissue elastic properties. For example, the cancerous tissue of renal cell carcinoma is stiffer than healthy kidney tissue, and the development of fibrosis, which impairs kidney function, also causes the tissue to become stiffer over time. These changes can be imaged with ultrasound elastography, a technique for quantitatively assessing tissue elasticity. If proven effective, elastography tissue characterization can replace biopsy.

The ultrasound elastography method used in this thesis, called Shear Wave Absolute Vibro-Elastography, or SWAVE, measures the wavelength of induced steady-state multi-frequency mechanical shear waves to calculate tissue elasticity. SWAVE can employ standard ultrasound transducers that image the kidney though the skin above the organ, or custom miniaturized transducers that are placed directly on the surface of the organ during surgery. The accuracy of SWAVE is vastly improved by the use of 3D ultrasound data.

We propose and evaluate 3D SWAVE imaging based on the use of a tracked intra-operative ultrasound transducer designed for use with the da Vinci Robot. Different tracking methods are evaluated for future intra-operative use. Elasticity images of tissue phantoms are obtained using interpolated 3D tissue displacement data acquired with the da Vinci robot and the intra-operative transducer. The use of tracked ultrasound transducer opens the way for introducing registered preoperative imaging, including elastography, to improve surgical guidance.

Different methods of characterizing kidney tissue using SWAVE imaging are examined. The elastic and viscous properties are estimated kidney tissue *ex-vivo*. The effect of arterial pressure on the measured kidney elasticity is characterized. It was found that increasing input pressure increases the measured elasticity. Finally, ultrasound and ultrasound elastography are applied to kidney transplant recipients *in-vivo* to assess the level of fibrosis development. A preliminary study indicates that it is possible to transmit shear waves into the transplanted kidney and measure the elastic properties of the kidney tissue.

Preface

A version of the material presented in Chapter 2 was published as:

> Caitlin Schneider, Christopher Nguan, Robert Rohling, Septimiu Salcudean. "Tracked 'Pick-up' Ultrasound for Robot-assisted Minimally Invasive Surgery". *IEEE Transactions on Biomedical Engineering*, 63 (2), 2016.

I was responsible for all the data collection and analysis. Drs Nguan, Rohling and Salcudean advised on data analysis and manuscript editing.

The material presented in Section 3.3 is based on material orally presented at and in the proceedings of the Medical Image Computation and Computer Aided Interventions (MICCAI) conference as:

> Caitlin Schneider, Ali Baghani, Robert Rohling, Septimiu Salcudean. "Remote ultrasound palpation for robotic interventions using absolute elastography". MICCAI LNCS: Vol. 7510, 2012.

For this publication, I was responsible for the integration of the robot API code into the elastography scanning system, data collection and analysis. Dr. Ali Baghani worked on the development of the phasor fitting and Local Frequency Estimation (LFE) C++ and CUDA code, and all authors contributed to the manuscript editing.

The second experiment described in Chapter 3, Section 3.4 has been submitted and is in process:

Caitlin Schneider, Christopher Nguan, Jeff Abeysekera, Julio Lobo, Robert Rohling, Septimiu Salcudean. "Intra-operative shear wave elastic imaging for robotic interventions".

I was responsible for all the integration between the dVRK (da Vinci robot software) and the current elastography software (eScan). Jeff Abeysekera and Julio Lobo wrote the elastography software. I completed all the data collection and analysis, as well as writing the manuscript. Drs Salcudean and Rohling supervised and edited the manuscript.

Chapter 5 contains material that was presented at two conferences in 2016. Section 5.4 contains material presented as:

Caitlin Schneider, Julio Lobo, Mohammad Honarvar, Samir Bidur, Robert Rohling, Septimiu Salcudean. "Blood Pressure Dependent Elasticity Measurements of Porcine Kidney *ex-vivo*". *IEEE Ultrasonics, Ferroelectrics and Frequency Control, International Ultrasonics Symposium*. 2016.

I was responsible for the coordination of the kidney harvesting and assisted by Samir Bidur. I completed all the data collection, while Julio Lobo and Mohammad Honarvar wrote and developed the elastography software. Drs Nguan, Rohling and Salcudean advised on data analysis and manuscript editing.

The second half of Chapter 5 contains material that as:

Caitlin Schneider, Mohammad Honarvar, Robert Rohling, Septimiu Salcudean, Christopher Nguan. "Apparatus for Imaging and Model Fitting of *ex-vivo* Porcine Kidney". *Fifteenth International Tissue Elasticity Conference*.

Mohammad Honarvar constructed the apparatus for holding the *ex-vivo* kidney and processed the Finite Element Model (FEM) results. I was responsible for the experimental design, kidney harvest, data collection, processing the results for the LFE method and data analysis. Drs Nguan, Rohling and Salcudean advised on data analysis and manuscript editing.

Table of Contents

List of Tables

List of Figures

Glossary

API Application Programming Interface

ARFI Acoustic Radiation Force Impulse

BMI Body Mass Index

CAD Chronic Allograft Dysfunction

CAN Chronic Allograft Nephropathy

CT Computed Tomography

DOF Degree of Freedom

DVRK da Vinci Research Kit

ECG Electrocardiogram

EGFR Estimated Glomerular Filtration Rate

EM Electromagnetic

ESRD End Stage Renal Disease

FEM Finite Element Model

GFR Glomerular Filtration Rate

ICP Iterative Closest Point

IF/TA Interstitial Fibrosis and Tubular Atrophy

IR LED Infrared Light Emitting Diode

LED Light Emitting Diode

LFE Local Frequency Estimation

MAP Mean Arterial Pressure

MIS Minimally Invasive Surgery

MRE Magnetic Resonance Elastography

MRI Magnetic Resonance Imaging

PCA Principal Component Analysis

PLUS Public Library of Ultrasound

PRA Point Reconstruction Accuracy

RF Radio Frequency

SWAVE Shear Wave Absolute Vibro-Elastography

SDK Software Development Kit

SDUV Shearwave Dispersion Ultrasound Vibrometry

SSI SuperSonic Imagine

TLE Target Localization Error

TRE Target Registration Error

VGH Vancouver General Hospital

VISR Viscoelastic Response

VTIQ Virtual Touch Image Quantification

Acknowledgments

The mountains are calling and I must go, and I will work on while I can, studying incessantly.

–John Muir

I would like to acknowledge all the help that I have received throughout the years of my PhD. My supervisors, Tim, Rob and Chris have provided me with valuable guidance during the course of my journey. My friends in the RCL lab were always there if I needed help with experiments, a good idea, or just someone to talk to. My friends in the outdoors taught me to take a break and get a new look at the world. I would like to thank my family, whose continuous motivation kept me going. I could not have made it without each of you.

Chapter 1

Introduction

1.1 Overview and Motivation

This thesis takes a comprehensive look at how to improve the characterization of kidney tissue through the application of ultrasound imaging and elastography of the kidney. There are multiple clinical applications for this work. The first application in which tissue characterization can improve clinical outcomes and surgical workflow is during kidney cancer identification and removal. In order to accomplish this goal, a miniaturized ultrasound transducer used for intra-operative imaging was developed and characterized. With this transducer, 3D ultrasound and elastography volumes can be produced for surgical guidance for robotic-assisted Minimally Invasive Surgery (MIS) procedures. The other major clinical application revolves around measurement of progressive kidney Interstitial Fibrosis and Tubular Atrophy (IF/TA) in kidney transplants, also known as Chronic Allograft Nephropathy (CAN), which is the leading cause of long term graft failure. The monitoring and measurement of CAN, through the use of ultrasound elastography, could provide insight into graft health and potentially lead to changes in treatment that would prolong graft life without the need for additional biopsies of the kidney.

1.2 The Kidney

1.2.1 Kidney Anatomy

The kidneys are a paired organ that are responsible for filtering the blood of ions and proteins, regulating the water content in the body and creating urine to remove waste from the body. The kidney also plays a role in the release of hormones, such as renin. The kidney is approximately 5 cm long, 3 cm wide and 2 cm thick. The kidneys sit under the liver and diaphragm respectively and are attached to the aorta and vena cava through the renal artery and vein. Although they seem to be located inside the abdomen, they are outside, anterior, of the abdominal wall. At any given time, the blood flow into the kidney is equal to approximately 25% of the cardiac output [82].

The kidney is composed of a three different sections: the kidney cortex (the outside of the kidney), the medulla (the middle of the kidney) and the collecting system (the internal section of the kidney). Figure 1.1 illustrates each of the structures mentioned. The cortex is the outside of the kidney and is the upper end of the nephrons, the functioning units of the kidney. The lower ends of the nephrons form pyramidal structures known as the medulla. The vertex of each pyramid terminates in the minor calyx, and the numerous minor calyces expand into two or three major calyces. The collecting system, made up of the minor and major calyces, collects the urine from the pyramids and pools it in the renal pelvis before sending it down the ureter to the bladder. The collecting system is lined by thicker connective tissue that appears as hyperechoic on ultrasound images.

The nephron is the functioning unit of the kidney, and is made up of loops that originate in the cortex and descend into the medulla. Its structure and function are illustrated in Figure 1.2. The blood is first filtered by the nephron at the glomerulus, a bundle of small vessels enclosed in a capsule, called Bowman's capsule. Further filtering and chemical exchanges take place in the ascending and descending Henle's loops. The measured amount of creatinine (a substance created by the muscles) in the blood and/or the urine, along with the patients physical characteristics is a commonly used way to estimate the filtration rate of the kidneys. The Estimated Glomerular Filtration Rate (EGFR) is used as a way to track how

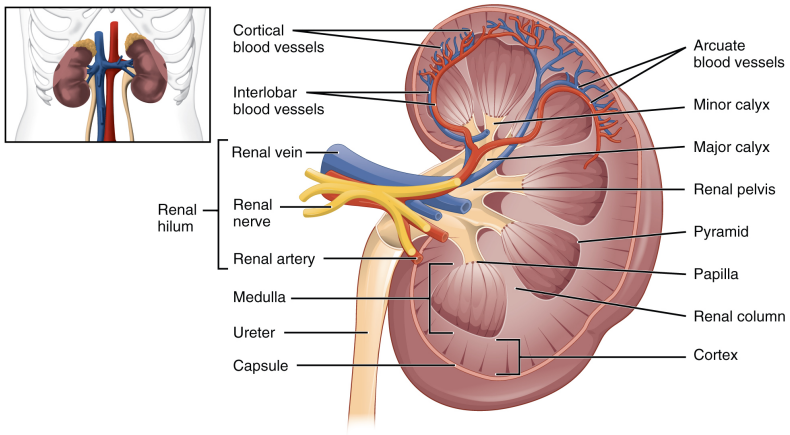

Figure 1.1: A diagram of the kidney anatomy (right) and their placement within the abdomen (left). Image credit: philschatz.com Anatomy and Physiology [122].

well the kidney is functioning, and thus a measure of the overall kidney health. For example, the normal estimate is around 100 mL/min/1.73m^2 and a sustained measurement of 60-90 mL/min/1.73m^2 is indicative of kidney damage.

1.2.2 Kidney Cancer and Partial Nephrectomy

Renal cell carcinoma is a one type of aggressive kidney cancer that is often treated through the removal of all or part of the kidney. It is the sixth most diagnosed malignancy in Canada in men and the tenth most common in women, with estimated 4,800 new cases and about 1,650 deaths from the disease in 2010. In the United States, 61,560 new cases of kidney cancer were diagnosed in 2015 [1]. Since the mid-1980s, death rates have decreased by 0.3 per cent per year for males, and for females by 0.7% per year. Despite the death rates decreasing, this type of cancer is also increasing its rate of incidence by approximately 1.3% per year. (Canadian Cancer Statistics: www.cancer.ca).

When the tumour in the kidney is small, less than 4 cm, or mostly on the outside of the kidney, the kidney tissue can be spared by only removing the cancerous tissue, rather than the entire kidney. The remaining kidney tissue continues to function as each section of the kidney is independent, as long as the blood flow is

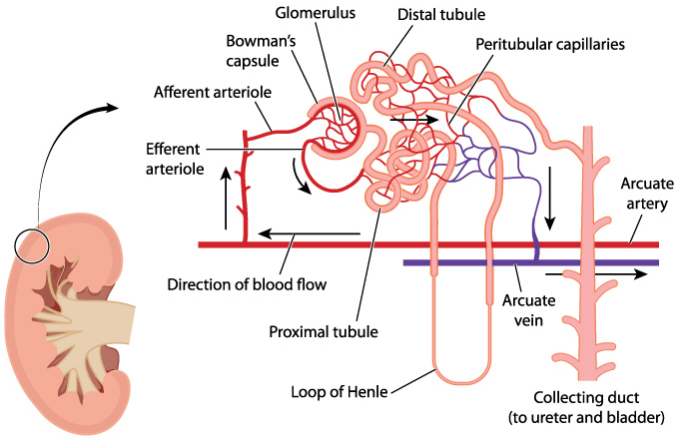

Figure 1.2: The detailed diagram of the nephron structure including the Glomerulus, Bowman's capsule and filtrate flow. Image Credit: Medical Science Navigator [135].

uninterrupted.

Partial nephrectomy, or removal of only a section of the kidney, is a relatively new procedure. In a study of matched patients receiving partial or radical nephrectomy, the patients receiving partial nephrectomy had equivalent long-term cancer outcomes, but a lower risk of long-term decreases in kidney function [96]. It is increasingly being performed but the complexity of the surgery has limited its widespread acceptance [130].

A detailed description of the surgical procedure is given in [157], but the following list outlines the steps in the robot-assisted procedure as experienced at our institution, the Vancouver General Hospital:

1. Prepare the patient and robot for surgery
2. Dock robot to the patient
3. Locate and dissect the gonadal vein and the ureter, follow this back to the renal hilum, identifying their entire path
4. Expose the renal hilum, where the vessels enter and exit the kidney
5. Determine location and expose the tumour, dissect additional fat if needed

6. Use laparoscopic ultrasound transducer to find the exact location of the tumour
7. Use ultrasound to determine tumour margins and mark them on the kidney surface using electrocautery
8. Place the clips on the renal hilum (25 minute warm ischemia time limit starts now)
9. Begin resection of tumour
10. Remove tumour, checking visually for clean margins
11. Suture the defect closed
12. Release the clamps on the hilum (25 minute warm ischemia time limit ends)
13. Check to make sure that there is no bleeding
14. Undock robot and finish closing using laparoscopic tools

The two major steps are 5) the localization of the kidney and tumor and 9-11) the removal of the tumor and defect reconstruction (repairing the hole left by removing the tumor). The localization and exposure of the renal hilum and the localization of the ureter is the most time consuming portion of the surgery. The total average time over 12 patients for the procedure was reported as 289.5 minutes (range 145-369 minutes) [36]. Since the exact locations of the vessels, including the renal artery and vein, are not known and the consequences of damaging these vessels would cause significant blood loss for the patient, surgeons proceed slowly and carefully. During the surgery, there is a time limit due to the necessity of clamping the major vessels to the kidney while the tumor removal is taking place [37]. After 25 minutes of warm ischemia time, it has been found that permanent damage to the kidney occurs [169]. The majority of the difficult suturing and defect reconstruction must be completed during the warm ischemia time, the time in which the blood flow to the kidney is cut off. The time for resection of the tumor and suturing was only 35.3 minutes (range 15-49 minutes) [36]. This means only about 12% of the total surgical time is spent during tumor resection and suturing,

while the rest of the time is spent locating the tumor and vessels, an area where improved ultrasound guidance could decrease the total time required for the procedure. There have been concerns that the use of partial nephrectomy could cause an increase in the rate of positive margins and cancer reoccurrence [134].

In general, surgeons try to leave 0.5 to 1 cm margins around the edge of the tumour to ensure that all cancerous tissue has been removed [161]. It has been found that any positive margin leads to the same (low) risk of cancer reoccurrence, but any positive margin, indicating some cancerous tissue had been left behind, increases the reoccurrence rate [134]. Intra-operative laparoscopic ultrasound is used to determine the extent and location of the tumor during surgery and helps determine the margins of the resection, providing the surgeon with another tool to minimize the occurrence of positive margins.

As the localization of the vessels is an important and potentially time consuming step within the procedure, one of the methods to provide additional guidance would be to register the ultrasound images of the vessels to pre-operative Computed Tomography (CT) scans of the patient [143]. Vessels have been previously used to register intra-operative data to pre-operative CT and Magnetic Resonance Imaging (MRI) scans [39, 127, 136]. For example, the cortical vessels of the brain were used to orient the surgeon and account for brain deformation during image guided surgery through video tracking of the vessels [39] or tracked ultrasound [136]. Image guidance during liver surgery is another application in which vessels were used for registration [93, 98]. The vessels of the liver are prominent features in surgical navigation for tumour resection. In addition, in complicated structures such as the liver, hierarchical methods of vessel registration were also implemented [124]. Previous work on vessel extraction and registration have involved voxel-based registration [98], image-to-model registration [74], model-to-model registration [136] and the integration of landmark and intensity information [93]. Model-to-model registration methods typically use a modified version of the Iterative Closest Point (ICP) algorithm [22] applied to the vessel centerlines. Other methods use Doppler images to create a model from the ultrasound images with region growing segmentation [92] or color-based segmentation [136].

Registering the pre-operative CT would allow the surgeon to see the relationships between the vessel and kidney structure. In section 2, the possibility of regis-

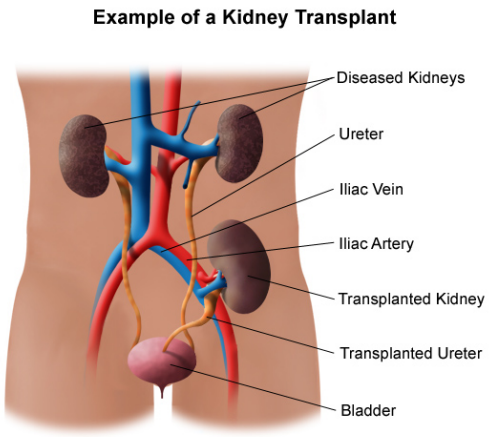

Figure 1.3: The transplant kidney is placed in the pelvis rather than in place of the failing kidney. It is attached to the iliac artery and vein. Image Credit: University of Utah Healthcare [119].

tering 3D ultrasound reconstructions of vessel structures with their corresponding CT structures is explored further.

1.2.3 Kidney Transplant and Transplant Fibrosis

Kidneys are one of the most commonly transplanted organs with 1265 transplants from live and deceased donors taking place across Canada in 2014 (Canadian Institute for Health Information). In this case, the donor organ is removed from the donor and placed into the pelvic region of the recipient. It is not placed where the native kidney resides since in many cases the native kidneys are not removed. Due to the placement of the transplant kidneys, they are very close to the surface of the patient's skin. This makes them very accessible for ultrasound and elastography interrogation.

The kidneys are a redundant organ, meaning that a single kidney is sufficient to filter the entire blood flow. This means that a person can function well with only a single kidney, making living kidney donors an option and that a transplant recipient only needs a single kidney to live a full and healthy life.

Renal transplantation represents the current gold standard in the treatment of patients with End Stage Renal Disease (ESRD). The major causes of ESRD are dia-

betes and hypertension, but other causes include glomerulonephritis, infection and polycystic kidney disease [73]. ESRD is characterized by low EGFR and eventual kidney failure. When diagnosed with ESRD, the patient must be put on dialysis or must receive an organ transplant. Great strides have been made in the management of renal transplant recipients in terms of supportive care, immunology, and drug therapeutics. While treatment of acute problems such as rejection has significantly improved over the past two decades, overall long term kidney graft survival is still a major problem. Indeed, the half-life for the graft was 36 and 19.5 years respectively (when removing those patients who died with a functioning graft) [57]. In 2013, the 5 year survival rates for kidney transplant patients who received their kidney from deceased donors is about 85% respectively [107]. It has been shown that clinical acute rejection within the first year decreases the long term survival and that chronic rejection is an important factor in graft failure [57].

CAN or as it is sometimes known, Chronic Allograft Dysfunction (CAD), is the term that describes the build up of interstitial fibrosis and tubular atrophy, which is characterized by thickening of the basement membranes and flattening of the epithelial cells [150]. In a study of risk factors for CAN, Schwarz *et al.* found that the patients at the highest risk for CAN were those with early histological changes (found on serial biopsy), a deceased donor and long cold ischemia times (the time during which the kidney was outside of a body during the transplant process) [150].

CAN is one of the common causes for eventual kidney transplant failure [57]. The fibrosis may be caused by the accumulation of rejection episodes that might not have obvious outward symptoms, known as subclinical rejection. Over time, the episodes cause fibrosis and scar tissue to build up and prevent the nephrons from functioning properly and the transplant organ fails. If the level of fibrosis could be measured and identified in the early stages of rejection episodes, these could be mitigated by making changes in the patient's immunosuppressant regimen.

Currently, the only method for measuring the level of fibrosis is through the use of biopsy. Biopsy of the kidney removes a small section of the kidney using an ultrasound guided biopsy needle. This tissue section is then sent to pathology where the level of fibrosis is identified. This process is painful for the patient and may lead to complications and morbidity [149]. Schwarz *et al.* reported on the safety of graft biopsy [149]. In a study of 1171 biopsies of 508 patients, they found

that arterio-venous fistulas occurred in 7.3% of the biopsies and gross hematuria occurred in 3.5% of the biopsies. 1% of the biopsies resulted in major complications. Although the complication rate is low, there are still risks, and patients who are on blood thinning medications must stop these medications before the biopsy is completed, which introduces other risks.

Some institutions have completed studies using serial biopsies in order to better understand the formation of fibrosis, and how subclinical rejection episodes influence the long-term graft survival. It is possible that these serial biopsies could detect the subclinical rejection episodes, and changes in medication and treatment could have resulted in better long term outcomes [110]. In one study, subclinical rejection was found in 14% of the patients [150]. CAN was found in 5% of the first round of these biopsies at 6 weeks and 37% of patients at 26 weeks. Another study found that CAN was present in one third of the patients at 1 year [116]. This shows that the early development of CAN, which could affect long term graft survival, is often progressing undetected.

To standardize the assessment of the tissue from biopsy, a scoring system was developed [155]. This scoring system measures different aspects of the tissue, including tubular atrophy, interstitial fibrosis, arteriolar hyaline thickening, glomerulopathy and vascular fibrous intimal thickening.

In particular, for this thesis, the interstitial fibrosis measurement is of most interest as it is most likely to cause distinguishable effects on the measured kidney stiffness, as well as functional effects on the kidney. According to the Banff scoring system, the amount of interstitial fibrosis is broken down into four levels regarding the amount of cortical area affected by the fibrosis.

- Level 0: less than 5% of the tissue shows evidence of fibrosis
- Level 1: between 6% and 25% of the tissues shows fibrosis
- Level 2: between 26% and 50% of the tissue shows evidence of fibrosis
- Level 3: More than 50% of the tissue shows evidence of fibrosis.

Using a non-invasive method for measuring fibrosis, such as ultrasound, would allow for constant and ongoing monitoring of the kidney health. A non-invasive

method would mean that the early detection of CAN is potentially more likely and could result in changes in patient treatment. This will hopefully lead to kidney grafts that will last longer and improve the long-term outcomes for transplant patients.

1.3 Ultrasound Imaging

Ultrasound imaging is a non-invasive, non-ionizing and real-time method of medical imaging. Ultrasound offers real-time imaging with typical frame rates of 40 Hz, it is non-ionizing which makes it safer to use for both the patient and the operator and it is inexpensive compared to other imaging modalities. All of these characteristics make ultrasound an advantageous imaging modality for intraoperative navigation and guidance. A full explanation of ultrasound imaging can be found in textbooks [23], but a short overview will be presented here.

Ultrasound sound uses high frequency pulses to create images of tissue underneath the surface of a patient's skin or organ surface.

The system consists of a transducer, which is placed on the patient, and a processing machine or ultrasound scanner, which sends the energy to the transducer and receives the signals from the transducer. The ultrasound scanner then creates the images for the doctor or technician. The transducer is made of an array of piezoelectric crystals. These crystals vibrate in response to an electric stimulus and also produce an electric signal is response to a vibration stimulus.

With an electrical stimulus, the piezoelectric crystals of the transducer send a pulsed vibration at approximately 3-10 MHz into the body. These pulses travel through the tissue at approximately 1540 m/s. 1540m/s is the average speed for these waves in soft tissue. The true speed ranges from 1450 m/s in fat to 1580 m/s in muscle. The reflections from these waves are sensed by the piezolelectric crystals over time. The depth of a particular reflection can be calculated from the time of flight between when the pulse was created and when the echo was detected by the crystal and the associated electronics. The speed of sound generally changes very little depending on the tissue type [62], so this average is used for all tissue types unless specified otherwise.

The depth, d, is calculated as:

$$d = (t * c)/2 \ , \tag{1.1}$$

where t is the time from the pulse generation to the reception of the reflection or echo, and c is the speed of sound within the tissue.

The reflections are created when there is a change in the acoustic impedance Z of the tissue. The acoustic impedance is calculated as $Z = \rho c$ where ρ is the tissue density and c is the speed of sound in tissue.

The ratio of the energy passing through a boundary and the reflected energy is known as the reflection coefficient. This coefficient of any perpendicular reflection from a boundary between materials of two different impedances Z_1 and Z_2 is as follows

$$R = (Z_2 - Z_1)/(Z_2 + Z_1). \tag{1.2}$$

In general the reflection coefficient between soft tissues is small, such that most of the energy of the wave is transmitted through the tissue.

After the reflections are recorded, envelope detection is performed via a Hilbert Transform and the resulting signal is compressed to an appropriate range for display. After compression, the data is mapped to the transducer coordinate frame to display a geometrically accurate image of echo reflection strength as a function of echo location. This image is called a B-mode image (B for "Brightness").

In the cases of bone or air, there can be large reflection coefficients, where most of the wave is reflected at the boundary. This creates a shadowing effect, where the image past this boundary is mostly dark.

A general characteristic of ultrasound images is determined by sub-wavelength inhomogeneities in the tissue that create small echoes known as speckle. This speckle pattern depends on the transducer used and the type of image processing employed to generate the B-mode image.

Ultrasound transducers come in a variety of shapes, sizes and frequencies depending on their intended use. Transducers designed for examining small regions close to the surface use higher frequency pulses, often close or in excess of 10 MHz. The higher frequency waves allow for higher resolution imaging because they generate narrower pulses that can distinguish between reflectors that are close

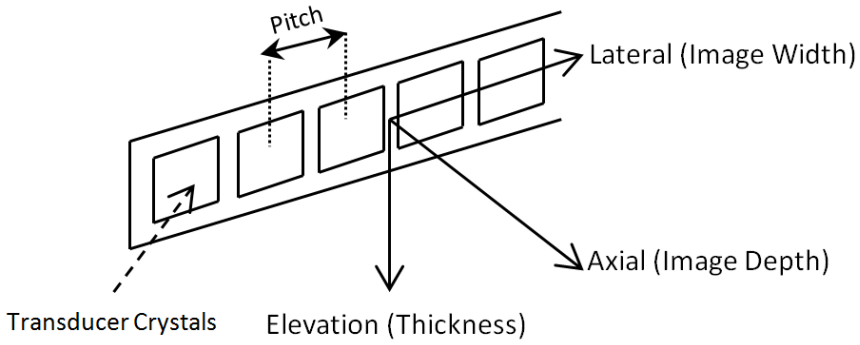

Figure 1.4: The pitch is the spacing between the piezoelectric crystals. The three directions of the image are defined as axial (away from the probe), lateral (along the direction of the crystal array) and elevational (out of plane).

to each other. However, the attenuation of ultrasound pulses in tissue increases with frequency, so the total depth of imaging is lower. Transducers that are meant for imaging the abdomen transmit longer pulses at a lower frequency, generally between 3-5 MHz. These transducers are able to image at a much greater depth than those at higher frequency. The depth for typical ultrasound images ranges from 2-16 cm depending in the transmitting frequency.

The piezoelectric crystals of many transducers are arranged in a linear fashion at the face of the transducer. Other possible arrangements include a curvilinear arrangement along a convex surface (convex arrays) to provide a wider field of view, and a matrix arrangement, which would allow for fast 3D imaging. The spacing between the crystal elements is known as the pitch. The direction of the row of piezoelectric crystals is known as the lateral direction, the direction of wave transmission (away from the transducer face in the body) is known as the axial direction and the final direction, out of plane of the produced image, is known as the elevational direction (Figure 1.4).

Ultrasound images have the greatest resolution in the axial direction, which is determined by the pulse length. The resolution in the lateral direction is deter-

mined by the beam width. This can be improved using beam focusing [164]. The resolution in the elevation direction is also determined by beam width via a fixed lens on the transducer face, and cannot be changed using software.

For all work in this thesis, an Ultrasonix Touch ultrasound machine (Analogic, Richmond, BC) was used. This machine is equipped with an Software Development Kit (SDK), which allows access to programming the underlying signal transmissions and processing. An image is typically formed by the sequential transmit and receive of groups of crystals along the lateral direction of the image. The time required to complete the sending and receiving of the signals will determine the frame rate of the imaging system. By adjusting the sequence of sending and receiving, possible with the Ultrasonix SDK, it is possible to create a small section of an image at a very high frame rate. This concept will be described in more detail in Section 1.4.

1.4 Ultrasound Elastography

In a broad sense, elastography is the measurement of tissue stiffness. A comprehensive overview of elastography can be found in the thesis by Jeffrey Abeysekera [3] and a short review is presented here.

Although there are several methods for measurement, all methods use the same underlying principle. The tissue is physically pushed and then ultrasound imaging is used to measure the tissue response to this push. For a dynamic push, the shear wave that is created moves through the tissue at a speed and wave length that is determined in large part by the shear modulus or elasticity of the tissue.

The original method for measurement of tissue stiffness is using quasi-static strain measurements. This requires a user to slightly compress and decompress the tissue. The tissue is compared in the two states and the relative motion is calculated. This method allows the *relative displacement* or strain of the tissues within the image to be compared, but does not allow for comparison between imaging sessions or between patients, because strain depends on the push and on the boundary condition surrounding the region of interest, so it is not an intrinsic property of tissue. However, strain measurement opened the gateway for subsequent development of *absolute* or *quantitative* measurement methods by providing proof that the

tissue stiffness could be correlated with tissue health.

Absolute elasticity methods allow for the tissue stiffness to be measured in a quantitative manner by observing the dynamic wave propagation, producing a quantitative measurement of shear modulus or Young's modulus in kilopascals (kPa). This allows for intra- and inter-patient comparisons. The excitation can be generated by an acoustic force [21, 40, 118] or by external vibration [12, 34]. We use an external vibration source and a standard ultrasound machine. This system was named Shear Wave Absolute Vibro-Elastography (SWAVE) and will be referred to as such for the remainder of this thesis.

For a harmonic excitation, shear wave propagation in an isotropic homogeneous elastic solid, and for incompressible tissues undergoing small strain and linear approximations, is described in the frequency domain by the following wave equation:

$$\rho(j\omega)^2\hat{u}(x,j\omega) = \mu\nabla^2\hat{u}(x,j\omega)\ , \tag{1.3}$$

where ρ is the tissue density, ω is the frequency, $\hat{u}(x,j\omega)$ are the displacement phasors and μ is the shear modulus.

We assume that the density of tissue ρ is homogeneous and equal to that of water. This is a common assumption in the elastography community even though tissue density does change with tissue type and affects the wave speed. We also assume that the displacement phasors $\hat{u}(x,j\omega)$ generated in the tissue by the exciter have only a shear wave component, no pressure wave component. Then, if one component of the displacement phasors $\hat{u}(x,j\omega)$ is known over a region of interest, in this case the axial displacement with respect to the transducer, the Helmholtz equation (1.3) can be used to find the shear modulus μ.

There are various ways to define the elastic modulus, or elasticity. In much of the literature, the Young's Modulus (E) is used and describes a material's resistance to deformation under unilateral compression. The shear modulus (μ) specifically describes a material's resistance to shear. Poisson's ratio (ν) defines the ratio of deformation that occurs orthogonal to the applied force due to tissue compressibility. It is generally assumed that the Poisson's ratio for tissue is ≈ 0.5, or that tissue is incompressible. The shear modulus, Young's modulus and Poisson's ratio

are related in the equation below, for a homogeneous, isotropic, linear elastic and incompressible material:

$$\mu = \frac{E}{2(1+\nu)} \tag{1.4}$$

When ν is = 0.5, this reduces to $E \approx 3\mu$.

With the above assumptions, the speed of the shear wave c_s, the shear wave wavelength, λ, at a known frequency, f, can be related to Young's Modulus, E, as follows:

$$E = 3\mu \tag{1.5}$$

$$\mu = \rho c_s^2 \tag{1.6}$$

$$c_s = f\lambda \tag{1.7}$$

$$E = 3\rho(f\lambda)^2 \ . \tag{1.8}$$

1.5 SWAVE

In the SWAVE imaging method used in this thesis, the displacement phasors from each 2D image are interpolated over a regular 3D grid and the distribution of shear moduli over the tissue is estimated by using a local spatial frequency estimator, such as Local Frequency Estimation (LFE) [105]. As the vibration source is not in any particular position with relation to the ultrasound probe, it is important to measure the wave in three dimensions to measure the full length of wave, which may not be within the imaging plane. The local frequency of the 3D volume is estimated after applying a bank of directional filters. These filters are directionally oriented and cover a wide band of spatial frequencies. The weighted average of the ratios between the outputs from these filters determines the local frequency at that location within the volume. This 3D volume can be created in a variety of ways including a motorized 3D probe, a tracked freehand 2D probe or a motorized 2D

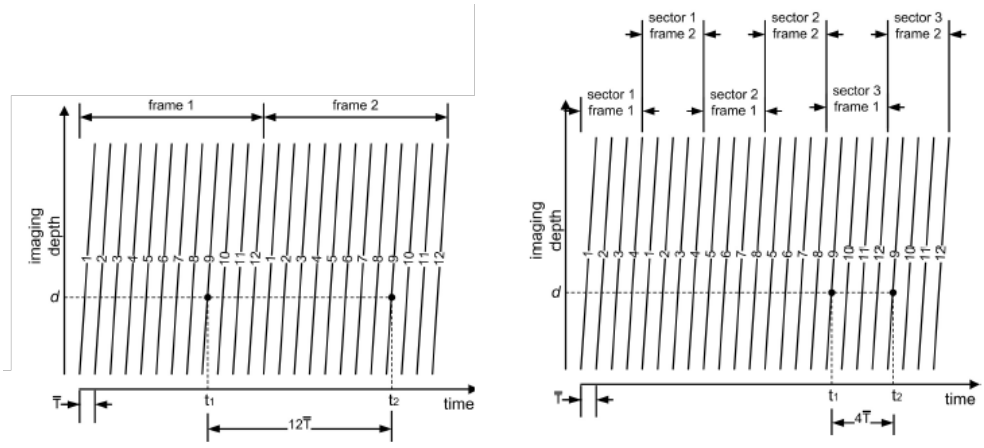

Figure 1.5: Left: Acquisition timeline for two frames of B-mode data for a twelve scan-line field of view. Right: Acquisition timeline for two frames of high-frame-rate acquisition data for a four scan-line field of view. T is the time required for acquisition of a single RF line.

probe.

Strain is inversely proportional to elasticity under certain conditions, such as uniform stress. Changing boundaries violates this assumption, which results in image artifacts that do not represent the elasticity of tissue, but are the result of a non-uniform stress field within the tissue. SWAVE however, measures the local wavelength of the waves traveling in the tissue, which is dependent on the local intrinsic elasticity of the tissue.

With a steady state excitation, the axial displacement phasors can be estimated over a volume at a high effective frame rate using sector based imaging. In other words, using the software development kit provided by Ultrasonix, it is possible to program the sequence of imaging on the ultrasound machine. By repeatedly imaging a small section of the image, the frame rate can be much higher than when imaging the entire width of the image (Figure 1.5) [12].

Our system uses an external mechanical exciter, a voice coil shaker, driven by waveforms created by a signal generator (Agilent 33220A) controlled through software loaded on the Ultrasonix machine. The excitation is applied directly to the phantom or tissue. No particular positioning of the exciter with respect to the

transducer in needed. When the tissue motion is analyzed in the frequency domain, the motion caused by each of the frequencies of excitation can be separated.

1.5.1 Overview of Elastography Methods

There are several methods to measure tissue elasticity. In this Section, an overview of the other systems are presented with their advantages and limitations.

Two of the other methods of quantitative elastography are acoustic radiation force impulse imaging [118] and supersonic shear wave imaging [21]. Both of these methods use the acoustic power from the ultrasound transducer to create displacements in the tissue. The impulses are focused along the axial direction of the ultrasound image to create a wave in the tissue that propagates in the lateral direction of the image. Using high speed imaging techniques the wave is tracked as it moves away from the focus line of the push, or uses the ultrasound to measure the tissue response at the site of the push.

One limitation of this technique is that it requires a higher power machine in order to create the acoustic push. It is available on the Siemens Acuson Machine (Erlangen, Germany), the Philips EPIQ (Philips Healthcare, Boston, Mass), and the Supersonic Imagine Aixplorer (Aix-en-Provence, France). One advantage of this technique is that no external hardware is required and the push is created within the ultrasound transducer. It is also very localized, and has a high potential resolution. This method has been used extensively for breast cancer measurements [40, 44, 117]. The depth of measurement using this technique is limited as the power needed to create the push cannot penetrate further than about 6 cm. This limits its use in deeper organs, such as liver.

Another commercially available method of stiffness measurement is the FibroScan system (Echosens, Paris, France). FibroScan is an elasticity measurement system that uses a mechanical impulse and a single ultrasound element. The system measures the response of the tissue to the mechanical impulse along the line of the ultrasound element. One limitation of this system is that there is no B-mode ultrasound guidance for the measurement to guide the user. FibroScan is suited for large homogeneous organs such as the liver. The system is easy to use and it has been proven to accurately measure the liver stiffness and level of liver cirrhosis

[72].

External vibration is used in Magnetic Resonance Elastography (MRE) and in the steady state shear wave ultrasound elastography used in this thesis. In this method, a constant vibration source is used to create steady state waves at a known frequency of excitation [106]. The displacements of the tissue are measured as the tissue moves and the local wavelength within the tissue can be measured with image processing techniques [187].

One advantage of using MRE is that the imaging technique is already in 3D and the waves can be measured naturally in three dimensions. The disadvantage is that imaging can be very slow, one acquisition taking several minutes. The approach used in this thesis is similar in principle to that used in MRE. The advantages of our approach are that we eliminate the challenges of penetration depth and tissue heating that are associated with using acoustic impulse forces for excitation. In addition, we can excite the tissue at specific frequencies, allowing us to examine the frequency dependency of tissue stiffness [154]. Using multiple frequencies also decreases the problems caused by nodes in the wave patterns [167]. Nodes can cause artifacts in the elasticity image because there is no displacement at these points, and therefore the wavelength measurement is unreliable. One disadvantage of this method is the desirability of having multiple wavelengths within the tissue of interest in order to get an accurate measure the wavelength; this is because ultrasound can only accurately measure axial displacement of the tissue.

1.6 Minimally Invasive Surgery, Intra-operative Ultrasound and the da Vinci Robot

1.6.1 Minimally Invasive Surgery

Minimally invasive surgery is slowly becoming the standard of care for many procedures, and continues to grow in popularity. Minimally invasive operations often require several small incisions, of approximately 2 cm each, to be made through the patient's skin, instead of the 10-15 cm incision required for a traditional open surgery. The surgeon works using long specialized instruments and views the surgical scene through a laparoscopic camera. This type of procedure decreases the pa-

tient's morbidity and shortens hospital stays [47, 137]. Many abdominal, thoracic and pelvic procedures are now completed as minimally invasive (or laparoscopic) operations.

Although there are benefits to the patient, additional physical and cognitive loads are placed on the surgeon [99, 173]. First of all, the surgeon must work with instruments that lack the degrees of freedom available in the human hand. The majority of laparoscopic instruments do not have any wrist-like joints at the end-effector. Additionally, during laparoscopic surgery, the surgeon must overcome working through the 'fulcrum effect' caused by the instrument having to pass through a narrow opening in the mostly rigid abdominal wall. This constraint makes the tip of the instrument move in the opposite direction of the surgeon's hand. Also, the view of the surgical field becomes considerably more restricted when moving from open surgery to laparoscopic surgery. The surgeon is no longer able to see the entire surgical field at once, but must rely on the narrow view through the laparoscopic camera. Last, they are now looking at a single camera image, they lose binocular vision, and therefore, depth perception.

The limitations of laparoscopic surgery are especially noticeable in more difficult surgeries, such as laparoscopic partial nephrectomy [130]. Partial nephrectomy is one treatment for kidney cancer. Kidney cancer refers to any tumours that occur in the parenchyma of the kidney, of which approximately 80% are renal cell carcinomas.

Because partial nephrectomy allows the cancerous tissue to be removed while preserving as much of the healthy kidney tissues as possible, it is the preferred method over radical nephrectomy for tumours under 4 centimetres in size [77]. Laparoscopic partial nephrectomy has also gained popularity as it is minimally invasive and has shown to have comparable outcomes to open procedures [56, 130, 141]. Partial nephrectomy, with its innate challenges, as described above in Section 1.2.2, combined with the limitations of laparoscopic surgery, make partial nephrectomy an operation which could be improved through the application of new technologies, such as intra-operative ultrasound.

The use of intra-operative ultrasound could also be pivotal to the improvement of surgery. As a real-time imaging technique, ultrasound has the potential to be used for registration to pre-operative data and also as a method of direct vi-

sualization of critical structures such as with elastography. Through the use of intra-operative ultrasound combined with robotic technology, the challenges of laparoscopic surgery and partial nephrectomy have the potential to be minimized [143].

1.6.2 Intra-operative Ultrasound

Intra-operative ultrasound was first introduced in the 1950s [104]. In 1958, the first laparoscopic ultrasound transducer was used during cholecystectomy, but intra-operative ultrasound did not gain widespread usage until B-mode images became available in the 1970s and interpretation of images became more straightforward since 2D B-mode images could now be visualized as a 'picture' rather than a single echo line. Laparoscopic ultrasound also gained popularity with the spread of minimally invasive surgery, where the ultrasound images enhance guidance when using laparoscopic tools [104]. Traditional laparoscopic intra-operative ultrasound is currently used for a variety of procedures, including resection of liver cancer [16], gall bladder removal [31] and resection of kidney cancer [129]. Intra-operative ultrasound provides high-quality, real-time intra-operative imaging for assessment of tumour margins, guidance around vessels and locating tumour resection planes. Våpenstad *et al.* presents a survey on the current use of laparoscopic ultrasound [174].

1.6.3 Robot-assisted Surgery with the da Vinci Surgical System

The introduction of robotic systems such as the da Vinci Surgical System attempts to mitigate the shortcoming of laparoscopic surgery by replicating an environment more similar to that of traditional open surgery. The system consists of three sections: the surgeon's console, the patient side cart and the vision cart [Figure 1.6]. The surgeon is able to sit comfortably and ergonomically at the console (a possible improvement over traditional open surgery), and the patient is positioned on the table by the patient side cart. The surgeon sits at the surgeon's console and his/her motions are mapped to the motions of the instruments on the patient-side cart, this is known as a teleoperated robot, or a master (the surgeon) and slave (the instruments of the patient side cart) configuration. Although the da Vinci system does not

Figure 1.6: The da Vinci Surgical System. Image courtesy of Intuitive Surgical Inc.

currently included automation, the surgeon's motions are scaled and filtered to improve dexterity and to remove tremor. The instruments used during robotic surgery are wristed at the end-effector, allowing the surgeon to regain natural control of the degrees of freedom of the tools.

The orientation of the surgeon's hands on the 'master manipulators' is constrained to match the orientation of the end-effector as seen by the surgeon through the cameras. The surgeon uses the 'master manipulators' in the surgeon's console to control all of the Degree of Freedom (DOF) available to the instrument, generally six or seven. In six DOF instruments, there are three translational degrees and three rotational degrees of freedom while in seven DOF instruments, the surgeon also controls the grasping motion of the instrument. The camera arrangement is also different from laparoscopic procedures. The da Vinci laparoscope has two camera channels that run along its length. The video feeds are kept separate until viewed by the surgeon through the console. This camera system is stereoscopic, simulating binocular vision and allows for depth information to be provided to the surgeon. This, along with the degrees of freedom of the instruments, makes manipulations of tissue, knot tying, needle passing, and discrimination of layers more effective [30, 68, 184].

Although the da Vinci robot offers advantages over traditional laparoscopic

surgery, some studies have found that experienced laparoscopic surgeons have not seen a significant benefit [101]. On the other hand, the da Vinci robot is a good platform for integration of additional aids and is not being currently used to its full potential. With additional navigational aids, such as intra-operative imaging, we believe the surgical guidance can be improved. The stereoscopic vision allows the surgeons to visualize intra-operative and pre-operative imaging [175], and can be used for tissue tracking in 3D [159]. Using the joint angles of the robot encoders, the tool position and orientation can be tracked within the accuracy of other commonly used surgical localizers, approximately 1 mm [89].

One of the main limitations cited by researchers and users is the lack of haptic feedback to the surgeon in the console during the surgery. This means that the surgeon can no longer feel the tissue in the traditional way using the sensors in their fingers. The surgeons often feel for tumours under the tissue surface. Tumours are often much stiffer than the surrounding tissue, which means the surgeon can palpate or touch the tissue to determine its approximate depth and diameter even when it is not visible on the surface of the tissue [86, 88, 109]. This would then guide the surgeon's further dissection or resection. This limitation could be mitigated through the use of ultrasound elastography as a tool for identifying stiff areas below the surface.

There are two interfaces used to get information to and from the da Vinci Robot. The clinical robot Application Programming Interface (API) is used to read the joint angles from the robot in real time. These joint angles can be used to locate the tools in space through the use of forward kinematics. This interface can be used while the robot is in clinical use.

The other interface used is the da Vinci Research Kit (DVRK). The DVRK differs from the previously mentioned API, in that it does not use the clinical da Vinci software, but uses a separate controller to command the joint positions, velocities or torques of each of the robot arms [33, 79]. These controllers are linked to a computer and each arm is controlled individually. This allows for a computer to automate the motion of the robot, in addition to the usual teleoperation mode of the da Vinci.

1.6.4 Intra-operative Ultrasound for the da Vinci

Although traditional laparoscopic ultrasound instrumentation is a valuable imaging tool in many types of surgery, the manoeuvrability, and thus imaging ability, with these types of instruments is limited. Furthermore, during robotic procedures, laparoscopic ultrasound probes are typically controlled by the patient bedside surgical assistant instead of the operating surgeon. Additionally, the ultrasound instrument requires a dedicated laparoscopic port, meaning that another instrument must be removed from the surgical field and the operation must be halted while scanning is taking place. It is well established that ultrasound is highly user dependent modality in two main ways. Firstly, the quality of the ultrasound image views depends on the experience of the user. Secondly, only some users have the ability to make three-dimensional connections between the images and the actual anatomy. Manipulating the transducer allows the surgeon's natural hand-eye coordination to aid in the interpretation of the 3D anatomy from a series of 2D cross-sectional images.

In order to provide the operating surgeon with control of the transducer, and to integrate intra-operative ultrasound into robotic surgery, an ultrasound transducer that is controlled directly from the da Vinci surgeon's console was proposed [100]. Later, another transducer was designed and modeled after a typical da Vinci 5mm tool and had greater mobility inside the patient [142]. However, both of these combined ultrasound/da Vinci tools still require a dedicated port or da Vinci tool changes, and this version of the 5mm da Vinci tool is more limited in its range orientation than a typical 8mm da Vinci tool.

The first miniature "pick up" style probe was developed for cardiac procedures. A 13 MHz Aloka (Hitachi Aloka Medical, Wallingford, CT) mini-transducer ($15 \times 9 \times 6$mm) has been used for characterization of the coronary arteries during thoracic laparoscopic surgery [28, 29]. This transducer was outfitted with a small fin that allowed the da Vinci needle drivers to grasp and maneuver the transducer.

Two commercial products have recently been introduced, one by Aloka (Wallingford, CT), and one by Analogic Ultrasound (named the ProArt$^{\textregistered}$) (Peabody, MA). Both these ultrasound transducers are designed with a fin on the ventral proximal surface that fits the da Vinci Pro-Grasp$^{\text{TM}}$ tool (model 420093). The fin is placed in

such a way that the long axis of the transducer and the jaws of the tool are parallel. They fit through a standard sized trocar and use the TilePro display in the da Vinci S and Si. Both transducers are high frequency and thus have high resolution with relatively low penetration depth. The Aloka model is a linear array transducer and the ProArt® uses a curved array for wider visibility.

The grasping fin designs of the three transducers mentioned above do not enable a repeatable, stable grasp by a da Vinci tool, such as the Pro-Grasp™ forceps. The Pro-Grasp™ forceps are a very commonly used dissection tool and their slotted shape is conducive to holding onto an ultrasound transducer. While the fin design of [28, 29] makes it easy to grasp the device, the location of the grasp is not well defined. A stable, repeatable grasp is needed for accurate 3D tissue reconstruction or localization with respect to the da Vinci coordinate system.

In order to take advantage of the degrees of freedom available with the da Vinci wristed tools, a new intra-abdominal pick-up transducer was designed in previous research to fulfill the design parameters (Figure 1.10) [143]. As outlined in this paper, the design requirements for this new transducer were determined through consultations with the surgeons at our center and a transducer manufacturer. The completed transducer is small enough to fit through a standard laparoscopic incision and be maneuverable within the abdominal cavity. The da Vinci tools can grasp the transducer in a repeatable manner and create a fixed transformation between the tool location and the ultrasound image. The transducer's motion should also be fully constrained once grasped. Finally, the tool self-aligns with the 'locking' mechanism on the transducer, such that the tool and transducer need not be well aligned initially to guarantee capture.

The transducer:

- is small enough to be maneuvered inside the patient
- has a small enough diameter to fit through a surgical incision
- has a consistent and self-aligning interface with the da Vinci grasper
- has no sharp or breakable components
- can be tracked via multiple modalities

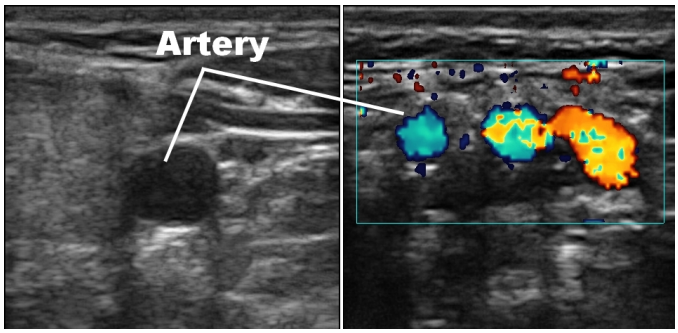

Figure 1.7: Example ultrasound images created with the intraoperative "pick-up" transducer of the carotid artery and vein. Left: B-mode image. Right: Doppler image of the arteries after bifurcation.

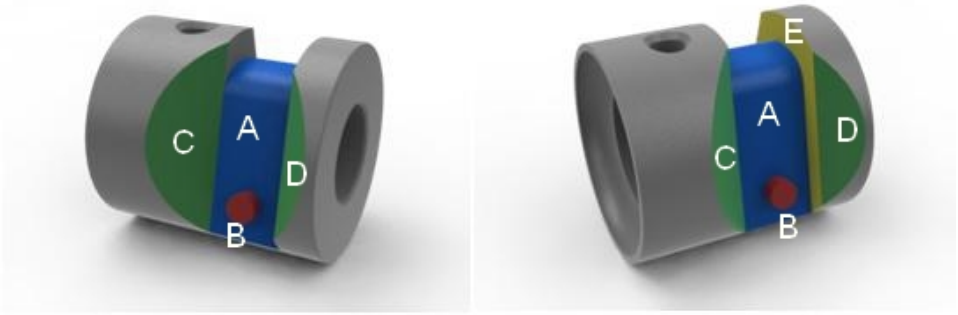

Figure 1.8: Rendered images of the da Vinci interface.

- can be sterilized using standard methods.

The transducer is made of 128 elements spaced over an imaging face of 28 mm and has a center frequency of 10 MHz. These are similar characteristics to other commercially available intraoperative transducers which provide high-resolution imaging to a depth of 4 to 6 cm. Pin connections are currently compatible with Ultrasonix ultrasound machines (Analogic Medical Corp., Richmond, Canada). Examples of the B-mode and Doppler images are displayed in Figure 1.7.

Unique to this transducer, and different from the commercially available transducers, is the specially designed interface between the transducer and the da Vinci Pro-Grasp^{TM} forceps. This metal interface was designed such that it forms a lock-

ing type grasp with the Pro-Grasp^{TM} tool [Figure 1.8]. A groove [Figure 1.8], shown in blue (A), was built to match the width of the Pro-Grasp^{TM}. A small pin, shown in red (B), was designed to catch in the end of the tool slot and prevent the tool from sliding off. The walls of the groove are angled, shown in green (C, D), to increase the capture range. One wall is slanted to the floor of the groove, while the other ends just short, shown in yellow (E). The solid wall helps to constrain the motion between the transducer and the tool while the fully slanted wall prevents the tool from ever becoming jammed into the groove. The angle between the two sides of the groove matches that of the Pro-Grasp^{TM} when the tool is completely closed on to the metal walls. This allows for a fixed transformation between the da Vinci tool and the transducer, which in turn transfers all the degrees of freedom and range of motion available to the da Vinci tool to the transducer. The jointed wrist of the da Vinci and direct connection to the transducer makes manipulation easier than traditional hand-held laparoscopic transducers [148] and because the two are now fixed, it is possible to track the ultrasound transducer by measuring the location of the tool (Section 2. The transducer was manufactured by Vermon (Vermon, Tours, France) and is approved for STERRAD (ASP, Irvine, CA) sterilization methods that are commonly used in hospitals to sterilize ultrasound transducers. STERRAD is a low temperature method of sterilization for sensitive surgical instruments using hydrogen peroxide gas plasma technology and manufactured by Advanced Sterilization Products.

Another unique aspect of this transducer is the inclusion of an electromagnetic sensor inside the body of the transducer [Figure 1.9]. A Model 180 (Ascension, Vermont, USA) 6 degree of freedom sensor is used and compatible with the software of the Ultrasonix Ultrasound GPS system.

As an alternative, a flat checkerboard for visual tracking can be placed on either flat section of the transducer, which is approximately 24mm $\times$ 10mm. An example of this checkerboard is shown in Figure 1.9, and can be used, as described later, for 3D tracking with a stereo camera. The checkerboard is surgical identification tape (Key Surgical Inc., MN, USA) that is approved for human use and designed to withstand repeated autoclave sterilization cycles [42].

The transducer can be placed into the abdominal cavity before the laparoscopic cannulas. The transducer tether will run alongside the camera cannula, but through

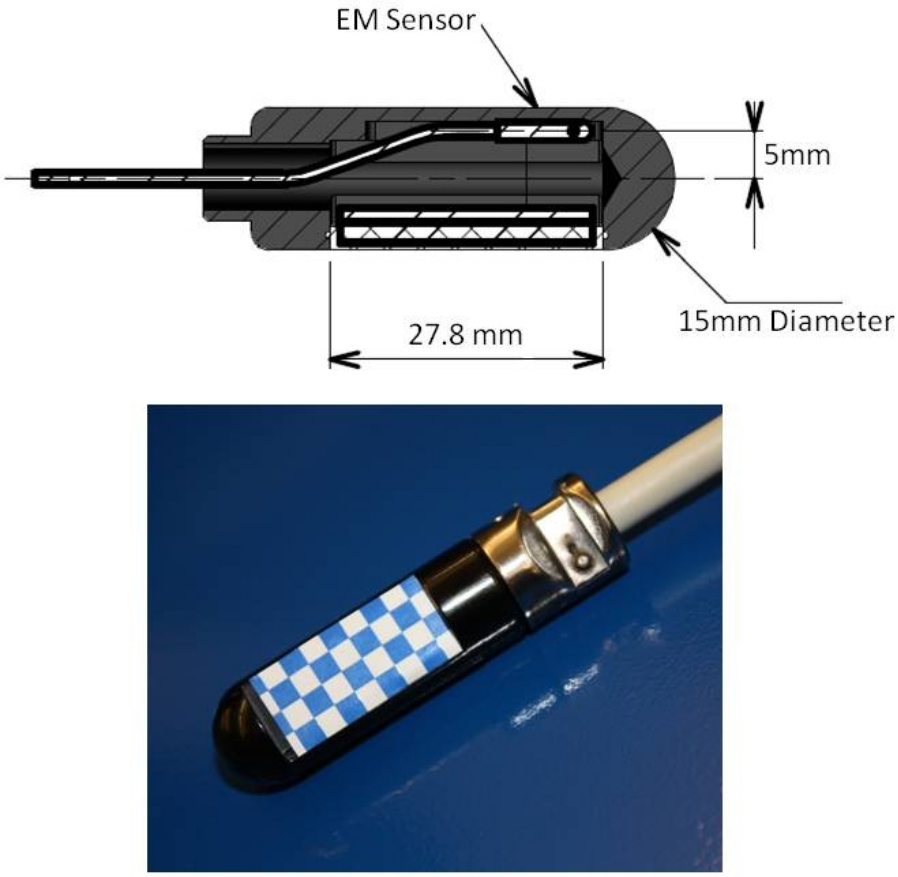

Figure 1.9: Top: Diagram showing the cross section of the "pick-up" transducer, and the location of the electromagnetic (EM) sensor and crystal stack. Bottom: a photograph of the ultrasound transducer, with checkerboards used for camera tracking.

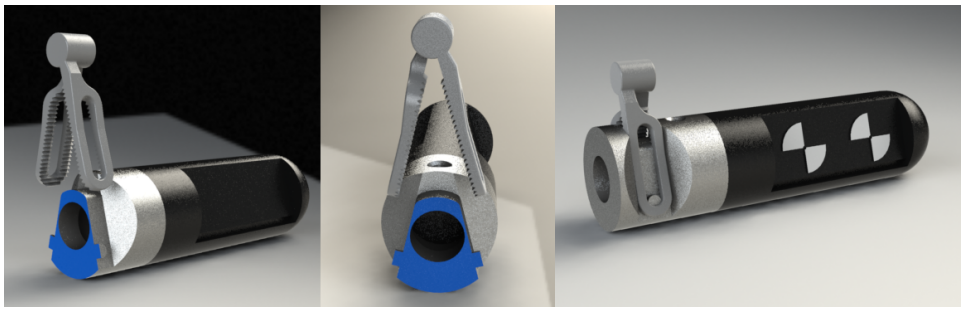

Figure 1.10: Rendered images of the "pick-up" transducer. Left and middle: cross sectional view (blue) of the lap-handle. The angled faces and locking pins can be seen. Right: the tool fits tightly against the angled faces. The practicality of adding visual tracking markers is demonstrated.

Figure 1.11: The pick-up intra-operative transducer is grasped and manipulated by the Pro-Grasp^{TM} tool of the da Vinci Surgical System.

the same incision. Thus, ultrasound is available throughout the operation without the need for tool changes and provides further surgeon autonomy. This minimizes the effect of using the transducer on surgical workflow.

1.6.5 Intra-operative Ultrasound Elastography

Using the transducer described above, 2D and 3D B-mode ultrasound images and volumes can be used during the procedure to provide the surgeon with additional guidance. In some cases, B-mode imaging alone of the renal tumor may not be

enough to provide the surgeon with adequate guidance.

23-46% of small renal cell carcinomas, those treated with partial nephrectomy, appear iso- or hypo-echoic in B-mode imaging [60]. This means that the boundaries of the tumor would be difficult to define, resulting in either positive margins (effecting patient outcomes) or more healthy tissue removed than necessary [91]. Renal tumors can also have complicated structures, including necrotic cores and fat tissues [59].

Ultrasound elastography has the potential to add contrast to imaging in order to better define the tumor boundary, as tumors are generally stiffer than the surrounding tissues [86]. This is particularly important when the tumor has a complicated structure.

In addition, elastography also has the potential to differentiate between benign angiomyolipomas and malignant renal cell carcinoma. The differences in stiffness of these two types of tumors could potentially differentiate them intra-operatively. Elastography imaging could also measure other tissue characteristics, just as viscous properties [154] or poroelasticity [84]. The fat content of the tumors might be measurable from elastography measurements. Elastography could also help distinguish hypoechoic cysts, where shear waves do not propagate, from other hypoechoic lesions.

The tissue characteristics determined from elastography, along with B-mode imaging, could improve intra-operative imaging guidance for surgeons.

1.7 Thesis Objectives

1. To use ultrasound and ultrasound elastography to better characterize kidney tissue for use in robotic-assisted surgical guidance and kidney transplant monitoring

2. To determine the tracking accuracy of the new intra-operative "pick-up" ultrasound probe previously built and tested. Looking at and testing three different tracking methods, including the robotic kinematics, electromagnetic tracking and stereo camera tracking

3. To use the "pick-up" ultrasound probe for the construction of 3D elastograms

that could be used in surgery

4. To determine tissue characteristics of the kidney. Previous research has produced very different quantitative measures of kidney elasticity. To examine the relationship between pressure and the elasticity properties and to estimate the viscous properties of the *ex-vivo* kidney by analyzing the frequency dependency of elasticity measurements

5. To measure the correlation of kidney health on the elasticity measurements of *in-vivo* transplant kidneys

1.8 Thesis Overview

Chapter 2 describes the experiments which test the tracking accuracy and reconstructions of the "pick-up" ultrasound probe. Three different tracking modes are tested and the accuracy of the reconstructions are tested against a known geometry of a vessel phantom.

Chapter 3 details the use of the "pick-up" ultrasound transducer for use in elastography. In this chapter, two sets of experiments are described. The first set of experiments uses the Clinical Mode of the da Vinci robot, where the surgeon still has direct control of the robot and ultrasound transducer and the second set of experiments leverages the ability to automate the robot using the da Vinci Research Kit.

Chapter 4 provides an in depth look at the current state of the art research in kidney elastography measurements. In particular, the different and varying results of previous studies are examined and also the complications in kidney imaging that have arisen from the different studies.

Motivated by the complications of kidney imaging, Chapter 5 examines two main features of kidney tissue. First, the relationship between blood pressure and measured elastography is investigated. The second experiment measures the viscous properties of the kidney. There is a distinctive relation between the excitation frequency (assuming a completely elastic tissue) and the measured elasticity, and by measuring at multiple frequencies, a model of the tissue which includes the viscous elements can be fit to the resulting data.

The next chapter of this thesis moves to the realm of *in-vivo* patient imaging. Elastography data using the SWAVE method is collected from kidney transplant recipients without biopsy. The initial study and results of four patients is presented in this chapter.

The final chapter of this thesis provides an overview of the work presented. The long term implications and limitations of the work are also discussed. Finally, the future of the work and possible improvements are considered.

Chapter 2

Ultrasound Transducer Tracking and 3D Reconstruction

2.1 Introduction

Laparoscopic MIS has become the standard of care for many abdominal operations. Benefits for the patient include lower morbidity and faster recovery time [47, 137]. However, MIS is more technically challenging for the surgeon, and this has historically limited the widespread adoption of laparoscopic approaches for complex surgical procedures such as partial nephrectomy. This operation is compounded by pressures including time constraints, restricted visualization, and elevated risks of bleeding [157].

As described in Section 1, knowledge of the vessels' location during the procedure would assist the surgeon in conducting a safer and more efficient dissection. Our center, Vancouver General Hospital (VGH), performs about 150 open or laparoscopic partial nephrectomy procedures per year, and 5 to 10 robotic procedures. We expect that a surgical navigational adjunct to robotic assisted surgery using the da Vinci, as proposed here will increase surgeon confidence, improve patient safety and decrease dissection time required for this operation.

With the increasing use of the da Vinci, better visualization and intra-operative

A version of this chapter was previously published [147]

imaging could be incorporated into the robotic procedures. As ultrasound is already regularly used during laparoscopic procedures, we focused on how ultrasound and ultrasound reconstruction could be integrated. An important application of ultrasound during laparoscopic procedures is 3D ultrasound reconstruction and mapping of the vasculature. Localized vessels can be used to define surgical planes and to register intra-operative images to pre-operative scans.

In this chapter, we describe the use of a novel, custom-designed intra-operative "pick-up" ultrasound transducer, described in detail in Section 1.6.4. We demonstrate that it can create 3D ultrasound volumes via transducer tracking methods and that the volumes can be used for pre-operative imaging registration. A preliminary study of the "pick-up" transducer was presented using one tracking method [143]. In this chapter, we study the accuracy of each of the three tracking methods used with this novel transducer and the potential for vessel reconstruction with each tracking method. These tracking methods include using the robotic kinematics, the Electromagnetic (EM) sensor and the stereo camera.

In particular, for registration, the 2D contours are combined to create a 3D model of the vessels and branches. The surface representations which are extracted from both the ultrasound images and pre-operative models can be registered. Due to the potential advantages that the transducer could bring to robot-assisted partial nephrectomy, this is the primary application discussed in this chapter.

2.2 Methods

2.2.1 Transducer Tracking

Localization and tracking of the ultrasound transducer can therefore be achieved using several different methods: robot kinematics [142], electromagnetic tracking [46, 83] and vision based tracking [133]. In addition, it is possible to create 3D volumes without any external tracking equipment, using such techniques as speckle decorrelation [5, 52].

For the "pick-up" transducer described in this thesis, three methods are used to track the transducer while inside the body: robotic kinematics, embedded electromagnetic tracker and stereoscopic vision. For this transducer, all of these methods

minimize the lever arm effects which can multiply error in calibration and tracking because the tracked sensor/element is very close to the ultrasound linear array and associated imaging plane. This effect is minimized by keeping the distance between the tacking point (the actual tool tip, the checkerboard or EM sensor) and the corner of the ultrasound image as short as possible.

Previous literature states that the expected accuracy of the da Vinci kinematics is approximately 1 mm, when tracking the activated joints of a single da Vinci arm using the clinically approved robot software [89]. In this situation, that accuracy compares favourably to other tracking techniques. The transducer can be grasped in a repeatable manner so that the transformation from robot to tool is fixed and known *a priori*. This is important because it would be impractical to do a calibration to calculate the transformation during surgery.

2.2.2 Repeatability Tests

To test the repeatability of grasping and to perform the optical tracking ultrasound calibration, a wide baseline stereo-camera was used. A checkerboard with 3.175 mm squares was placed on the transducer and instrument jaws and was tracked by the camera. The checkerboard was tracked using the wide baseline camera, which has a 75 mm baseline and consists of two Flea2 cameras (Point Grey Research, Richmond, Canada), each with a resolution of 1280 x 960 [43]. The intrinsic and extrinsic parameters of the wide-baseline camera and the location of the checkerboard on the tools within the camera frame were found using the Caltech Camera Calibration Toolbox [27].

Some studies claim that electromagnetic sensors have an accuracy of about 1% of the workspace [69], which, in this case, is approximately 0.5 mm. These tests were performed under optimal conditions; we would expect larger errors, more likely around 1 to 1.5 mm, due to the large metal objects in the operating room. In particular, the operating table and the da Vinci interfere with the EM sensor readings. The six degrees of freedom EM sensor is located within the body of the transducer as seen in Figure 1.9. It is close to the center of the transducer to minimize lever arm effects and maximize tracking accuracy with respect to the image plane. This sensor also does not interfere with the sterilization process as

the sensor is approved for use with the STERRAD system as well.

Another approach is to optically track the ultrasound transducer using the laparoscopic camera image(s). This has been done previously with a monocular laparoscope tracking a checkerboard pattern on an ultrasound transducer to create an augmented reality laparoscopic ultrasound system [133]. We used a stereo laparoscope and larger checkerboard pattern to do the same type of tracking. Specifically, we used a wide angle NTSC da Vinci stereo laparoscope from the da Vinci Surgical System (Standard). It has a baseline of 5 mm and a resolution of 720×486 pixels. The 6×2 checkerboard pattern on the pick-up ultrasound transducer had 3.175 mm squares. Camera calibration was performed using the Caltech Camera Calibration Toolbox [27]. The checkerboard tracking and stereo triangulation functions from the calibration toolbox were also used to track the checkerboard on the ultrasound transducer. This includes locating the checkerboard corners with a Harris corner detector and using the known geometry of the checkerboard to accurately determine the checkerboard pose. For each camera frame, the user selected the four extreme corners of the checkerboard to initialize the software.

In order to track the ultrasound image, a calibration must be completed to determine where the ultrasound plane is located relative to the respective sensor (da Vinci kinematics, EM sensor or stereo camera) [112].

N-wire calibration was used to calibrate the EM sensor and checkerboard to the ultrasound image. We used the PLUS framework for the EM sensor calibration [94] and a similar implementation in Matlab for the checkerboard calibration. EM sensor to ultrasound image calibration was completed away from large metal objects and other interference. The calibration of the stereo camera tracking to the ultrasound image was completed using the wide baseline stereo camera set-up previously described. Because locating an N-wire phantom within the reference frame of the da Vinci kinematics was particularly difficult, the transformation from the ultrasound image to the da Vinci tool was found through calibration using a single wall phantom [132].

2.2.3 Tracking Tests

Several tests will be undertaken to determine the accuracy of the different tracking methods.

First, before the da Vinci kinematics can be used for tracking, the grasping repeatability must be tested. The same wide baseline camera system that was described above was used to test the repeatability, so the error of the wide baseline camera system and checkerboard tracking also needed to be determined. To test this camera system error, two checkerboards were placed in a fixed relative position. These checkerboards were the same 3.175mm square pattern used for tracking the transducer. The Harris corner detection methods of extraction from the Caltech Camera toolbox used on the transducer and da Vinci tools were applied to these fixed checkerboards. Thirty images of the two fixed checkerboards in different poses were used to determine the camera repeatability. The error was calculated as the difference in the thirty resulting transforms.

For testing the grasping repeatability, the transducer was picked up 30 independent times (released and picked up again) using the robotic instrument. Images were saved from the stereo camera and the transformation between the tool and transducer was determined for each of the 30 trials [Figure 2.1].

To understand the errors present in the different tracking methods, we performed hand-eye calibration using the Kronecker product implementation [152], solving the system $AX = ZB$. Using the EM sensor and da Vinci robot as an example, A is the set of 4×4 matrix transforms corresponding to the location and orientations of the EM sensor with respect to its transmitter base and B is the collection of homogenous transformations of the tool tip with respect to the robot base. We then solve for X, the transform between the tool tip and the EM sensor and Z, the transformation between the robot base and the EM transmitter base. Z is subject to change with changes in the experimental set-up, but X should be consistent as the transformation between the da Vinci tool tip and the EM sensor inside the ultrasound transducer is repeatable, as described above. The position error is defined as the Cartesian distance between points in B and in the points defined by the transform: $Z^{-1}AX$.

We use the Optotrak Certus Motion Capture System (Northern Digital Inc.,

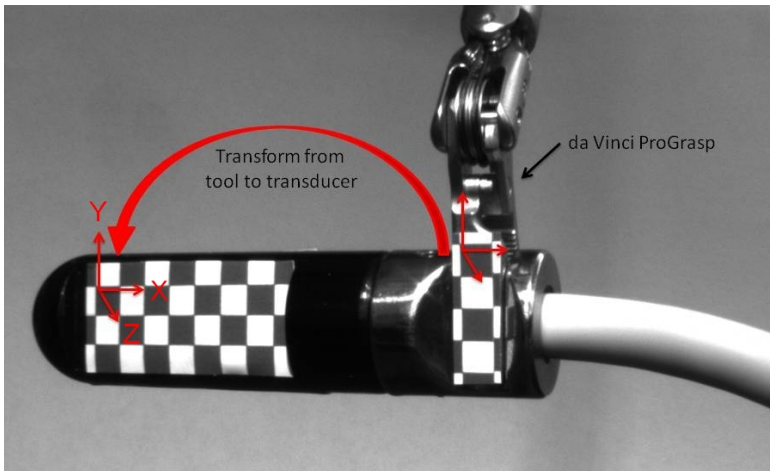

Figure 2.1: Grasping Repeatability testing set-up. The transducer was picked up 30 independent times and the transformation between the checkerboard on the tool jaws and on the transducer was calculated.

Waterloo, Canada), as the ground truth during these experiments because it is a tracking system that uses active Infrared Light Emitting Diode (IR LED)s, has an accuracy of 0.1 mm and resolution of 0.01 mm over its working volume [138]. A rigid body with four active infrared Light Emitting Diode (LED)s was attached to the transducer and the transducer was moved through 75 to 100 poses while grasped by the da Vinci. Three sets of data were collected with slightly different experimental set-ups and for each set, X and Z were calculated. Three hand eye calibrations were completed with this data, the da Vinci and EM sensor, both with respect to the Optotrak and the da Vinci to the EM sensor. Finally, because of differences in the experimental setup, we compared the tracking accuracy of the da Vinci stereo camera tracking to the Optotrak. In order to complete this, a rigid body of Optotrak markers was created surrounding a checkerboard of the same size and dimensions as the one attached to the transducer. Two sets of data of 100 poses were collected.

2.2.4 Image Processing, 3D Reconstructions and Registration

The contours of the vessels within the ultrasound images of the reconstructed volume were segmented manually for each of the 18 volumes (6 da Vinci kinematics,

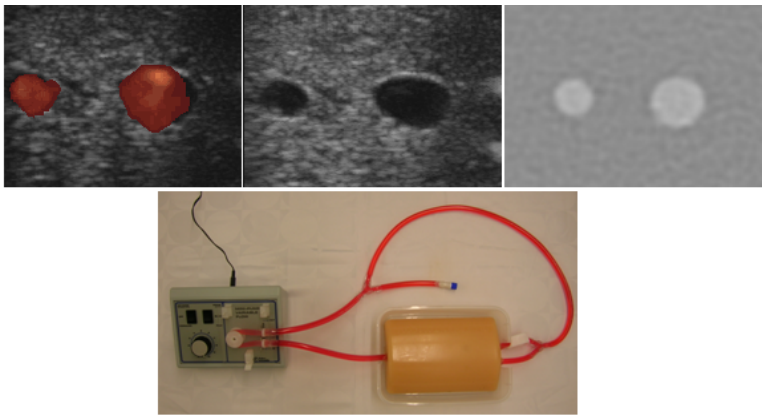

Figure 2.2: Vessel Phantom. Top left: B-mode, top right: CT, bottom left: Power Doppler and bottom right: Phantom photo

6 EM, and 6 stereo camera) after reconstruction. Once the contours from each image are found, a surface was created from the points on the surface of vessels using regularized marching tetrahedra [171]. Segmentations were all completed by the same person for consistency and to minimize bias. This surface structure was then used for registration with a previously created surface representation of the vessel structure created from pre-operative imaging. In this case, pre-operative CT scans of the phantom were used and contours were created through manual segmentation. A custom designed flow phantom (Blue Phantom, Redmond, WA) was used during the experiments [Figure 2.2]. This phantom consists of a single vessel which branches once midway through the phantom. The vessel diameter varies from 4 to 6 mm.

The surface-to-surface registration was completed using Principal Component Analysis (PCA) [11] followed by ICP [22]. Ball bearings were placed under the vessel phantom during the CT scans and subsequent ultrasound scans be used for registration validation. To validate the reconstructions, the distances between the ball bearings in the CT scan (#1 to #2, #1 to #3 and so on) were compared to the distances between the bearings in the ultrasound volumes. To verify the registrations, the distance between corresponding ball bearings was calculated, and the Dice coefficient [32] and volume error (the difference in the two overall volumes) were also calculated. The distance between corresponding ball bearings is defined

as the Target Registration Error (TRE). In addition, the average distance was calculated between every point on the CT surface and its closest counterpart on the reconstructed surface.

Table 2.1: Standard deviations of the fixed checkerboards, used to determine the repeatability of the wide baseline optical camera tracking system.

	Roll	Pitch	Yaw
Angles (deg)	0.13	0.15	0.07
	X	Y	Z
Translation (mm)	0.012	0.010	0.02

2.3 Results

2.3.1 Repeatability

First, the tracking error of the wide baseline camera system needed to be determined. The standard deviations for the three Euler angles and Cartesian components of the transforms resulting from testing two fixed checkerboards are shown in Table 2.1. The axis are defined on Figure 2.1, roll is the rotation around the Z axis, pitch, the rotation around the X axis and yaw, the rotation around the Y axis.

From the 30 release and capture trials, a transformation between the tool jaws and the ultrasound transducer was calculated using the position of the checkerboard markers in the frame of the stereo camera [Figure 2.1]. The transformations were converted to rotations and positions and centered on the mean values. The distributions of these values are shown in Figure 2.3.

The grasping repeatability results demonstrate repeatability better than the accuracy of the da Vinci kinematics and the EM tracking and approaches the accuracy of the checkerboard tracking itself. This shows that the ability to grasp the probe is repeatable and the transformation between the tool and the transducer can be considered fixed.

2.3.2 Calibration

The results for the ultrasound calibration using the da Vinci kinematics, EM sensor calibration and stereo camera laparoscope tracking are described in turn. For each sensor, a slightly different measure of calibration accuracy was used. For the da Vinci kinematics calibration, the residual error using a single wall phantom was 2.2 mm, averaged over three calibrations using 60-65 images. For the EM sensor calibration, the re-projection error for EM sensor calibration using the N-wire phantom was 0.94 mm, using 200 calibration images. The re-projection error is the difference in position of the N-wires, projected using the calibration matrix compared to the segmented N-wires in the ultrasound images. For the stereo camera to ultrasound image calibration, the pinhead Point Reconstruction Accuracy (PRA) was 1.3 mm. The point reconstruction accuracy is the Euclidean distance from the average of the estimated pinhead location to the actual pinhead location. The estimated pinhead location was determined by segmenting the pinhead from the ultrasound image and transforming that point to the stereo laparoscopic coordinate system. The actual location is the location of the pin, as seen by the stereo laparoscope, after the fluid in the ultrasound imaging bath is drained. During calibration, Edgcumbe *et al.* used a wide baseline camera to track the ultrasound transducer, an N-wire phantom for ultrasound calibration and the da Vinci stereo laparoscope was used to determine the accuracy of the calibration [43]. 30 and 22 transducer poses were used for ultrasound calibration and calculating the PRA respectively.

Since there is an unknown amount of error between the EM sensor measurements and the da Vinci kinematic measurements, both were compared to the NDI Certus Optotrak. Table 2.2 shows the mean position errors and standard deviations for three calibration set-ups using 50, 75 and 75 poses for the calibration data respectively and 15, 25 and 25 separate, unique poses for the test data. The results presented are mean and standard deviations of 50 randomized iterations of the calibrations and tests, such that the poses in each data set were randomly assigned to calibration or test sets.

One hundred poses of a rigid body were also collected with both the da Vinci stereo camera and the Optotrak. The data was separated randomly into 75 poses to be used for the hand-eye calibration and 25 poses to be used for testing. Fifty

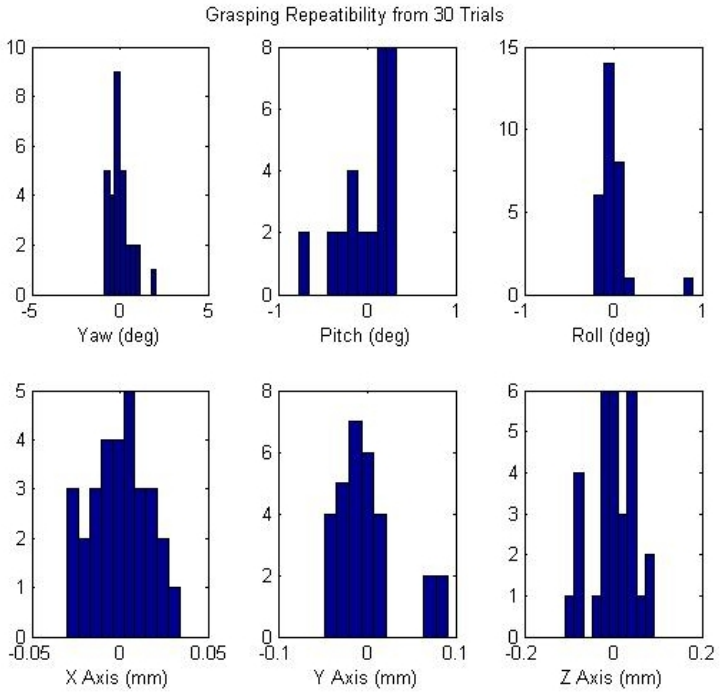

Figure 2.3: Grasping Repeatability. The mean-centered components (centered at zero) of the transformation between the tool jaws and the transducer computed using stereo tracking. See Figure 2.1.

iterations of the hand-eye calibration were completed, in which the poses were randomly assigned to either the calibration or test sets. The average results of the 50 iterations are shown in Table 2.3.

2.3.3 3D Reconstructions and Registration

We created 3D ultrasound reconstructions of a vessel phantom using the EM sensor, da Vinci kinematics and stereo camera tracking systems. With each system, six volumes were reconstructed and registered to the CT scan of the same vessel phantom. The contours in each image were segmented manually using B-mode images. The ball bearing fiducials were located and the distance between each fiducial was calculated and compared to the distances from the CT volume. The mean error and standard deviations between the bearing locations for each tracking modality

Table 2.2: Position Errors for Hand-eye Calibration between the da Vinci (dV), electromagnetic sensor (EM) and Optotrak

Data Set	Mean and Standard Deviation (mm)		
		Calibration Data Error (mm)	Test Data Error (mm)
1	dV to Optotrak	2.6 ± 1.8	2.5 ± 1.9
	EM to Optotrak	5.6 ± 2.9	5.5 ± 3.3
	dV to EM	7.9 ± 3.1	7.7 ± 3.5
2	dV to Optotrak	3.5 ± 2.5	3.7 ± 2.6
	EM to Optotrak	6.8 ± 3.2	6.9 ± 3.5
	dV to EM	10.7 ± 4.6	10.8 ± 5.1
3	dV to Optotrak	3.2 ± 2.3	3.3 ± 2.4
	EM to Optotrak	5.9 ± 2.9	5.9 ± 3.2
	dV to EM	10.1 ± 4.2	10.6 ± 4.4

Table 2.3: Position errors for the hand-eye calibration of the Optotrak and da Vinci stereo camera

Data Set	Calibration Data Error (mm)	Test Data Error (mm)
1	1.58 ± 0.92	1.62 ± 0.94
2	0.78 ± 0.54	0.82 ± 0.54

are shown in Table 2.4, Table 2.5 and Table 2.6. This error is a representation of reconstruction accuracy, while the TRE, the mean distance between corresponding fiducial bearings, represents the registration error.

The errors between the CT volumes and volumes created from the three sensors were also calculated. The volume error, the difference in the volumes of the CT and the sensor-based reconstructions, was calculated, as it was seen that the volume segmented from the ultrasound images was typically smaller than that of the CT scan. The relative volume error reported in Table 2.4, Table 2.5 and Table 2.6 is the ratio of the volume of the CT reconstruction and the reconstruction from the respective sensor. To find a measure of registration error, we used the Dice coefficient, which is twice the volume overlap divided by the sum of the two vol-

umes. Note that the Dice coefficients drop very quickly with errors in registration. For example, a mis-registration of 1mm along the x-axis of the CT volume with itself results in a coefficient of 0.8. Table 2.4, Table 2.5 and Table 2.6 outline the results from these volumes. Note that the volumes collected and reconstructed with each method correspond, *ie* volume 1 from the da Vinci and volume 1 from the EM sensor are the same volume, collected at the same time while the camera volume were collected separately and correspond to volumes 7-12.

Table 2.4: Reconstruction and registration errors for the volumes of the vessel phantom and targets collected with the da Vinci as a tracker.

Volume	Mean Target Spacing Error (mm)	Mean TRE (mm)	Dice Coefficient	Relative Volume Error (ratio)	Mean Closest Surface Point (mm)
1	2.8 ± 1.12	5.35 ± 1.88	0.41	0.60	1.33 ± 0.94
2	2.7 ± 0.98	5.45 ± 1.16	0.42	0.55	1.31 ± 0.87
3	2.8 ± 1.28	4.91 ± 1.25	0.49	0.57	1.18 ± 0.79
4	0.8 ± 0.64	5.97 ± 1.49	0.41	0.53	1.33 ± 0.93
5	2.68 ± 0.74	5.01 ± 2.74	0.54	0.51	1.01 ± 0.63
6	3.60 ± 1.37	5.73 ± 1.87	0.33	0.54	1.66 ± 1.29
Averages	2.56 ± 1.02	5.40 ± 1.73	0.43	0.55	1.30 ± 0.91

Table 2.5: Reconstruction and registration errors for the volumes of the vessel phantom and targets collected with the EM sensor as a tracker.

Volume	Mean Target Spacing Error (mm)	Mean TRE (mm)	Dice Coefficient	Relative Volume Error (ratio)	Mean Closest Surface Point (mm)
1	2.00 ± 1.20	8.05 ± 2.94	0.25	0.67	2.08 ± 1.53
2	1.49 ± 1.12	8.03 ± 1.97	0.23	0.86	2.49 ± 2.15
3	1.03 ± 1.05	6.9 ± 2.11	0.23	0.64	2.30 ± 1.96
4	1.38 ± 0.40	6.16 ± 1.95	0.21	0.61	2.48 ± 1.91
5	1.44 ± 0.33	6.09 ± 1.90	0.23	0.64	2.19 ± 1.68
6	1.41 ± 1.34	4.06 ± 1.33	0.35	0.55	1.71 ± 1.25
Averages	1.46 ± 0.91	6.55 ± 2.03	0.25	0.66	2.21 ± 1.75

Table 2.6: Reconstruction and registration errors for the volumes of the vessel phantom and targets collected with the stereo camera as the tracker.

Volume	Mean Target Spacing Error (mm)	Mean TRE (mm)	Dice Coefficient	Relative Volume Error (ratio)	Mean Closest Surface Point (mm)
7	2.30 ± 0.68	5.15 ± 1.49	0.29	0.49	1.92 ± 1.44
8	5.09 ± 1.16	8.52 ± 2.15	0.37	0.37	1.50 ± 1.22
9	2.47 ± 0.80	7.38 ± 2.54	0.43	0.57	1.65 ± 1.59
10	5.18 ± 2.76	6.39 ± 2.97	0.41	0.35	1.37 ± 1.03
11	5.53 ± 2.34	7.81 ± 1.60	0.45	0.27	1.36 ± 1.01
12	2.48 ± 0.80	4.59 ± 1.91	0.39	0.27	1.45 ± 1.06
Averages	3.84 ± 1.42	6.64 ± 2.11	0.39	0.39	1.54 ± 1.23

The vessel surfaces were registered using PCA and visual inspection was completed to verify that the surfaces were correctly registered and reconstructed. Figure 2.4 shows examples of the reconstructions using each tracking method and examples of the registration with a vessel reconstructed using the da Vinci tracking.

2.4 Discussion

We have presented tracking methods that make an ultrasound transducer useful during minimally invasive surgery. The three methods for tracking the transducer have been validated for a vessel phantom. The camera tracking has been independently validated by Edgcumbe *et al.* [43]. The transducer follows all the guidelines for intra-operative use and discussions with several surgeons have confirmed that this is a transducer they would like to use during their surgeries.

We were able to test the repeatability of grasping the transducer with the da Vinci tool and found that errors introduced by variations in the grasping were much smaller than the tracking errors introduced by the robot kinematics. In fact, the errors that were found between the tool jaws and the ultrasound transducer are close to those that were found between the fixed checkerboards, indicating that the grasping of the transducer is repeatable.

The results of the hand-eye calibrations are particularly interesting as they give a good indication of the errors introduced by the different tracking methods. The errors for the calibration between the EM and the da Vinci averaged 9.7 mm. It is not clear though, which tracking method is closer to the ground truth. When the two tracking methods were then compared to the Optotrak, which has much lower and known tracking error, the errors in the EM sensor calibration had an average of 6.1 mm while the errors between the da Vinci and the Optotrak had an average of 3.2 mm. The larger errors in the EM sensors could be related to the metal within the environment. In such situations, the operating room table and the da Vinci itself could contribute to warping of the EM fields.

The da Vinci camera tracking was also compared to the Optotrak and the average error between the Optotrak and the stereo camera positions was 1.22 mm. The data for this comparison was collected within the optimal distance range for the da

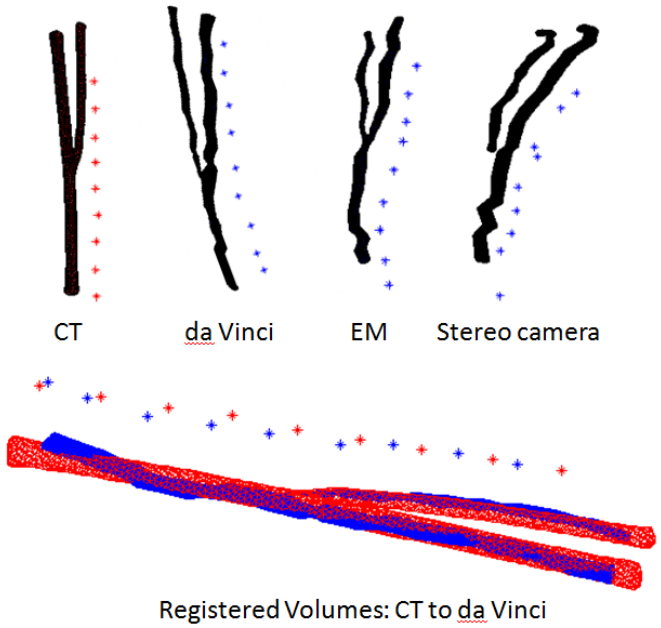

Figure 2.4: Top: Examples of the vessel phantom reconstructed from each modality, from left to right, the CT scan, the da Vinci kinematics, the EM sensor and the stereo camera tracking. The blue stars represent the locations of the ball bearing targets for each of the sensor based reconstructions. Bottom: An example of the CT volume registered with a volume reconstructed using the da Vinci kinematics. The red mesh and stars represent the surface of the CT volume and the ball bearing targets, while the blue mesh and stars represent the da Vinci reconstructed volume.

Vinci cameras, so larger errors are expected as the checkerboard is moved further from the camera.

The vessel reconstructions with the da Vinci had an inter-fiducial spacing error that was within the tracking errors of the robot and ultrasound calibration. Visually, the reconstructions looked correct, without major distortions in the vessel structure. The surfaces were well matched, as seen by the low closest point distances. The registration errors may decrease with a more rigorous registration method, or a more complicated vessel surface. The blood vessel phantom used for the experiments is Y-shaped and does not well constrain all the degrees of freedom,

presenting a challenging but anatomically realistic model.

The EM sensor had similar results for the reconstruction of the vessel phantom. The mean target spacing error was slightly lower than with the da Vinci, but the correspondence errors were larger. However, visual inspections of the volumes reveal larger distortions in the vessel structure than were seen with the da Vinci volumes. This is partly attributed to the larger closest point means and the large variations. The larger distortions are due to the EM environment around the da Vinci, as reconstructions performed in a metal-free environment did not display these distortions and were more consistent. Additional testing needs to be completed to determine the primary cause of the EM field warping. Warping of the EM field by the operating room table is static and warping from the moving da Vinci arms is dynamic. In the case of static warping, it would be possible to correct the distortions using one of the other tracking methods, either camera or kinematics with methods described by Kindratenko *et al.* [80]. In the case of warping from the operating room table, the use of a flat panel EM transmitter would negate some of the effects. The flat panel would be placed under that patient, blocking some of the effects from the table.

The reconstruction using the stereo camera had the largest mean spacing error and TRE. The reconstructed trajectory of the ultrasound and associated blood vessel path has several unexpected jumps that were caused by inaccurate optical tracking of the ultrasound transducer. These jumps are visible in the stereo camera reconstruction in Figure 2.4. Specifically, at the extreme ends of the vessel there are visible distortions. This is likely because the distance between the camera and transducer was outside the optimal distance for the stereo camera tracking. At one end of the vessel, it was inside the focal distance of the cameras and in the extreme lower corner of the images. At the far end, the checkerboard was very small in the images, limiting the accuracy of the corner detection. The distance between the camera and transducer, (z) was between 50 mm to 200 mm and the camera had a narrow baseline of 5 mm. Thus the depth to baseline ratio ranged from 10 to 40 during the experiment. The range of depth is significant because the 3D stereo localization error scales in a nonlinear manner (z^2) according to the following formula:

$$\delta z = \frac{-z^2}{fB} m \ , \tag{2.1}$$

where f is the focal length (pixels), B is the stereo baseline (mm), and m is the uncertainty in disparity (pixels). In Section 2.2.3, for a checkerboard at a depth of 10 cm from the camera, we calculated the accuracy of stereo point localization to be 0.8 mm. If we assume that all the error was caused by the uncertainty in disparity, then the point localization error is 0.2 mm and 3.2 mm at depths of 50 mm and 200 mm respectively. This corresponds with the range of error that was observed for the blood vessel surface reconstruction.

The three tracking methods each have advantages and disadvantages. The stereo camera tracking gives high tracking accuracy while the transducer is close to the camera, and has the benefit of being tracked directly in the camera frame, making integration of augmented and virtual reality relatively simple. However, it has the disadvantages that the markers must be visible in the camera and clean. This will be most accurate early in the surgery, but may become obscured later. Another disadvantage is the limited angle for which they can be seen by the camera; the markers on the transducer can only be accurately tracked when they are facing the camera. There will be times during the procedure when the markers will not be visible.

On the one hand, the EM sensor has the disadvantage that it may be warped by the electromagnetic fields and metal objects in the surgical environment. On the other hand, it has the advantage that the transducer can be tracked anywhere in the surgical field, even when out of view of the camera. We hypothesize that it can be used to direct the surgeon to the location of the transducer, through the use of on-screen cues, if the transducer were to be placed somewhere outside the camera's view.

The robot kinematics has high accuracy and can be used throughout the surgery without any degradation in tracking accuracy. It should be noted that this accuracy is only valid for the activated joints on a single arm; the errors in the set-up joints of the da Vinci can be very large as different types of potentiometers are used in these joints. In order to use the kinematic tracking (or the EM sensor) for augmented reality, the tracking coordinate frames need to by registered at the beginning of the

surgery, likely using a hand-eye calibration method. We may be able to use the stereo markers to calibrate the other trackers to the camera frame and un-warp the inconsistencies in the EM field.

By appropriate decision making throughout the surgery to determine which tracking methods to use, on their own or in combination, we will provide the surgeon with the best possibly localized ultrasound image.

For the remainder of this thesis, the da Vinci kinematics alone will be used to track the ultrasound transducer. The da Vinci kinematics offer an acceptable accuracy over a large working volume, can be read in real-time during imaging, and are not affected by the metal objects in the room or the angle of transducer with respect to the camera. These practical considerations along with the accuracy of the reconstructions, mean that the da Vinci kinematics were the best choice for tracking the transducer at this point.

2.5 Conclusion

The transducer tracking techniques presented in this chapter are applicable to an ultrasound transducer that can be easily grasped, aligned and released. In addition, the grip on the transducer is stable and repeatable, less than 0.1 mm and 0.2 deg, enabling the use of the robot kinematics to track the transducer and create accurate 3D ultrasound volumes as it is maneuvered using the da Vinci Robot. The three tracking methods allow for volume reconstruction when tested using a vessel phantom with internal targets.

Chapter 3

Elastography using the da Vinci Surgical Robot

3.1 Introduction

An increasing number of surgeries are being carried out as minimally invasive surgeries. During this type of surgery, surgeons have limited haptic feedback, since they can only touch the organs with the distal ends of long surgical instruments that must pass through the patient's abdominal wall. This configuration creates interference from friction at the trocar (the device that allows the instrument to be inserted in the body during laparoscopic surgery) as well as a fulcrum effect in which the tool tip moves in the opposite direction to that of the surgeon's hand.

In order to mitigate some of these challenges, surgical robots have been introduced and the most widely used laparoscopic robotic system is the da Vinci Surgical System (Intuitive Surgical, Sunnyvale, CA). The da Vinci Surgical System has overcome some of the challenges of MIS by offering the surgeon a stereoscopic vision system for 3D viewing of the surgical scene and increased tool dexterity. Both of these innovations improve the surgeon's performance [68], but the issue of haptic feedback remains unsolved. In fact, while surgeons using traditional MIS tools had limited haptic feedback, the surgeons using the da Vinci have no haptic

A version of this chapter was previously published [144]

feedback. The da Vinci tools have no force sensors and the surgeon receives no force feedback. Thus, during da Vinci robotic surgery, the surgeons rely solely on visual cues to estimate the forces they exert on the tissue.

Robotic systems have been used to measure and recreate manual palpation sensations in an attempt to solve the ongoing issue of haptic feed back during minimally invasive surgery [165, 166]. Graphical displays can also be used to replace direct haptic feedback [180]. Adding force sensing and haptic feedback to the da Vinci robot have been shown to allow for lower and more controlled forces to be applied to the tissue and suture [114, 120, 121]. The addition of force sensing can be used for vessel and tumor identification [108, 165]. Adding force sensors to the da Vinci tools can be difficult from a practical standpoint due to the sterilization process and the fact that the tools are disposable. Using motor torques as a force surrogate is also more difficult in this environment due to the fact that the da Vinci robot uses cables to control the end effector, which can stretch over time.

We believe that ultrasound elastography is a promising alternative to direct force sensing. Ultrasound elastography provides a full image of tissue stiffness and viscous properties – the very properties that surgeons try to measure during manual palpation. Conventional ultrasound has been integrated previously into the da Vinci Surgical System using multiple types of ultrasound transducers [28, 143, 179].

We have identified the two major uses of haptics needs for minimally invasive surgery to be tumour and vessel palpation (Section 1.6.3). In open surgery, the surgeon uses his/her fingers to feel the underlying vessels, through their compliance and pulsatile motion. In contrast, surgeons using the da Vinci robot cannot feel tumors and vessels because the da Vinci robot does not collect or transmit this information.

The absolute elastography technique is a promising adjunct for a broad range of surgeries; quantitatively measures the Young's Modulus rather than a relative value in comparison to the surrounding tissue. For radical prostatectomy, it will help delineate the prostate gland and the tumours within it. For partial nephrectomy, it will help navigate towards the kidney and delineate the tumour boundary. For liver surgery it will help determine appropriate ablation boundaries. Once an elasticity map of the tissue is constructed, haptic feedback based on deformation simulation can also be provided without affecting the da Vinci teleoperation system stability.

Previous ultrasound elastography with the da Vinci robot has been primarily based on *strain* imaging. Ultrasound strain imaging, which provides images of relative tissue deformation in response to various compression levels applied by the ultrasound transducer [123], has also been integrated with the da Vinci Surgical System [24]. That system uses the 'Read-Write' API [38] to overlay a palpation motion onto the movements of the surgeon. The API is an interface with the clinical da Vinci software.

This removes some of the user-related difficulties of creating quality strain images by moving the transducer with a known amplitude and frequency. Strain imaging can be used to determine the tumour extent and for image registration [158]. Because of the oversimplified assumption of a constant stress field, strain images often contain artifacts caused by tissue inhomogeneity and stress concentration. Strain images are also more affected by boundary conditions.

This chapter demonstrates the feasibility of obtaining absolute elastography by using the da Vinci robot in order to create an environment in which the surgeon is able to estimate the tissue stiffness during robotic surgery. An external exciter is used to induce low frequency vibrations at multiple frequencies into the patient's body, while a 2D intra-operative transducer [143] acquires 1D axial displacement amplitude and phase over a given volume. These displacements are then used to create a 3D displacement volume used to calculate the elastic properties. Different than calculating the elastography from each planar 2D ultrasound image, and then creating a volume, measuring the displacements of volume allows for a more accurate measurement of the wavelength through the tissue, and thus a more accurate measurement of tissue properties.

The first section describes a method of 3D elastography that uses the clinical da Vinci software, but is a bit more cumbersome for the user, as the user must move the transducer slowly over the given region of interest. The second section of this chapter proposes a novel, 3D absolute elastography method with external excitation that is suitable for the da Vinci robot using the da Vinci Research Kit (dVRK). The DVRK and a da Vinci "Standard" (1^{st} generation) robot system [33, 79] are used to determine the position and orientation of the ultrasound transducer so that the displacement phasors are acquired at known 3D locations. More specifically, as the surgeon traces out a trajectory, equally spaced ultrasound images are reconstructed

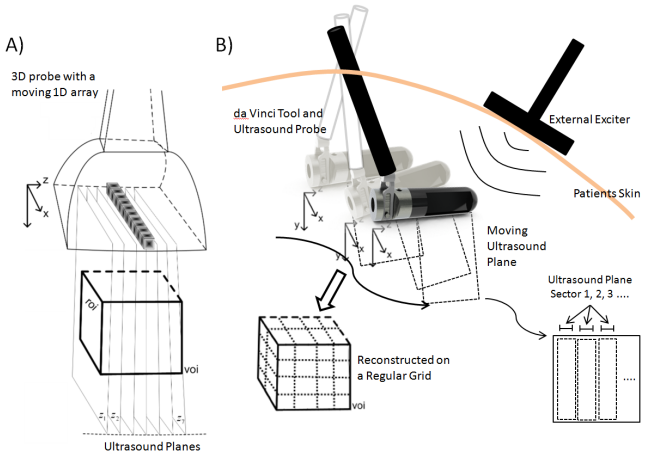

Figure 3.1: A) Elastography set-up for the 3D transducer method. B) Set-up for the extension to freehand scanning using a 2D transducer and the da Vinci robot. In both cases, sector subdivision high-frame rate imaging is applied.

into a regular 3D volume when the DVRK traces out the surgeons trajectory in reverse, under autonomous control.

These experiments represent the first time that 3D ultrasound elastography volumes have been created using a freehand scanning or automated freehand techniques. This process requires that the imaging be synchronized with the transducer motion in order to accuracy capture the tissue displacements. It requires that transducer position be tracked accurately in order to create a 3D volume of displacements. The methods and results presented here represent a step forward for elastography imaging, expanding the applications to intra-operative procedures and other freehand imaging.

3.2 Elastography

In these experiments, the SWAVE elastography system was used, along with a software interface, eScan, developed in our laboratory and described in detail in Jeffrey Abeysekera's doctoral dissertation [3]. This elastography system was described in more detail in Section 1.4. This system is generally based on the idea of inducing mechanical vibrations into phantoms and tissues using an external excitation

source. Here, sector based imaging was used to image the wave displacements at high frame rate.

3.3 Experiment 1: Freehand Technique in Clinical Mode

A mechanical 3D transducer has been used previously to capture a 3D volume of tissue displacements [Figure 3.1A] [14]. Such a transducer mechanically sweeps a 1D crystal array to create regularly spaced ultrasound planes, but can be large and bulky. In this chapter, we describe the use of a tracked 2D transducer (the transducer described and characterized in Section 2 to create the same type of 3D volume [Figure 3.1B].

The custom-designed transducer creates a static and repeatable transform between the da Vinci tool (Prograsp) and the ultrasound image. The transducer has 128 elements, is 28 mm long and is operated at 7 to 10 MHz (Section 1.6.4). For this study in this Chapter, a sector size of 8 crystals and a sector frame rate of 625 frames per second was used (Figure 1.5). The tool-to-image transform was found using the single-wall phantom method implemented in Stradwin [132].

To synchronize the external exciter with the ultrasound image acquisition, the surgeon using the transducer triggers the image capture by using the clutch pedal in the robot console, an event captured by the da Vinci API. This approach has the benefit of keeping the ultrasound transducer still while imaging takes place but has the drawback that it interferes with the natural, smooth motion of ultrasound scanning. See Section 3.5 for methods of improving upon the natural movement limitation.

Image acquisition begins with the collection of Radio Frequency (RF) data along the axial direction of the ultrasound image. The RF data is used to compute the displacement phasors $\hat{u}(x, j\omega)$ from equation 1.3, at all depths in the image with respect to the transducer face. When a full volume of displacements phasors is captured, typically 15-30 frames, the real and imaginary parts of the axial displacement phasors (scalar values) are reconstructed into a volume on a regular grid. The volume reconstruction is performed using the Public Library of Ultrasound (PLUS) software architecture [95] and uses linear interpolation between points for the real part and the imaginary part of the estimated displacement phasors. The field of

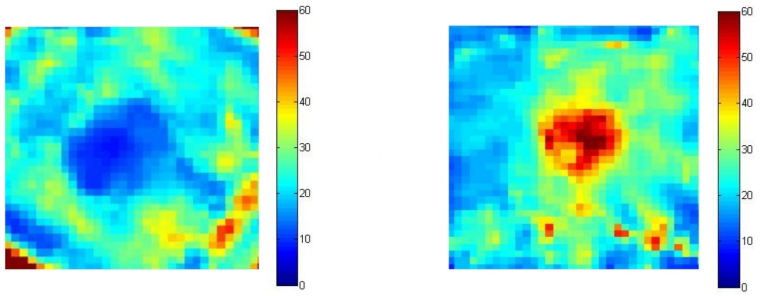

Figure 3.2: Left: Image of 6 kPa CIRS phantom lesion. Right: Image of the 54 kPa CIRS phantom lesion. The colour bar shows the elasticity in kilopascals (kPa).

view with an intra-operative transducer is small, about 30 mm by 30 mm. The absolute elastic properties of the samples are found from the grid displacements using local frequency estimation (Section 3.2). This final volume of elasticity can be displayed to the operating surgeon or used to create a local model for haptic feedback.

3.3.1 Experimental Setup and Results

A CIRS Elastic Quality Assurance Phantom, model 049 (Computerized Imaging Reference Systems, Norfolk, VA), was used to evaluate the accuracy of the elastic properties found using this method. The soft (6 kPa) and stiff (54 kPa) shallow lesions were imaged against a neutral background (29 kPa). Image acquisition was performed simultaneously at four different frequencies: 180, 210, 230 and 270 Hz.

The soft and stiff lesions were imaged at a depth of 4 cm and a frequency of 7 MHz and the resulting elastograms are shown in Figure 3.2. The diameter and average elasticity were measured in two images (corresponding to the middle of the lesion) for 5 trials for each lesion. The diameters of each lesion were also measured using the caliper function of the ultrasound software [Table 3.1]. The results for the stiff lesion were within 6% error of the manufacturer's specifications and within 4% of the values found using MRE on the same phantom model [13]. The softer lesion was stiffer than the manufacturer specified value but within 2% of the values reported with MRE. The results achieved through freehand ultrasound

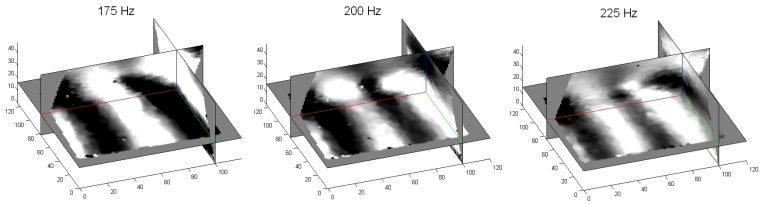

Figure 3.3: A series of phasor volumes for the same trajectory in the CIRS phantom, of the stiff lesion. The different wave patterns can be seen at each different frequency.

elastography are repeatable, with narrow standard deviations in both the diameter measurements and the elastic properties.

Table 3.1: Results from the CIRS QA Elastography Phantom

	Diameter of Soft Lesion	Diameter of Stiff Lesion
B-Mode	8.9 ± 0.6 mm	10.8 ± 0.2 mm
Elastogram	10.4 ± 1.6 mm	10.7 ± 1.6 mm
	Elasticity of Soft Lesion	Elasticity of Stiff Lesion
Manufacturer Specifications	6 kPa	54 kPa
MR Elastography [13]	11.1 ± 2.1 kPa	49.4 ± 16.9 kPa
Freehand Elastography	10.9 ± 0.6 kPa	51.1 ± 5.2 kPa

3.4 Experiment 2: Automated 3D Elastography with DVRK

3.4.1 Robotic Integration

In previous work on SWAVE, a 3D motorized ultrasound transducer has been used to create 3D volumes of tissue elasticity [4, 12]. These types of transducers tend to be large and there are none designed for intraoperative use. Instead, we have designed a custom ultrasound transducer that is controlled by a da Vinci surgical robot also described in Section 1.4 and shown in Figure 3.4 [143, 147].

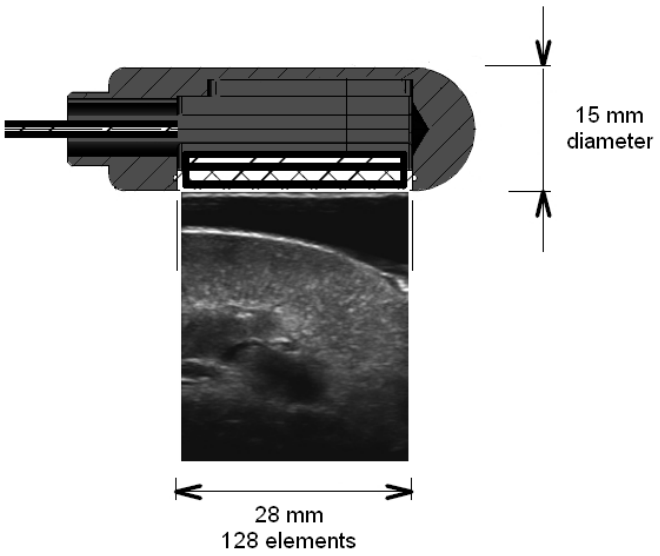

Figure 3.4: The transducer used in this study was custom designed for use with the da Vinci Robot [143]. It has 128 elements, an imaging face that is 28 mm wide and a diameter of 15mm.

In order to create accurate 3D volumes of the area of interest using the da Vinci robot, the DVRK is used to control the position and orientation of the tool and thus the location of the ultrasound transducer and image [33, 79]. In order to create accurate 3D elastic reconstructions, the transducer must be held still during each individual image acquisition within a volume, as the displacements in an image plane must be captured over several phases of the excitation signal. A further description and accuracy assessment of the DVRK is given in Appendix A.1.

The DVRK is used to record the desired trajectories traced out by the surgeon. The surgeon moves the transducer over the surface of a given area of interest in standard teleoperation mode, while the robot records the motion. Using this learned trajectory, the robot is commanded to recreate the trajectory, stopping at given locations to capture images with more regular spacing. A spacing of approximately 0.5 mm is used.

Within an ultrasound image, the displacement can only be accurately measured along the axial direction, which has the highest resolution, since it is the direction

of the transmitted and received acoustic waves. When measuring the tissue displacements, it is best if the axial directions of each image are approximately in the same orientation. In using axial ultrasound displacements, only a single component, or projection, of a three dimensional wave is measured. If this component is changing throughout the acquisition, it is very difficult to reconstruct the wave amplitude, since we do not collect overlapping data. Thus, since the reconstruction is based on Helmholtz's equation (1.3), the most accurate reconstruction is achieved if the planes are parallel.

Because the trajectory recorded from the surgeon may have changes in the axial direction, the trajectory that is given back to the robot aligns the axial direction of each plane, while covering the same volume (Figure 3.1). In order to compensate for the changing axial direction of the phasors, the average axial direction of the image plane is found over either the volume or a sub volume depending on the total size and directions of the images. The average orientation is applied to each transformation of the desired transducer trajectory. The desired trajectory of the transducer passed to the da Vinci robot will have all the axial directions aligned. The average rigid transformation of all the recorded orientations is found using an algorithm based on Kavan's method as described in [78].

The DVRK and the elastography software on the ultrasound machine communicate through TCP/IP sockets. The resampled trajectory is loaded into the ultrasound machine and before a new displacement plane is captured, the software commands the robot to move to the next desired position. The robot is allowed some time to complete the motion (usually 1 second as the motions are small) and returns its 'achieved" position. Through this communication, the software records the actual achieved position and orientation of the robot for every image.

At each 3D location, 25 images are collected at an effective high frame rate, using the sector based method described above. The tissue displacements between these 25 images are found and the phasors are calculated at each of the desired 3D locations [187]. Using the measured trajectory locations from the DVRK, the phasors are reconstructed on a regular grid using the PLUS software architecture [95]. Reconstruction is completed for the real and imaginary part of the displacement phasors to recreate a volume where each value is located in its correct geometrical location in 3D. LFE was then used on the 3D volume to estimate the absolute value

of the tissue Young's modulus [81].

3.4.2 Experimental Setup

Two sets of experiments were used to validate this method of elastography integration on the da Vinci robot. The first set of experiments use a CIRS Elastic Quality Assurance Phantom, model 049 (Computerized Imaging Reference Systems, Norfolk, VA). The phantom has embedded lesions of known stiffness and size that can be used to validate the accuracy of the elasticity. This phantom was used to validate the accuracy of the elasticity reconstructions.

The second set of experiments tested the system in *ex vivo* tissue. *Ex vivo* liver or kidney was purchased from a local butcher. The surface was arranged to mimic the surface curvature of the human liver or kidney.

CIRS Phantom Elastography Validation

From the CIRS phantom, 5 volumes were collected of the stiffest small spherical lesion and 5 volumes of the softest lesion. Each volume consisted of 30-50 image slices, enough to image the 10 mm lesion and some surrounding tissue. Each volume collected used a unique trajectory.

B-mode imaging was used to determine the size of the lesion and then a virtual sphere of that diameter was manually overlaid onto the elasticity volume. The elasticity values inside the sphere are then averaged to determine the value of the elasticity.

To determine the elasticity of the background, a similar method was used. In the B-mode image, an area of background was located, and the average elasticity within a sphere of 1.5 cm in diameter was calculated. This process was repeated at two separate locations for each volume and combined to determine the average background elasticity.

Because the elasticity calculation has been found to be dependent on the excitation frequency, we measured the values at several different frequencies using steady state excitation. For this phantom and transducer, the frequencies were: 175, 200 and 225Hz. The optimal frequencies of excitation depend on the tissue being imaged and the frame rate of the machine. It is also recommended to use multiple

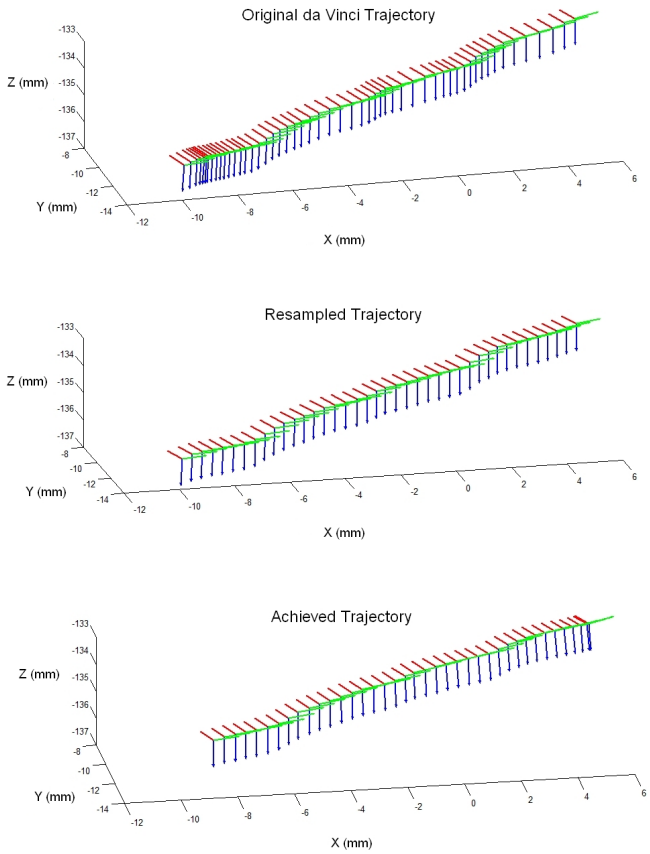

Figure 3.5: Example trajectory from the *ex vivo* kidney scans. The original trajectory of the da Vinci tool (top), the resampled trajectory (middle) and the achieved trajectory as reported by the da Vinci (bottom). All locations are reported in millimetres and the x, y, and z directions are indicated by red, blue and green lines respectively.

frequencies as some create nodal patterns in the tissue depending on the reflections. In addition, in places of very low displacement, such as the nodes, it is hard to determine the tissue motion. At different frequencies, the nodes appear at different physical locations and averaging over the frequencies allows the mitigation of any artifacts caused by the nodes.

As part of internal lab testing for accuracy and repeatability, the phantom was imaged with a 3D motorized transducer, using the same methods and software presented in this paper. The manufacturer values are also presented in the Table 3.2. In addition, we also compared the measured results with measurements taken with the Siemens Virtual Touch Image Quantification (VTIQ) system on a Siemens Acuson S2000 (Malvern, PA). This commercial system uses ARFI to measure tissue wave speed as described in Section 1.4. These wave speeds were then converted to elasticity measurements in order to compare with the other results. For these measurements, 14 individual locations were sampled for the stiff and soft lesions, as well as the background. The mean and standard deviation of these results are shown in Table 3.2.

Ex vivo Tissue

Volumes of two different tissue types were collected. Calf liver tissue was obtained from the butcher shop and fresh porcine kidney was procured from the hospital. The kidney was scanned at 175, 200, 225, 250 Hz, while the liver was scanned at 75, 100 and 125 Hz. The difference in excitation frequencies is due to the difference in expected elastic properties. The overall elasticity of the tissue will determine the shear wavelength within the volume, and it is desirable for accurate elastic measurements to have at minimum one wavelength within the area scanned. One wavelength is the minimum, but increasing the number of wavelengths within the volume will increase the resolution of the elastic measurements.

The set-up for both types of *ex vivo* tissue required that the tissue be restrained. The tissue was placed in a metal container lined with rubber designed to absorb ultrasound. This is needed to minimize the reflections that would have been caused by the container. A plastic film of the same type that is used in ultrasound transducer covers is placed over the tissue and held in place with magnets.

3.4.3 Experiment 2: Results

Unique tool path trajectories were created for each volume imaged. A subset of one trajectory is shown in Figure 3.5. The figure shows the original trajectory collected from the da Vinci and the resampled trajectory used as input during volume collection.

When comparing the resampled and the achieved positions and orientations across all the trajectories used in this study, the average angular error was 2.87 $\pm$ 0.55 degrees and the average translational error was 0.73 $\pm$ 0.18mm. The position error is defined as the 3D distance between the location of the tool tip in the resampled trajectory and the achieved trajectory. The angular error is defined as the average inverse cosine of the three primary axes. Figure 3.6 illustrates the position error between the resampled trajectory and achieved trajectory from Figure 3.5. The errors are small, but some bias can be seen. With a consistent bias, the reconstructed volume should not be affected.

The mean elasticity of the lesions in the CIRS phantom is found in Table 3.2 and compared to the previous results on the same phantom found using the same elastography processing techniques, but collected with a motorized 3D ultrasound transducer, specifically a 4DL14-5/38 transducer from Ultrasonix Medical. These previous results of internal lab testing for accuracy and repeatability. All results are given as *mean* $\pm$ *standard deviation* in kPa.

Table 3.2: The results of the elastogram volumes taken from CIRS phantom and compared to results of the same phantom captured with a 3D motorized ultrasound transducer, the Siemens VTIQ system and the manufacturer specifications

	Softer Lesion	Stiff Lesion	Background
2D and DVRK	16.1 $\pm$ 2.3	63.9 $\pm$ 6.4	38 $\pm$ 2
3D Motorized Transducer	9.5 $\pm$ 0.8	66.7 $\pm$ 0.8	29.3 $\pm$ 5
Manufacturer Specifications	6	54	29
Siemens VTIQ	12.78 $\pm$ 1.36	62.44 $\pm$ 10.7	28.4 $\pm$ 3.1
MRE [13]	11.1	49.4	22.3

The phasor images from each volume, which indicate the tissue displacement

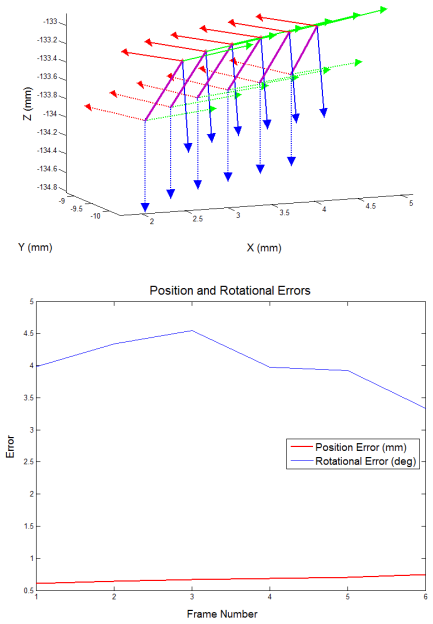

Figure 3.6: Top: The first six frames from the resampled trajectory and the achieved trajectory overlaid from Figure 3.5. The desired transforms are shown in solid lines, while the achieved transforms are shown with dotted lines. The magenta lines between the points indicate corresponding points within the trajectory. Bottom: A graph showing the values of the position and rotational errors for the six frames.

and thus wave tracking, were examined along with the resulting elastogram to validate a smooth reconstruction. The phasor images should show smooth waves that propagate throughout the volume. Any jumps or discontinuities will cause artifacts in the resulting elastogram. These jumps or discontinuities could be caused by gaps in the reconstruction or errors in the transducer tracking; they would be viewed by the algorithm as areas of high frequency change causing artifacts. One example of the phasors taken from the CIRS phantom at a 200 Hz excitation frequency and the resulting elastogram is shown in Figure 3.7. All elastograms of the CIRS phantom are shown on a scale from 0 to 60 kPa. The inclusion in this volume is clearly visible relative to the background within the phantom. All of the volumes imaged had similar contrast between the inclusion and the background.

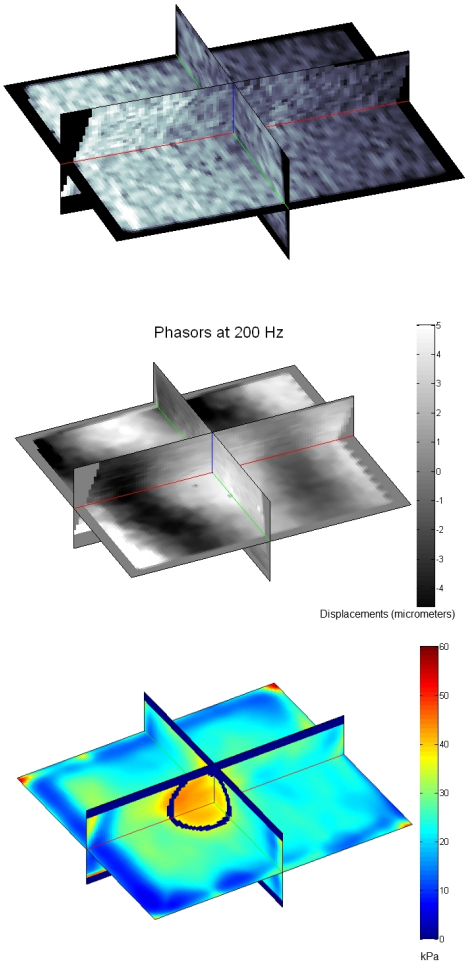

Figure 3.7: Results from the stiff lesion of the CIRS phantom. The reconstructed B-mode image of the phantom (top). The reconstructed real part of the phasor image (middle) and the resulting 3D elastogram (bottom). The blue sphere outline designated the area of the inclusion used to calculate the elasticity. Phasors are shown on a scale from -5 microns to 5 microns and the elastogram is shown on a scale for 0 to 60 kPa.

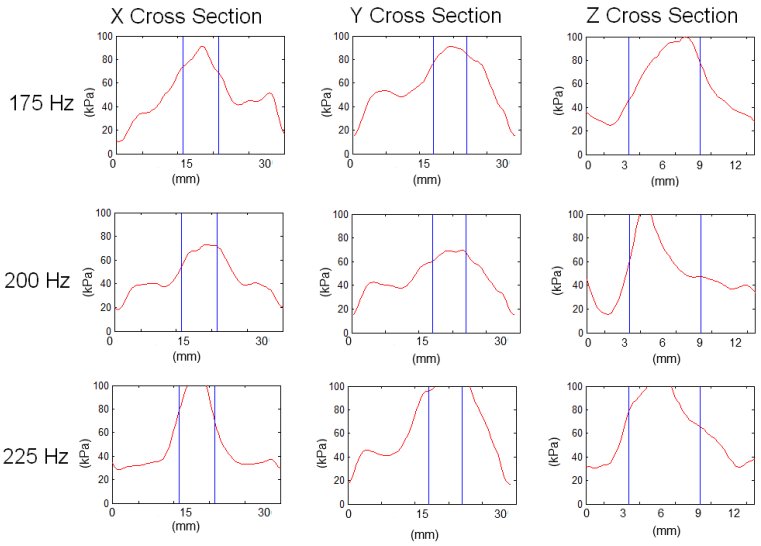

Figure 3.8: The cross sectional graphs of the elastogram taken through the center of the stiff inclusion in the phantom with the 2D transducer and da Vinci system. The red line is the calculated Young's Modulus and the vertical blue lines indicated the edges of the stiff inclusion.

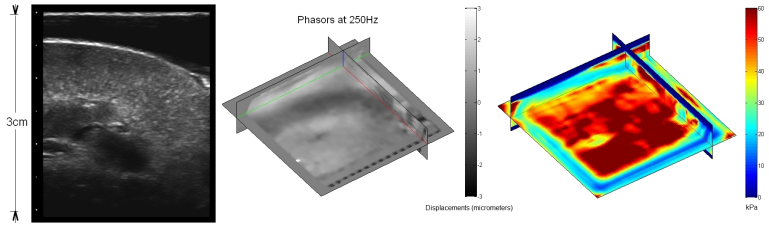

Figure 3.9: The B-mode (left), real part of the phasor image (center) and elastogram (right) of the *ex vivo* kidney. Phasors are shown on a scale from -3 microns to 3 microns and the elastogram is shown on a scale from 0 to 60 kPa.

To demonstrate that the method works on real tissue, *ex vivo* kidney and liver were scanned. The B-mode, phasors and elastograms are shown in Figure 3.9. The structure of the kidney is much more complicated than a phantom, causing different wave patterns. The central calyx of the kidney is still filled with urine and the vessels in the same area are filled with blood. As the fluid filled regions do not propagate shear waves, there is a lack of displacement data in that area. This lack of displacement causes the soft central region on the elastogram. In the phasor images, the upper surface of the kidney can be seen as the waves follow the cortex of the kidney.

The resulting measured Young's modulus of the upper half of the kidney was 37.9 kPa and the lower half of the kidney was 48.1 kPa.

3.5 Discussion

This Chapter presents two methods and associated results for 3D absolute elastography with a freehand scanning technique. Specifically, a small 2D intra-operative transducer allows robotic laparoscopic surgeons access to the elastic values of tissue. The results with freehand imaging and the clinical API are comparable to both those achieved with a mechanical 3D transducer [14] and within 5% of the results achieved with magnetic resonance imaging techniques [13].

The methods are currently implemented using the da Vinci robotic system but can easily be extended to any 2D transducer and any tracking system, such as electromagnetic or optical tracking systems. This would allow absolute elasticity values to be found in nearly every clinical setting. We have used the da Vinci robot as an initial platform for integration for several reasons; the robotic environment has the most room for improvement with regards to haptic feedback, and at the same time provides a stable and accurate platform for transducer tracking. The quality of the elastogram is dependent on the tracking error, which in turn depends on the tracker involved. Generally speaking though, if the planes are dense, a better elastogram is obtained, because of the higher signal to noise ratio due to averaging.

One current limitation of the method using the clinical API is synchronization of the imaging and the external exciter. This is currently addressed by using the clutch pedal in the surgeon's console to trigger imaging at a specified phase of the

exciter. But is addressed in a more comprehensive manner in the second method presented here.

The second method developed using the DVRK automates the scanning process. The robot is only automated on a path that is provided by the surgeon. The automation of the robot path allows for evenly spaced image acquisition and alignment of the axial direction, which is needed for accurate quantitative results. Automation of the imaging makes for reproducible results and makes the acquisition of data less dependent on the experience of the user. One remaining challenge is the introduction of automation into the operating room. The system currently relies on the use of the DVRK in order to automate the image collection process. This type of automation has not yet received regulatory approvals. In its current form, the system described attempts to minimize the potential risk to the patient, by keeping the amount of autonomous trajectory planning to a minimum, and keeping the autonomous trajectory in line with what was performed by the surgeon.

The resulting position and orientation of the achieved da Vinci trajectories match well the desired trajectories. Across all the trajectories used in this study, the average angular error was 2.87 ± 0.55 degrees and the average translational error was 0.73 ± 0.18 mm. Internal lab testing similar to that done by Kwartowitz *et al.* [89] as described in Appendix A.1, found that the DVRK has a target localization error accuracy of 1.16 ± 0.46 mm, over a total of 36 individual points. This means that the DVRK can localize the tool tip within 1.16 mm, so each achieved position has the possibility of deviating around 1 mm. The commanded trajectory of the DVRK had about 0.5 mm spacing between the Cartesian positions. Since there is some uncertainty in the location of the DVRK, as well as in the image calibration procedure, the close spacing of the imaging locations allows for some averaging in the case of errors. The larger angular error compared to that of the translational error could be attributed to the differences in controller gains on the DVRK. The DVRK uses a proportional, integral and differential (PID) controller to command the location of the position and orientation of the tool tip. For the studies in this paper, the gains on translational joints of the robot were set much higher than the gains for the orientation joints. This configuration of gains was found to allow normal teleoperation of the robot without causing instability within the system. Higher gains on the orientation joints were tried, but the system became unsta-

ble under normal teleoperation. In the future, we would like to tune the gains to achieve tighter bounds on the rotations.

The results of the elastography images compiled from multi-frequency sweeps of different phantoms and *ex vivo* tissue gives us high confidence in the usability of this method. The use of multiple frequencies diminishes the effects of nodes in the displacement measurements and allows for a more consistent picture of tissue elasticity. The reconstructed phasor images showed smooth wave patterns consistent to what is seen using the 3D motorized transducers.

The results of the elastograms created with the DVRK were slightly biased compared to those that have previously been acquired from the same phantom using a more conventional, constrained 3D motor sweep. Recent results taken with the 3D motorized transducer for the same phantom and using the same algorithms, are indicated in Table 3.2. In general the results found with the 2D da Vinci transducer were about 6 kPa higher for the softer lesions than those found with the 3D motorized transducer, but about 3 kPa lower for the stiffer lesion. The bias of the results could be due to a range of possible errors, some of these include errors due to calibration, DVRK tracking, and irregular spacing. These errors could also lead to larger variance in the elastic measures, but the variance remains small relative to the mean. Most important, these results show that it is possible to create 3D quantitative elastograms with robotic automation, but some differences still exist and further testing is needed to investigate and these differences further.

When comparing the results of the da Vinci method with those of the manufacturer and the VTIQ system, there is an issue with averaging over the volume of the inclusion. The VTIQ measurements are taken as point values, near the center of the inclusion, while the presented values using the da Vinci robot system are averaged. Looking at the cross sectional values in Figure 3.8, it can be seen that the inclusion is depicted as a peak in the elasticity value. The peak value is closer to what was measured with the VTIQ system and the manufacturer specifications. Since the expected wavelength in the phantom is close to the size of measured inclusion, the LFE algorithm is unable to correctly identify the boundaries of small inclusions. Both the 2D and 3D transducers had results that were higher than the manufacturer's specifications for both the soft and stiff lesions. Higher frequency excitation could be used, but as one increases the frequency, the wave penetration

and wave displacement amplitudes decrease to the point of being undetectable or unreliably measurable. It may also be possible that the phantom has changed over time and the manufacturer specifications are not longer truly valid.

The study of *ex vivo* tissue shows that the method is not constrained to only work within phantoms. The phasor images show that the waves are propagating well within the tissue and elastography images are consistent with the structure of the kidney. In some other studies of *in vivo* porcine kidneys using supersonic shear wave imaging, the measured elasticity ranged from 6.9 to 8.7 kPa [53].

This comparison indicates that the elastic properties of the kidney tissue could change significantly when taken out of the body and vary depending on the study and method in which they were collected. Future laboratory studies, described in Chapter 5, investigate how blood flow and blood pressure affect the wave propagation in *in-vivo* tissue. It is also possible that elasticity measured in the tissue is more frequency dependent, as described by Sinkus *et al.* [154] and thus the steady state shear wave measurement would result in a different elasticity than a transient shear wave as was used by Gennisson *et al.* [53].

The liver tissue scanned does show consistent elastic results with other liver studies. MRE liver studies report elastic properties ranging from 2 kPa to about 8 kPa, depending on the level of fibrosis [71, 72, 181]. Since the technique of measuring the elastic properties in MRE is similar to the method used in this paper, the comparison is fair. As with the *ex vivo* kidneys, the properties of the liver should be further studied in an *in vivo* environment.

One limitation of this approach, in comparison to the 3D motorized transducer, is the changes in surface pressure caused by the changes in transducer position during the acquisition of the 3D volume. The pressure of the transducer on the tissue can, in itself, cause changes in the measured stiffness due to pre-compression effects [19], and the changes in transducer position can cause changes in the wave pattern that is measured, which is assumed to be in steady-state.

3.6 Conclusion

In this chapter, we present an absolute elastography method for a tracked 2D ultrasound transducer using two different methods, both a clinical freehand method

and an automated method using the research da Vinci Robot interface. Absolute elastography methods provide quantitative information about the underlying tissue characteristics to the user. The system was implemented on the da Vinci in order to provide surgical guidance to the surgeon.

Chapter 4

Review of Elastography Measurements of Kidney

4.1 Introduction

Kidney transplant is the gold standard treatment for end stage renal disease. As the kidney function decreases, and the EGFR falls below 15 mL/min, kidney failure is diagnosed. The only treatments at this stage of kidney failure are dialysis or kidney transplantation. The leading causes of death for dialysis patients include cancer, cardiovascular disease, valvular disease and infections [170]. Transplant is the preferred method as the long term survival of the patient is greatly increased over those on dialysis [131].

Unfortunately, kidney transplants fail over time. As discussed in Section 1.2.3, chronic allograft dysfunction or CAD is the main reason for graft failure [57]. CAD is caused by the accumulation of IF/TA. Over time, the fibrosis and atrophy impair the kidney's ability to filter the blood plasma and regulate water levels and ion concentrations [150].

The progression of CAD often goes undetected as the EGFR may not fall below clinically relevant levels until after significant fibrosis build up [116]. Biopsies allow detection of histological changes that can be used to diagnose IF/TA. On the one hand, biopsy involves risk and pain for the patient and thus frequent biopsies are not recommended [149]. On the other hand, it has been reported that the av-

erage transplanted kidney loss from biopsy was approximately 0.03% whereas the loss from rejection was 5% [110]. It is possible that the losses of these transplants could have been prevented using the histological knowledge gained from a biopsy. Thus, it is important to have a non-invasive method to provide a quantifiable measurement of fibrosis. A non-invasive method could be used more often than biopsy and could provide a better monitoring protocol, providing more quantitative data over time.

Ultrasound elastography presents a non-invasive method for fibrosis detection that has been used successfully to diagnose the stages of fibrosis in the liver. Unfortunately, the extension from the liver to the kidney has proven to be difficult [25]. If the elastic properties of the tissue, as measured with ultrasound, could be consistently correlated with the histological changes within the kidney, it would be possible to better monitor the progression of IF/TA and make changes in a patient's treatment that would slow the progression and prolong the life of the allograft. This method of interrogation could be used for either transplant or native kidneys. There has been previous research on the topic of relating the measured elastic properties of the kidney with the clinical prognosis.

This chapter present an overview of current literature and will focus on the complications and difficulties of kidney elastography. It builds upon the review from Grenier *et al.*, which presents a comprehensive overview of the kidney elastography literature prior to 2013 [55]. The literature reviewed in this chapter uses a variety of elastography techniques that were described previously in Section 1.4, such as strain ratio, Acoustic Radiation Force Impulse (ARFI) (Siemens Medical) and SuperSonic Imagine, FibroScan, and MRE. Results for both native and transplant kidneys will be presented including literature addressing the difficulties of imaging the complicated anatomy of the kidney.

The papers presented were selected to provide a broad overview and illustrate the current state of the literature. This chapter will concentrate on the most current literature and the most important contributions, according to the author's judgment.

4.2 Type of Elastography Imaging

4.2.1 Strain Ratios

Strain imaging measures the compression of the kidney or section of the kidney in response to pressure applied to the tissue by the transducer. Most papers report a strain ratio, in which the strain of two areas is compared. In the case of the kidney, these two areas are often anatomical sections of the kidney, the cortex or medulla. In other papers, the compression of the cortex of the kidney is normalized by the compression of the entire kidney or across the entire image [48].

Using this normalization method, a study of 20 patients with either mild or moderate fibrosis found that the levels of fibrosis as defined in the Banff Score, could be distinguished [48]. Comparing the compression of the cortex of the kidney with that of the medulla, cortico-medullary strain was found to be useful in determining the level of IF/TA in a study of 45 patients [50]. Another method of strain ratio calculation is to use the strain ratio measured between the parenchyma and the central collecting system of the kidneys [76]. Kahn *et al.* looked at 112 patients, but only 19 had biopsy results. They found that there was some correlation with high grade of fibrosis (three patients). Ozkan *et al.* also measured the strain ratio using the parenchyma and central collecting system [125]. They found the method promising but the variability of this type of elasticity measurement was high enough to warrant further study.

Not directly looking at fibrosis, Menzilcioglu *et al.* compared the strain ratio with the measured resistive index (a measure of blood flow) of the kidney [111]. For measuring the strain ratio they measured the decompression of the tissue with the fat surrounding the kidney as a reference. They looked at 121 CAN patients and 40 healthy volunteers and found that the measured strain index was more sensitive in detecting CAN than the resistivity index.

All the papers mentioned above use semi-quantitative strain ratios, meaning that the numerical results cannot be compared across patients, making the results of these studies less applicable across large patient populations. Many of them use different tissues types to regularize their measurements. Doing so minimizes the user and pressure dependent effects that negatively impact strain imaging. Strain

and strain ratios do have an advantage in their simplicity. Acquisition and calculations are straightforward and simple and generally do not require specialized equipment. All the literature presented here found positive correlations between the strain ratios and kidney health indicators such as level of fibrosis or resistive index. However, strain and strain ratios are operator dependent and often show a high variability depending on the user [125].

Author	Year	Method	Number & type of patients	Results & Notes
Weitzel [178]	2004	Normal-ized strain	2 patients	Compared one normal patient with one patient with confirmed fibrosis
Ozkan [125]	2012	Strain ratio	42 transplant patients	Positive correlation with resistive index, but low repeatability
Gao [48]	2013	Strain	20 patients with biopsy	Compared developed and normalized strain to biopsy results
Kahn [76]	2013	Strain ratio	112 patients	Correlation only with high fibrosis patients
Gao [50]	2015	Strain ratio	45 patients	Used the strain ratio between cortex and medulla
Gao [49]	2015	Strain ratio	2 canine models	Measured the strain as a function of time after renal ligation
Menzil-cioglu [111]	2016	Strain ratio	121 CAN patients and 40 healthy volunteers	Found strain ratio more sensitive than resistive index in predicting CAN patients

Table 4.1: Existing studies using strain and strain ratios which are relevant to kidney fibrosis stiffness measurements.

4.2.2 ARFI and SuperSonic Imagine (SSI)

ARFI and SSI are quantitative stiffness measurements that use the acoustic power of the transducer to create a "push pulse" in the tissue and then use fast imaging techniques to track the speed of the resulting shear wave. Doherty *et al.* present a comprehensive review of elasticity imaging methods that use an acoustic radiation push pulse [40]. These methods have a high resolution, measuring the stiffness of a small section of tissue, about 1 cm by 1 cm. The kidney is a complicated organ and the likely area of interest is the outer cortex and medulla of the kidney, where the functioning nephrons are located and filtering takes place. It is advantageous in this setting to be able to measure specific area within the kidney.

ARFI and SSI are the most widely used methods to measure kidney stiffness, and as such, there are review papers that outline the results from these studies. Grenier *et al.* provides an overview of all renal elastography [55], while Zaffanello *et al.* specifically targets the use of ARFI in renal assessment [185, 186]. We will discuss the most pertinent specifics of these articles in the following sections.

These review papers noted the wide variation in reported results from renal allograft scans. Despite these variations, Zaffanello *et al.* point out that there is a consensus among the papers, that higher levels of fibrosis, or lower levels of renal function, lead to higher measured stiffness [186]. They noted the technical difficulties in creating repeatable and reliable measurements, citing many of the same factors discussed below, including transducer pressure, perfusion, anatomical structures and patient heterogeneity. They conclude that ARFI can be a useful technique in long term renal allograft assessment, but note that these are preliminary studies and further improvements and standardized guidelines are necessary. As mentioned in Chapter 1, one of the limitations of this type of imaging is the depth penetration, which limits its use for kidneys farther from the patient's skin.

4.2.3 FibroScan

FibroScan is a commercial product often used in liver imaging and fibrosis staging [25]. It has been proven to provide good correlation between its stiffness measurement and the level of fibrosis in the liver; a few studies report its application to measure the stiffness of kidneys. This type of elasticity imaging uses a mechan-

ical impulse to create a wave in the tissue and then measures the resulting shear wavefront speed with a single element transducer. Unfortunately, there is only a single image line to guide where the measurement is taking place. There are two depth settings available, but the resulting measurement is an average along the line of the single element transducer. The sample volume is fixed at 4cm long between 25mm and 65mm below the skin surface. Without a clear indication of where the measurement is taking place it is possible that the measurement is an average of fat, cortex and collecting system of the kidney, rather than just one specific area [55].

Despite some technical challenges of using the FibroScan system on the complicated anatomy of the kidney, researchers have looked at the correlation between the FibroScan results and kidney health and function.

The FibroScan system was used to measure the stiffness in renal transplants [8]. The stiffness of 55 patients was measured. The study found that there was a significant positive correlation between the percentage of fibrosis and the measured stiffness, reporting the average of 10 measurements. When comparing the stiffness of stable (EGFR $>$ 50ml/min) and impaired function (EGFR $<$ 50 mL/min) grafts, they report a value of 22.2 $\pm$ 11 and 37.1 $\pm$ 14.2 kPa respectively. Of the 55 patients measured with FibroScan, 20 had biopsies, and the rest were assumed to be stable grafts with $<$ 5% fibrosis. In these patients, the results were also compared to the Banff Score [155] and the different fibrosis levels could be differentiated (see Section 1.2.3 for more details of the Banff Scoring system) based on stiffness.

A study of 164 transplant patients also found positive correlations between kidney stiffness and advanced fibrosis [156]. The authors also looked at measurements from different parts of the kidney and found an average stiffness of 35.0 $\pm$ 19.9 and 33.2 $\pm$ 18.6 kPa in the pole and center of the kidney respectively. In patients with advanced fibrosis, the average values were 42.0 $\pm$ 17.0 and 42.8 $\pm$ 15.7 kPa in these two areas of the kidneys. They also looked and found inter- and intra-observer variation to be less than 4 kPa. It should be noted that the standard deviations of the reported values is large in comparison to the values reported, where the standard deviation is often half of the reported value. To overcome some of the technical challenges, Sommerer *et al.* use software available from Echosans to reassess the elastograms from the device in order to adjust the angle, depth and

length of the shear wave to limit the area of interest to the kidney cortex. Without this reassessment, they experienced high rates of measurement failure.

Nakao *et al.* and Lukenda *et al.* also presented similar results [103, 115]. They both found that the FibroScan measurements showed a positive significant correlations between the measured stiffness and the level of fibrosis and were related to the EGFR. Of interest, Nakao *et al.* reported that patients with high grade of interstitial fibrosis (Banff grade 2) had a mean value of 53.87 ± 17.8 kPa which is the highest reported stiffness for advanced fibrosis. Lukenka *et al.* report a mean stiffness of 32.2 ± 5.6 kPa which is close to average, 37 kPa across the studies presented here. Similar to Ardnt *et al.*, they found no correlation with the resistivity index of the patients [8], where resistive index is a quantification of blood flow into the kidney.

Across all the studies presented here, the average Young's modulus for healthy kidneys was approximately 28 kPa, and 37.5 kPa for those with impaired function. But the values that are given in each of the studies overlap, with normal ranging from a possible 11 to 50 kPa and impaired ranging from 28 to 63 kPa. Although easy to use, the complications due to averaging along the line of measurement and the lack of detailed imaging feedback mean that it is very difficult to provide consistent and reliable results for the kidney. The results from the FibroScan system are also higher compared to those of the ARFI and SSI systems, which are generally in the 10 to 20 kPa range.

Author	Year	Young's Modulus (GFR $>$ 50 mL/min vs GFR $<$ 50 mL/min)	Correlation with Kidney Health	Number & type of patients	Notes
Ardnt [8]	2010	22.2 ± 11 vs 37.1 ± 14.2	yes	55 patients, 20 with biopsy	Good correlation with eGFR cutoffs
Sommerer [156]	2012	32.7 ± 18.7 vs 43.1 ± 20.8	not definitive	117 patients	Correlation with Banff score, variations of 3 kPa over 3 months, correlation with increased creatine levels
Lukenda [103]	2014	28 ± 2.7 vs 33.9 ± 5.5	yes	52 patients	Correlation with eGFR and with Banff Scoring
Nakao [115]	2014	25 ± 5.5 vs 37.6 ± 4.2	yes	35 patients, 27 with biopsy	Positive correlation with increasing fibrosis

Table 4.2: Existing studies using FibroScan relevant to kidney fibrosis stiffness measurements.

4.2.4 MRE

Although this chapter has focused on the use of ultrasound for imaging kidneys, other papers using magnetic resonance imaging have also looked at kidney tissue characteristics.

When using MRE, a separate excitation source is placed on the patient's skin and steady state waves are transmitted through the patient's abdomen. MRI can then image the wave propagation in three dimensions and inversion algorithms are used to recover the elastic properties of the tissue [106]. This method of elastography is similar to SWAVE, described in Section 1.4 and used throughout this thesis. It is important to note that SWAVE and MRE measure the wave speed of steady state waves, which may have different properties than the transient waves measured by the imaging methods above. All results should also be reported with the excitation frequency when possible since there are some frequency dependent variables that affect the measured shear modulus. In addition, all the results presented here are of native kidneys (either human or swine), rather than transplanted kidneys.

Kruse *et al.* reported early results on the feasibility of using MRI to collect elastography data of healthy native kidneys and found that the average shear stiffness was 16 ± 5 kPa [87]. Other papers focused on the reliability and reproducibility of the method. Low *et al.* imaged 16 healthy volunteers at excitation frequencies of 90 and 60 Hz [102]. They scanned each patient twice in a 30 minute interval and found that it was a reliable technique with an average renal stiffness of approximately 3.5 kPa at 60 Hz and 5.7 kPa at 90 Hz.

Rouviere *et al.* looked at 10 healthy patients and attempted to measure the stiffness in the different sections of the kidney at 45 and 76 Hz [139]. They were able to measure the stiffness in the parenchyma (4.9 ± 0.5 kPa and 9.4 ± 0.8 kPa). It should be noted that at these excitation frequencies, the wavelength in the kidney is 50 mm at 45 Hz and 40 mm at 76 Hz which might be a limiting factor in this type of imaging, because the size of the parenchyma is about the same as a wavelength, so observing a full wavelength within the parenchyma may be impossible. Similar to this study, Bensamoun *et al.* also looked at healthy kidneys in order to assess the normal kidney value [20]. When measuring at 60 Hz, they reported an average shear modulus of 4.1 ± 0.2 kPa.

Other MRE papers looked at the influence of renal stenosis on the measured stiffness of swine kidneys. Korsmo *et al.* found that the Young's modulus (E) of the medulla changed (10.7 ± 0.2 kPa to 12.7 ± 0.4 kPa) while the cortical stiffness was unaffected after 10 weeks of induced stenosis [85]. In histological studies, the two kidney areas showed similar fibrotic levels. Warner *et al.* looked at the results from acute graded stenosis [177]. They found a decrease in the stiffness during acute stenosis, which they attributed to decrease in renal blood flow.

The MRE papers were more focused in establishing the baseline results for this method of kidney imaging and determining an appropriate protocol. It is a bit more difficult to compare these studies, as the excitation frequency should be taken into account, but, of the studies looking at normal healthy patients, the reported shear modulus fell around 3 to 8 kPa, with one paper reporting much lower results near to 1-2 kPa.

All the papers that looked at the results from artificial stenosis of a swine kidney reported that the contralateral kidney (the one without the artificial stenosis) measured stiffer than the one with compromised blood flow. In the longer term studies, the stenosed kidney also became stiff as it developed fibrosis.

It is interesting to note the excitation frequencies used in these papers, ranging from 45 Hz to 120 Hz (with one instance of 150 Hz). These are similar frequencies to those used during liver imaging, which generally is a more homogenous organ with a lower stiffness (4 kPa for healthy subjects) [10]. At 80 Hz, and a shear modulus of 5 kPa, the expected wavelength within the kidney is about 2.7 cm, where the entire length of the kidney is about 7 cm. This means that the resolution of the MRE is low compared to the size of the kidney and may not be able to resolve the stiffness within the anatomical structures of the kidney.

Author	Year	Frequency (Hz)	Shear Modulus (μ (kPa))	Results	Number & Type of patients
Yin [182]	2009	90	Control: 5.1 ± 0.6 Contralateral kidney: 4 ± 0.2	Shear stiffness of the contralateral kidney increased compared to one with artificial stenosis	Swine models: 5 with stenosis and 4 normal
Yin [183]	2010	90	3-5	Increased stiffness with increased pressure, decreasing stiffness with decreasing flow	4 swine models
Bensamoun [20]	2011	60	4.2 ± 0.2	Established protocol for kidney imaging, determine normal values	11 healthy subjects
Rouvier [139]	2011	45 and 76	4.9 @ 45 Hz, 9.5 @ 76 Hz	Average variability of 6% within the same subject	10 healthy patients
Warner [177]	2011	120	With stenosis: 4.8 ± 0.6 Normal: 7.6 ± 0.3	Decreases in renal blood flow leads to decreased stiffness. Chronic decrease could offset increase from fibrosis	6 swine models with graded ischemia
Lee [97]	2012	90, 120 and 150	Normal: 7.9 With Fibrosis: 9.2 kPa @ 120 Hz	Increased stiffness with increasing frequency and increasing fibrosis	11 patients with biopsy
Korsmo [85]	2013	120	Normal: 10.7 ± 0.2 With Fibrosis: $12.7 \pm .4$	Correlation with fibrosis only within the medulla of the kidney	17 swine models
Streitberger [160]	2013	30-60	Medulla: 2.67 Cortex: 1.64 Hilum: 1.17	Bladder pressure seemingly irrelevant	9 healthy volunteers
Low [102]	2014	90 and 60	3.5 @ 60 Hz, 6 @ 90 Hz	6 kPa and 3.5 kPa	16 healthy subjects

Table 4.3: Existing MRE studies relevant to kidney fibrosis stiffness measurements.

4.3 Challenges of Kidney Imaging

4.3.1 Patient Heterogeneity

The liver has shown promising results when comparing the level of fibrosis to the results of elastic imaging [25]. Unlike the liver, the kidney is less homogeneous, with a complicated structure that may influence wave propagation. In addition to the structure, the kidney also experiences a wide variety in pressures from the renal artery and possible pressure for the ureter that may affect the elastic measurements. Other factors that may influence the measurements could include age, gender, arteriosclerosis, transducer pressure, frequency of excitation and when looking at *ex-vivo* specimens, storage conditions.

Bota *et al.* looked at general factors that influence the shear wave speed in 91 healthy volunteers [26]. Looking at Body Mass Index (BMI), kidney length, renal parenchyma thickness, age and gender, they found that age and gender were correlated to the elasticity measurements and also found some influence from the measurement depth. These types of factors should be factored in when measuring elasticity under other conditions.

4.3.2 Kidney Structure

The structure of the kidney has been shown to influence the speed of the waves. The nephrons in the cortex and medulla are aligned in such a way that tubes all run radially from the center collecting system towards the surface of the kidney in a fan shape. This means that when an ARFI transducer, for example, is placed facing the center of the kidney, the push pulse is travelling down the tubes of the nephron and the shear waves will be moving across the alignment of the loops of the nephrons. Alternatively, when the transducer is placed near the pole and imaging towards the opposite pole through the cortex, the push pulse will be aligned across the tubes of the nephron.

In particular, Gennisson *et al.* measured the shear wave speed in different orientations [53]. They found that elasticity values were higher when the ultrasound image and the push pulse was aligned perpendicular to the main pyramid axis. This means that the measured wave were traveling fast (higher elasticity) along

the nephron tubes than against them. The orientation dependency is not something that is not well standardized in kidney elastography. In general, most of the papers using ARFI and SSI align the ultrasound image parallel to the renal pyramids. However, it is not easy to be consistent in imaging the transplanted kidney since the kidney is not always in the same position with respect to the patient's skin.

4.3.3 Perfusion

Approximately 25% of the cardiac output flows through the kidney with each heartbeat, which creates large changes in the input blood pressure. The kidney has two autoregulation mechanisms to create constant filtering pressure inside the kidney, such that the changes in blood pressure do not affect the functionality of the kidney [82]. The first mechanism is the myogenic mechanism, which is the intrinsic property of the smooth muscle. When the pressure rises suddenly the muscle of the renal afferent arteriole is stretched and contracts to compensate. This mechanism smoothens out the changes due to the heart cycle. The second mechanism compensates for larger changes in the general systemic pressure. The tubule-glomerular feedback uses the NaCl concentration to release vasoconstriction that affects the afferent arteriole [82]. The vasoconstriction also causes the vessels within the kidney to constrict, causing the apparent input pressure to increase.

It has been hypothesized that the blood pressure could affect the elastography measurements. In particular, researchers have looked at two areas, stenosis [49, 53, 85, 177, 182], where the renal artery or vein are blocked and perfusion, where the increase in blood pressure could affect the measurements [9, 61, 183].

Of the papers looking at stenosis, Warner *et al.* noted that the stiffness decreased with increasing stenosis (and decreasing blood flow) [177]. Gennisson *et al.* also found that decreasing the blood flow through the renal artery decreased the measured stiffness and that ligating the renal vein (increasing the internal pressure) increased the measured stiffness [53].

Korsmo *et al.* looked at the fibrosis caused 10 weeks after the induced stenosis [85]. They found that the stenosis increased the fibrosis in the medulla of the kidney, with no change in the cortex. Yin *et al.* also looked at the kidney stiffness 10 weeks after induced stenosis, but instead of looking at the kidney with stenosis,

they measured the stiffness of the contralateral kidney [182]. It was suggested that the contralateral kidney increases blood flow to make up for the stenosis of the original kidney. The authors found that the measured stiffness in the contralateral kidney was increased. In a different study, Yin *et al.* decreased the blood flow to the kidney and this time measured the shear stiffness in both the stenotic and contralateral kidney [183]. This study found that with increasing stenosis, the stenotic kidney decreased in stiffness and the contralateral kidney increased slightly.

Only a few papers look at the effects of perfusion directly as it is difficult to measure and control. Asano *et al.* measured the ankle pulse velocity as a surrogate for blood flow in the kidney [9]. The ankle pulse velocity, the velocity of the blood flow through the artery near the patient's ankle, would indicate the level of sclerosis. They found that with decreasing shear wave velocity, there was a decrease in EGFR, but surmised that the changes in shear wave velocity were caused more by the change in blood flow than by changes in fibrosis.

The connection between chronic kidney disease (and the development of fibrosis) and arterial stiffness (and cardiovascular disease) is described by Garnier *et al.* [51]. In that paper, the authors point out that patients with compromised renal function (with and without hypertension) have much higher incidences of arterial stiffness. Cardiovascular death is 10-30 times higher in patients with end-stage renal disease than in the general population. This association persists even after adjustments for traditional cardiovascular risk factors. In light of this connection, it is possible that the differences in ankle wave velocity that Asano *et al.* saw could have been part of this association [9].

Using *ex-vivo* kidneys, it is possible to control the arterial input pressures from 60 to 120 mmHg, and 60 mmHg in the ureter [61]. In that study, porcine kidneys ($n = 11$) were harvested and examined four hours after death. They found that with increasing the pressure, the measured shear wave velocity also increased. This the only study found that looks specifically at *ex-vivo* kidneys in a controlled environment.

4.3.4 Transducer Pressure

Strain ratio is used to measure the changes in kidney structure and function, and measuring strain involves putting pressure on the kidney and measuring its response. Thus, it would not be surprising that transducer pressure on the kidney would influence the measurements of other elastography measurement methods. Syversveen *et al.* looked at the relationship between ARFI measurements and transducer pressure [163]. In patients with varying degrees of fibrosis, they found correlation only between pressure and shear wave velocity, but no correlation between the shear wave velocity and the degree of fibrosis. The transducer pressure would be especially important for transplant kidneys, which do not have the protection of the ribs from outside pressures. No subsequent papers have attempted to standardize the transducer pressure, so this is an unknown variable in all the papers.

4.3.5 Viscous Properties of Tissue

Most elasticity measurement systems assume that the tissue is entirely elastic, even though tissue can have significant viscous properties as well. Two methods, Shearwave Dispersion Ultrasound Vibrometry (SDUV) and Viscoelastic Response (VISR) have begun to measure the viscous properties of different tissue types [6, 7, 66, 151, 172]. The studies involving kidney tissue, though, are very limited. The viscous properties of the kidney could also be contributing to the differences in results, as the viscous components are dependent on the excitation frequency, which is not controlled in all measurement methods.

Other models of tissue including poroelasticity, could be used to characterize the tissue properties not explained with a linear elastic model. A poroelastic model describes the tissue as a material with an elastic skeleton saturated with fluid. This fluid is allowed to flow freely through the pores of the matrix. This type of model has not been extensively applied to kidney tissue but has been used to characterize other tissue types [45, 128].

4.3.6 Incongruent Results

The majority of papers have reported that increasing fibrosis results in increasing measurements of stiffness. There have been a few notable exceptions. One of the

first papers to use ARFI to look at the correlation between fibrosis and shear wave velocity found there was no significant correlation [162], disagreeing with the first positive correlation found with FibroScan [8].

In a paper looking at 43 patients, Grenier *et al.* found that the stiffness measurements correspond only to the sum of all the Banff Scores for a given biopsy, but not with any particular value [54]. They also reported very high interobserver viability which might account for the lack in correlation. The measured stiffness was also notably higher than other reported values using supersonic shear wave imaging, with a mean stiffness of 22 kPa in the cortex and 16 kPa in the medulla.

Using ARFI to measure only the cortex, Wang *et al.* determined from their data that there was no correlation between the shear wave velocity and the level of renal fibrosis [176]. They did find, though, that the resistivity index was higher in the later stages of chronic kidney disease.

Contradicting most other published papers, Hu *et al.* found that ARFI measurements of impaired kidneys showed the shear wave velocity in the kidneys decreased with increasing kidney impairment [67]. This means that as the kidneys failed functionally, the kidneys became softer instead of harder. They also noticed that the parenchymal thickness decreases as the function decreases.

As both of these studies took place in China, it is possible that differences in the causes of kidney failure in this region account for the differences in results. In North America, the main causes are hypertension and diabetes, whereas the main cause of kidney failure in China is glomerulonephritis [51].

4.4 Conclusions

Elastography has the potential to provide vital information about the health of the transplant and native kidneys. This information could potentially change the method of treatment and prolong the life of a transplant.

The results of the previous research of kidney elasticity have been mixed and variable. Different elastography methods have produced different results, especially considering the absolute measurement results. With ranges from 2 kPa to 50 kPa, this shows that results across methods cannot be compared reliably. The intra- and inter-observer coefficient of variation was found to be 20% and 12%

respectively [54] and another paper found the coefficient of variation on repeated measurements to be between 8% and 15% depending on the region within the kidney [58]. The results from the native kidney studies and the transplant kidney studies may also not be directly comparable. The transplantation process and immunosuppressant drugs may affect the measurements of the kidney in a way that is of yet ill defined, complicating the comparison of MRE results (mostly native kidneys) to the ultrasound results in transplant patients.

Many of the authors point out the confounding factors in making measurements of the kidney. Sommerer *et al.* identified confounding factors with FibroScan including scanning depth, BMI, fluid accumulation and kidney structure in general. They also provided an outline for acceptable criteria for valid measurements [156].

Due to the inconsistency of the measurements, it is important to better understand how confounding factors directly affect the measurement results and how they might be addressed in the future. The confounding factors to be addressed are perfusion and how the kidney anatomy affects wave travel.

It is important to look at perfusion and anatomy in an environment where most of the possible variables can be controlled, such as an *ex-vivo* setting. Even in an *ex-vivo* setting, factors such as storage temperature could potentially have an effect on the ARFI measurements [168]. Fortunately, it was found that storing the kidneys at either +4 degrees Celsius or at 20 degrees Celsius did not significantly change the elasticity measurements from when the kidneys were measured fresh. So using *ex-vivo* kidneys stored overnight should be representative of fresh kidneys. Some initial results for changes in pressure were reported, but only looked at static pressure rather than pressure with flow, which is more representative of kidneys *in-vivo* [61].

In the following chapters, we examine the relationships between the input renal pressure and elasticity measurements using steady state shear wave elastography. We also examine the wave pattern within the kidney and how the anatomy of the kidney affects the waves. It is often assumed in elastography measurements that the tissue is entirely elastic, without viscous components. In the next chapter we will also determine the viscous properties of the kidney tissue, as these can be a confounding factor when measuring at different frequencies or with different types of acoustic pulses.

Although most of the measurements are taken in the context of native and transplant kidneys imaged trans-abdominally, all the results of the experiments described in the following chapters can be and will be applied to intra-operative ultrasound elastography. All the renal tissue characteristics should be similar, and changes in these characteristics could increase differentiation between healthy and cancerous tissue.

Chapter 5

Tissue Characteristics of Porcine Kidney *ex-vivo*

5.1 Introduction

As described in Chapter 4 it is imperative to better understand the parameters of kidney elasticity imaging. In many elastography algorithms, assumptions are made including that the tissue is completely elastic, and that the tissue is homogeneous (Chapter 1.4). In this chapter, we look specifically at two poorly understood aspects of the kidney imaging. The first aspect examined is the effect of input pressure on the kidney elasticity measurements. In particular, how the elasticity of the changes with pressure throughout the heart cycle and possible long term changes with hypertension. The effect of heart beat is poorly controlled during imaging *in-vivo* and has been shown to influence the results as discussed in Chapter 4. The second aspect that was examined is the presence of a viscous component of the kidney tissue. The viscous effects are generally not taken into account during traditional elasticity imaging, but could affect the results and cause the differences between different methods of elasticity imaging.

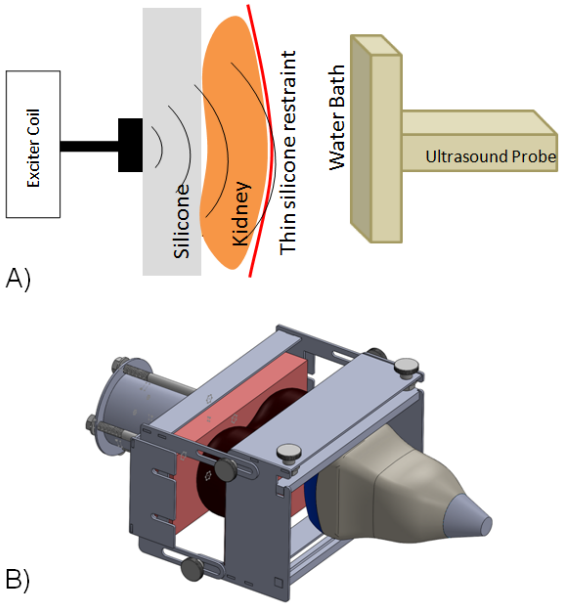

Figure 5.1: A) A diagram of the shaker set-up. B) The Solidworks rendering of the set-up, showing the frame, ultrasound transducer and the kidney.

5.2 Imaging Set-up

In order to image the kidney in a controlled environment *ex-vivo*, a stainless steel apparatus was designed to hold the ultrasound transducer, the exciter coil and the kidney.

In order to best allow vibrations to propagate through the kidney, the kidney should be allowed to move freely at the boundaries. To allow this, the kidney is held away from the ultrasound transducer with a flexible silicone sheet. The sheet is stretched on the frame, supporting the kidney and holding it in place during scanning.

On the other side of the kidney, the exciter coil and the kidney are separated by a stand off pad of silicone. This pad is approximately 2cm thick and serves to transfer the vibrations from the exciter coil into the kidney with minimal loses. This also means that the waves arrive at the kidney surface across a wider area, rather than from a point source, or small disk, as some of our previous work has

A much abridged version of this chapter was previously published [145, 146]

used [3, 14, 113].

The frame is adjustable to deal with the different sizes of kidneys, and the fact that the kidney expands as the pressure increases during some parts of the testing. It is important to maintain constant pressure on the kidney, as pressure can affect the elasticity measurement [163].

The kidneys were scanned using a multi frequency steady-state wave imaging technique and using external excitation and a 3D motorized ultrasound transducer (Ultrasonix 4DL14, Analogic, Richmond, BC, Canada) [2, 14]. Each volume was created from 25 image planes, each placed approximately 0.5mm apart. Elasticity of the volume was calculated using LFE [105] and/or Finite Element Model (FEM) [64].

5.3 Kidney Harvest

All the kidneys used in this thesis were harvested from pigs used in research and training studies that left the kidneys intact. These pigs were all female pigs and weighed approximately 50 kilograms. Within moments of euthanasia, the kidneys were harvested in a similar manner to kidneys harvested for donor nephrectomy. The kidney is identified within the abdomen and the tissue surrounding the kidney is removed. The vessels entering and exiting the kidney are then identified and isolated from the surrounding tissue and fat. The length of the vessel, from the kidney to the aorta and vena cava was isolated and the vessels are clamped and cut close to these major vessels. Particular care was taken to harvest as much of the renal vessels as possible, as these will be used later in the study. Unlike those kidneys used for transplant, for this study, the ureter was not needed.

After harvest, the kidneys were flushed with graft preservation solution, until the solution coming from the renal vein flowed clear. A 16 or 18 gauge cannula was placed into the renal artery, and tied in place with suture ties. The fluid was pushed into the kidney with a syringe, and then a slow pump was used to continuously push fluid for several minutes.

Both water and saline have been previously used to perfuse the kidney, but in our experience, these fluids would not flush out of the vein.

The kidneys were then stored in solution at +4 $^{\circ}$C until imaged, no more than

12 hours after harvest. Storage in these conditions should not have caused changes to the elastic properties of the kidney [168].

5.4 Kidney Pressure Tests

5.4.1 Infusion Pump

To change the pressure into the kidney, and to flush the kidney slowly, a peristaltic pump was used (Fisher Scientific, part number 13-876-3). The pump has several sizes of tubing and variable speeds that allow changes in the flow rate of the pump. A constant tubing size was used for all the kidneys for consistency. To measure the pressure on the renal side of the kidney, a pressure gauge (Kodiak Controls KC25-3# Low Pressure Gauge, 5 PSI) was attached to the tubing between the pump and the kidney. The renal vein was left open and pressure on that side was assumed to be zero. Since within a live subject, the renal vein would be connected directly to the vena cava, which has a pressure of about 1 mmHg, we considered the difference between our set-up and the correct anatomic pressure to be negligible in comparison to the pressure on the input side, which was between 60 and 130 mmHg.

Figure 5.2 shows the general set-up of the kidney, pressure gauge and the pump. The three components are connected through silicone tubing.

For this series of tests, 5 kidneys were harvested and measured.

We measured the elasticity of each kidney at three gauge pressures: zero (0 mmHg), simulated diastolic (60-80 mmHg) and simulated systolic (125 mmHg) to correspond with average diastolic and systolic pressures [15, 35].

Each kidney was measured at multiple excitation frequencies ranging from 50Hz to 175Hz. As there is an intrinsic viscous component of the kidney biomechanics, causing the apparent elasticity to increase with increasing excitation frequency, a linear estimation of the relationship between measured elasticity and frequency was made and the estimated elasticity at 125Hz is presented here.

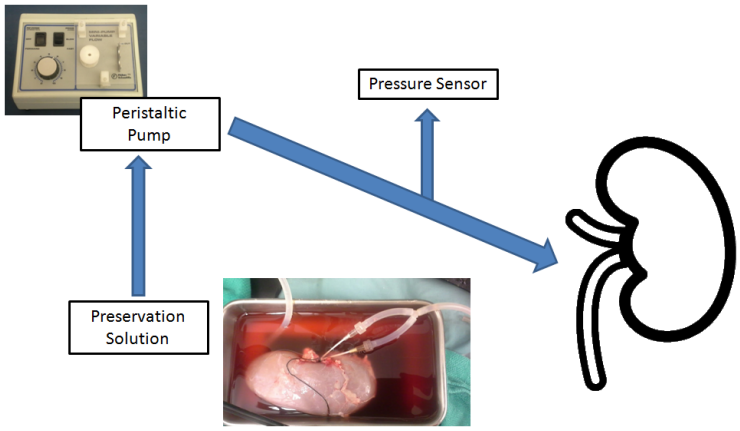

Figure 5.2: The pump and flushing set-up. The preservation solution is pumped into the kidney through a cannula which is inserted into the renal artery. A pressure gauge is in the system to measure the input pressure into the kidney.

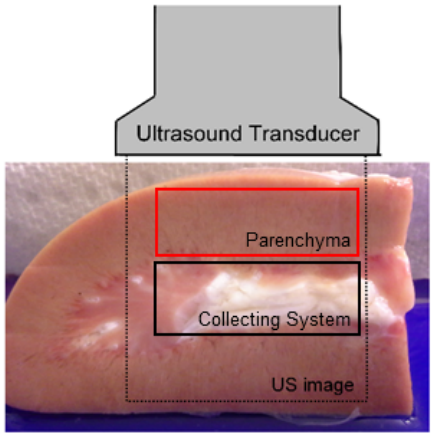

Figure 5.3: A diagram that shows the cross section of the kidney that is imaged during these experiments.

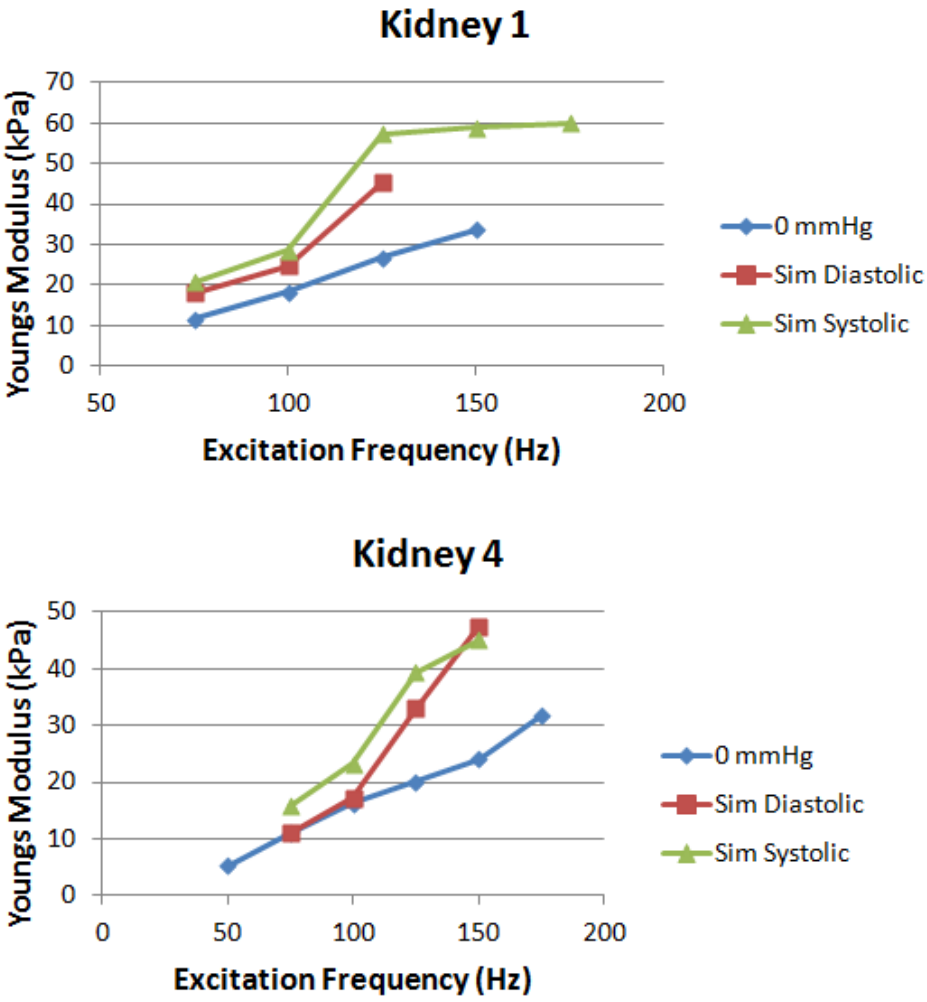

Figure 5.4: The relationship between measured elasticity and excitation frequency for three different input renal pressures. Connecting lines are used for visualization purposes only.

5.4.2 Kidney Pressure Results

In the examination of the 5 porcine kidneys, it was found that the measured elasticity of the kidney was dependent on the input pressure of the pump. Increasing the input pressure resulted in an increase in the measured elasticity, increasing from an average of 21 $\pm$ 3 kPa at zero mmHg to 34.1 $\pm$ 7 kPa at simulated diastolic to approximately 34.4 $\pm$ 9 kPa at simulated systolic pressure (130 mmHg). When comparing the results in a paired t-test, there was a statistically significant difference between the results of the 0 mmHg and simulated systolic ($p \leq 0.05$) and between the 0 mmHg and simulated diastolic ($p \leq 0.05$) but the $p-value$ between the simulated diastolic and the simulated systolic was 0.8. Although only using five kidneys in this experiment, we believe that the effect would be notable in all kidneys.

Figure 5.4 shows the results at different input pressures for each of the different excitation frequencies (Figure 5.5). It can be seen that the measured elasticity increases as the pressure increases at all excitation frequencies. This frequency dependence is further investigated in later sections of this chapter.

When looking at the resulting elastograms, the differences in the different areas of the kidney become visible (Figure 5.6). The upper section of the B-mode image is the parenchyma of the kidney, while in the center of the image is the collecting system. In the elastograms, it is possible to distinguish these two distinct anatomical structures. The collecting system shows up as soft in the elastogram, as it is mostly made of fluid. Similar to the results seen in vessels, fluid filled areas do not represent the true stiffness of the area [144]. The shear waves propagate in the soft tissue matrix and fluid of the collecting system, and appear much shorter than in normal renal tissue.

5.5 Viscous Properties of Kidney Tissue

In most elasticity measurements, there is an assumption that the tissue behaviour can be modeled solely by using a linear elastic model in which the shear modulus is assumed to only have a storage component. In reality, tissue has both elastic and viscous properties due to the physical construction of the cells and intercellular matrix. These viscous properties become more apparent when measuring at differ-

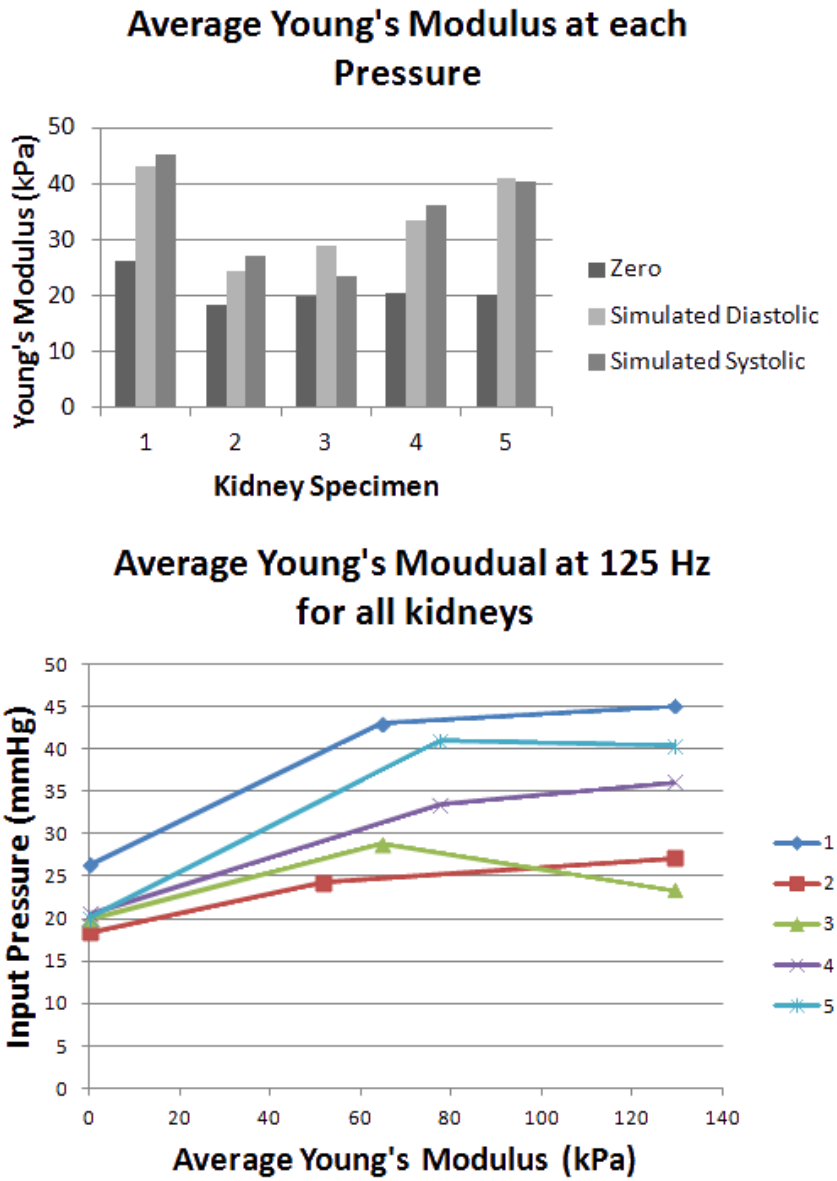

Figure 5.5: Top: a histogram of the average elasticity for each specimen. The average elasticity is measured at three different input pressures, zero, simulated diastolic and simulated systolic. Bottom: The elasticity, estimated at 125Hz, for all the kidney specimens at each of their measured input pressures.

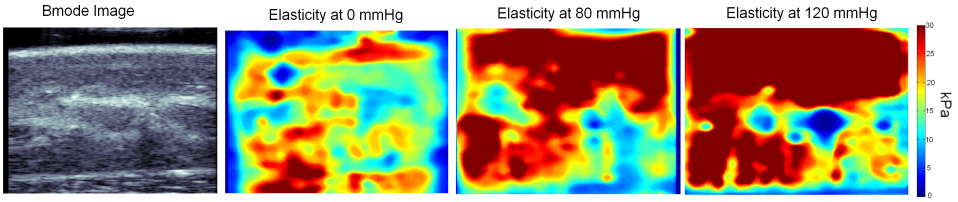

Figure 5.6: Cross-sectional images of the B-mode image of the kidney and the resulting elastograms at each input pressure.

ent excitation frequencies, since the tissue will respond differently when vibrated at higher *vs* lower frequency.

As the literature and different methods of measuring elasticity use various excitation frequencies, it is very important to understand how the tissue responds to these changes when trying to compare results across methods and studies.

Two methods to measure tissue viscous properties have recently emerged. They are SDUV and VISR. SDUV uses a single element "push transducer" and a "detect transducer" [7, 172]. The detect transducer measures the phase of the wave, produced by the push transducer, at two different locations along its path of travel. At two known locations the wave speed can be estimated for the phase velocity. The push transducer can push a different frequencies to measure the dependency of the shearwave speed on frequency. The measured wave speed at each frequency, ranging from 50Hz to 500Hz, is then fit to a mechanical model to solve for the elastic and viscous properties of the tissue. This method has been applied to an *ex-vivo* swine kidney [6, 7].

VISR imaging also leverages the Voigt model for tissue (described in detail below) [66, 151]. This method employs two acoustic radiation force push pulses at a single location within the tissue. The relaxation times for the tissue are measured and fit to the Voigt Model [151] or to a mass, spring, damper tissue model [66]. This method then reports τ, the estimate of the ratio of the viscosity coefficient to the relaxed elastic modulus. VISR is able to estimate the tissue properties in a very localized manner without reliance on shearwave propagation, so it is less affected by local changes in the tissue.

In a study of transplanted kidneys *in-vivo* using VISR, τ, the relative elasticity and relative viscosity were measured [66]. The relaxation time and these rela-

tive measurements were taken from multiple anatomical areas within the kidney. Using different combinations of these ratios, for different anatomical locations, the authors found that this method could differentiate patients with different diagnoses. Unfortunately, the results of this method are difficult to compare to other methods since the resulting measurements (ie. τ) are different than those reported by other systems (ie. Young's Modulus or shear wave velocity).

These two methods both use a model fitting approach to estimate the tissue properties, similar to what is described in this chapter.

5.5.1 Methods

Using a similar imaging set-up to that used during the pressure tests, all kidneys used for this portion of the study were imaged without flow, in the same imaging apparatus.

The kidneys were all flushed with preservation solution after harvest to remove any blood within the organ, as the clotted blood could change the measurements.

The kidneys are imaged in the stainless steel apparatus at six different frequencies: from 50 Hz to 225 Hz at intervals of 25 Hz. For each volume, 25 slices are imaged at a spacing of 0.5 mm. The 4DL14 ultrasound transducer was used, imaging at a depth of 4 cm.

5.5.2 Tissue Models

The mechanical models for tissue include the Voigt, b) Maxwell and c) Zener rheological models. These include both the elastic (μ (Pa)) and viscous (η (Pa s)) elements.

These models are simple representation of the tissue models. Real tissue is made up of cells, connective fibers, and intra- and extracellular matrix. Each of these components has its own elastic and viscous properties. The models presented here act as an aggregation of this very complicated system. Using these models we hope to gain insight into how much influence the viscous components have on the measured elasticity.

The Voigt model represents the two components placed in parallel, whereas the Maxwell model has these components in series. The Zener model combines

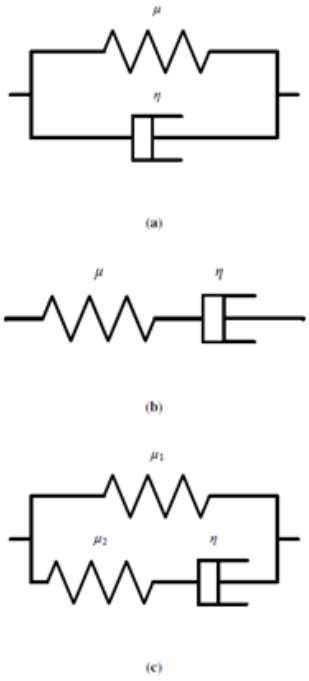

Figure 5.7: There are three rheological models used in these studies. a) Voigt, b) Maxwell and c) Zener. The springs represent the elastic components and the dash-pots represent the viscous components.

these two ideas into a single model. The derivation of these models can be found in detail In Jeffrey Abeysekera's thesis [3].

For each model the wave speed (c_s) as a function of frequency (ω) is calculated as follows:

Voigt:

$$c_s = \sqrt{\frac{2(\mu^2 + \omega^2\eta^2)}{\rho(\mu + \sqrt{\mu^2 + \omega^2\eta^2})}} \tag{5.1}$$

Maxwell:

$$c_s = \sqrt{\frac{2\mu}{\rho(1 + \sqrt{1 + \frac{\mu^2}{\omega^2\eta^2}})}} \tag{5.2}$$

And Zener:

$$c_s = \sqrt{\frac{2(\mu_1^2\mu_2^2 + \omega^2\eta^2(\mu_1+\mu_2)^2)}{\rho(\mu_1\mu_2^2 + \omega^2\eta^2(\mu_1+\mu_2) + \sqrt{(\mu_1^2\mu_2^2 + \omega^2\eta^2(\mu_1+\mu_2)^2)(\mu_2^2+\omega^2\eta^2)})}} \tag{5.3}$$

For each of these models, the model parameters (X) representing the elastic and viscous properties were optimized using the following, where ω_i is the excitation frequency in radians.

$$\underset{x}{\text{minimize}} \sum_{i=1}^{6} (c_s(\omega_i, X) - \hat{c_s}(\omega_i))^2 \tag{5.4}$$

And the error, ξ is defined as follows:

$$\xi = \sqrt{\frac{1}{6}\sum_{i=1}^{6} (c_s(\omega_i, X) - \hat{c_s}(\omega_i))^2} \tag{5.5}$$

Eleven experiments were performed. Each experiment represents a different kidney. All the elasticity results here were analyzed using thin volume 3D LFE techniques [14, 113] and with FEM methods [63].

The results of the these tests were fit to each different model using the Matlab Optimization Toolkit.

5.5.3 Viscosity Results

The quality of the model fits to the observed data can be seen in the following figure. And the results of the variable fitting are shown in Table 5.1 and Table 5.3 below. Individual graphs of each kidney used in this study can be found in Section A.2.

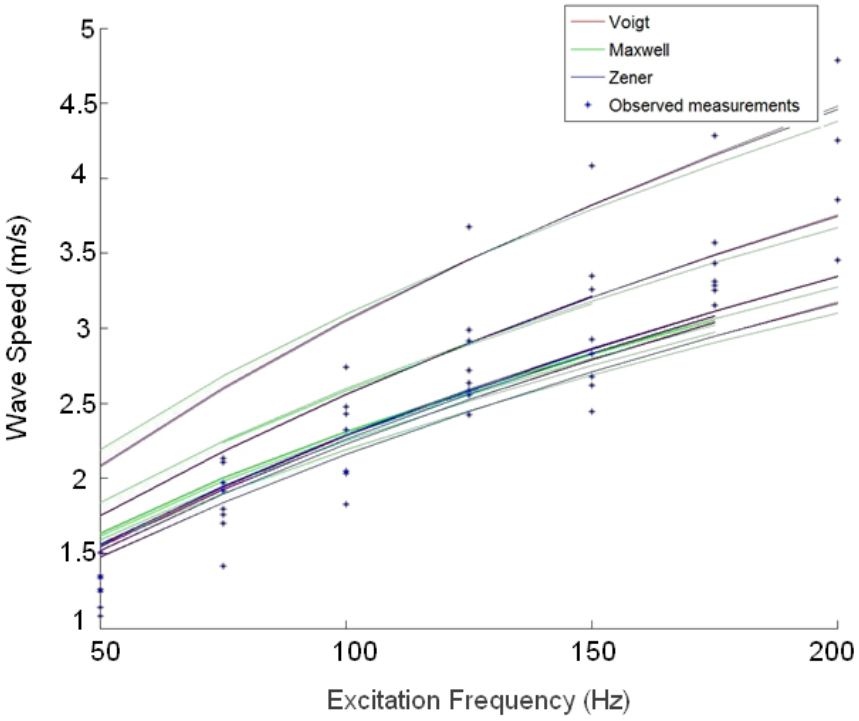

Figure 5.8: The graphic results of the LFE model fitting for all the experiments. The stars represent the experimental data, the red, blue and green lines represent the results of the Voigt, Maxwell and Zener Models respectively.

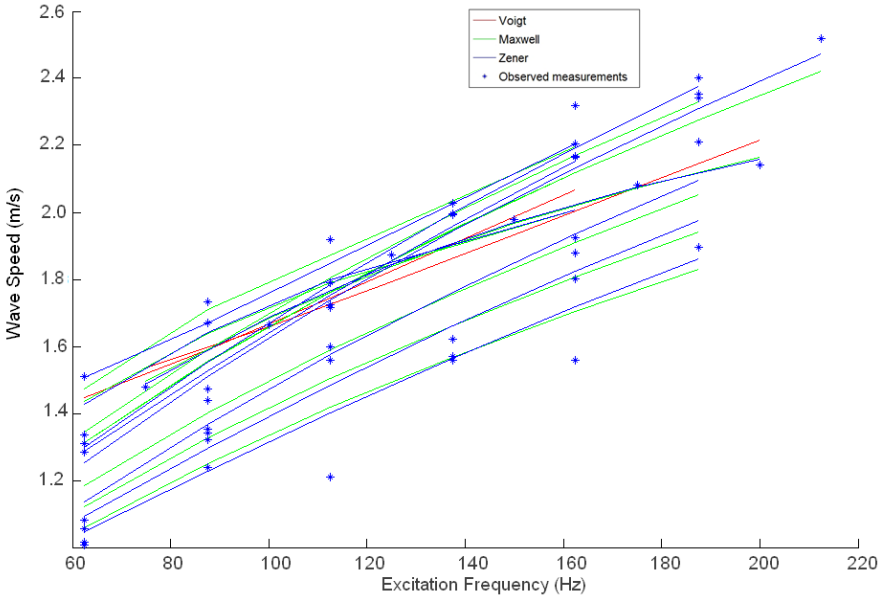

Figure 5.9: The graphic results of the FEM model fitting for all the experiments. The stars represent the experimental data, the red, blue and green lines represent the results of the Voigt, Maxwell and Zener Models respectively.

Table 5.1: Results from LFE analysis for the Voigt and Maxwell models presented.

	Voigt				Maxwell		
	μ (kPa)	η (Pa s)	error (m/s)		μ (MPa)	η (Pa s)	error (m/s)
1	1.28	8.83	0.42		5.70	7.63	0.49
2	0.69	4.46	0.29		1.05	3.83	0.33
3	0.98	6.27	0.36		2.25	5.37	0.42
4	0.79	4.99	0.40		4.41	4.26	0.45
5	0.71	4.73	0.28		1.22	4.02	0.33
6	0.64	4.91	0.23		0.54	4.25	0.28
7	0.74	4.88	0.26		2.14	4.16	0.29
8	1.05	6.33	0.26		0.40	5.31	0.31
9	0.71	4.73	0.28		1.22	4.02	0.33
10	0.64	4.91	0.26		1.69	4.24	0.31
11	0.74	4.88	0.26		2.14	4.16	0.29
Mean	0.82 ± 0.2	5.45 ± 1.3	0.30		2.07 ± 1.6	4.66 ± 1.1	0.35

Table 5.2: Results from LFE analysis for the Zener model presented.

	Zener			
	μ_1 (kPa)	μ_2 (GPa)	η (Pa s)	error (m/s)
1	1.28	240.93	8.83	0.42
2	0.69	37.85	4.46	0.29
3	0.98	118.25	6.27	0.36
4	0.79	132.86	4.99	0.40
5	0.71	49.86	4.73	0.28
6	0.64	57.80	4.91	0.23
7	0.74	80.03	4.88	0.26
8	1.05	84.03	6.33	0.26
9	0.71	49.86	4.73	0.28
10	0.64	164.90	4.91	0.26
11	0.74	80.03	4.88	0.26
Mean	0.82 ± 0.2	99.67 ± 61	5.45 ± 1.3	0.30

Table 5.3: Results from FEM analysis for the Voigt and Maxwell models presented.

	Voigt				Maxwell		
	μ (kPa)	η (Pa s)	error (m/s)		μ (MPa)	η (Pa s)	error (m/s)
1	0.42	2.55	0.13		136.99	2.20	0.17
2	0.52	1.97	0.16		10.97	1.60	0.17
3	0.38	2.12	0.13		20.56	1.79	0.16
4	0.54	1.78	0.09		20.54	1.42	0.11
5	1.59	2.72	0.13		0.00	3.17	0.11
6	0.69	2.73	0.04		15.05	2.20	0.07
7	0.61	2.79	0.08		20.23	2.30	0.10
8	1.80	2.54	0.06		0.00	2.76	0.04
9	1.66	3.08	0.04		0.00	3.06	0.05
10	0.69	2.73	0.05		15.05	2.20	0.06
Mean	0.89 ± 0.6	2.50 ± 0.4	0.09		23.94 ± 41	2.27 ± 0.6	0.10

Table 5.4: Results from FEM analysis for the Zener model presented.

	Zener			
	μ_1 (kPa)	μ_2 (GPa)	η (Pa s)	error (m/s)
1	416.33	79.96	2.55	0.13
2	516.57	2.91	1.97	0.16
3	381.68	30.84	2.12	0.13
4	539.06	11.36	1.78	0.09
5	376.00	0.00	3.58	0.10
6	692.67	16.30	2.73	0.04
7	606.66	7.48	2.79	0.08
8	449.17	0.00	3.18	0.03
9	1659.27	17.10	3.08	0.02
10	692.67	16.30	2.73	0.04
Mean	633.01 ± 380	18.22 ± 24	2.65 ± 0.6	0.08

The kidneys do show a distinctive increase of measured elasticity with increasing excitation frequency. The models show that the viscous component is present and influential.

The FEM results do show a better correlation with the models at lower frequencies. The wavelength within the kidney at these low frequencies is close to the size of the image. When this happens it is difficult to determine the exact wavelength. The overall error in the FEM results is less than that of the LFE results as well. For both the LFE and FEM processing methods, the Voigt model had lowest overall error for all the kidneys imaged.

Parenchyma Scanning

In order to look only at the tissue of interest, the parenchyma of the kidney, we dissected the kidney and isolated the parenchyma. In addition to scanning the kidney tissue with ultrasound elasticity, we were able to use a manual indenter to test the static elasticity of the parenchyma. This indenter is made of a precise linear stage and a force sensor [63]. The force sensor is pressed into the tissue at 5 micron increments and force measurements taken after the tissue has settled. Using these results to calculate the elasticity, it was found that the parenchyma was approximately 7 kPa. It is important to note these measurements are taken after the tissue has settled, and in a static manner. This means that the measurements from the indenter are not dependent on frequency, and should only represent the elastic properties of the tissue.

5.5.4 Discussion

We have looked in depth at the viscous tissue characteristics of kidney *ex-vivo*. Constructing an apparatus to provide means of excellent wave propagation throughout the kidney, we have looked at the frequency response of the kidney in order identify the elastic and viscous properties. Using two different elasticity algorithms we have fit different models to estimate these properties. We found that the FEM results generally measured lower elasticity values than LFE on the same phasor data.

When fitting the models to the observed data, the observed error in the Voigt

and Maxwell models was a 0.30 and 0.35 m/s respectively for the LFE analysis and 0.09 and 0.10 m/s respectively for the FEM analysis.

In addition, the sensitivity of the parameters to small changes in the data was measured. Using the original data from experiment 6, which had very low fitting error, small perturbations to the data were made. A random perturbation was made to the original data, up to $\pm 10\%$, for 10 trials. From these 10 trials, the standard deviation of the parameters is shown in Table 5.5. For the Voigt, the resulting standard deviations in the parameters were small, 7.5% and 2% of the mean parameter values. For the Maxwell model, the deviation in the μ and η parameter were approximately 82% and 2% of the mean value respectively. For the Zener model, the μ_2 parameter varied hugely from trial to trial, while the error in the fits do not change much, ranging from 0.15 to 0.10 (m/s). From these results, it shows that the Voigt model is the most sensitive to small changes in the data results.

Table 5.5: The standard deviations in the parameters for each of the three models after 10 trials of up to $\pm 10\%$ perturbations in the original data.

Voigt		
μ (kPa)	η (Pa s)	
0.047	0.092	
Maxwell		
μ (MPa)	η (Pa s)	
0.985	0.096	
Zener		
μ_1 (kPa)	μ_2 (GPa)	η (Pa s)
30.98	126.53	0.15

Given the above results, we explored how changing the final parameters would change the fitting errors. After optimization, each of the parameters was multiplied by a factor of 10, and the fitting error was calculated. For the Maxwell model, the μ parameter could be changed by a factor 1000 with less than a 0.2 (m/s) change in the fitting error. The fit for this model is dominated by the viscous component, and the value of the elastic component has little or no effect on the model.

For the Zener model, the μ_2 parameter could also be multiplied by up to 1000

with little change in the fitting error, less than 0.2 (m/s). This parameter is basically a solid bar, in which case the model simplifies to the Voigt model.

The results of previous *ex-vivo* kidney studies using the SDUV method, found that the elasticity and viscosity of the cortex ranged from 1.7 to 2.3 kPa and 1.8 to 2.2 PaS, respectively [7]. The resulting elasticity component is larger than the values reported for the Voigt model here. Amador *et al.* were able to measure at higher frequencies, up to 500Hz, more than was possible here. It is possible that the higher frequencies changed the model fitting parameters. They also reported only values for a single kidney, some of the kidneys results reported in this chapter fall within this range.

When examining the waves within the kidney, we can see that the waves are deflected and changed by the internal kidney anatomy. When using the steady-state wave technique, it is possible to see the wave propagation throughout the entire kidney and spot these anomalies. They are sometimes correlated with visible differences in the B-mode, but sometimes there is no easily discernible cause. Other issues also arise when there are reflections within the kidney. These are sometimes caused in *ex vivo* situations due to the kidney-water interface. Interestingly, they have detrimental effects on the apparent wavelength but do not show as poorly correlated areas

As mentioned above there have been numerous studies looking at the correlation between kidney fibrosis and elastic measurement, but little consistency in the resulting measurements, we hypothesize that these disruptions in the wave may be the cause for some of the variety in other kidney elasticity results.

One limit of this study is that the measurements were taken on *ex-vivo* kidneys without blood flow. As we have seen from the results of Section 5.4, the input pressure can have an effect on the elasticity results. It is possible that the measurements could be very different quantitative results, but it seems that the trends are fairly consistent so we would expect similar results. These studies go to prove that there are significant viscous properties of kidney tissue that will have an effect on elasticity measurements. For example, when the optimization was run on the same LFE data, assuming no frequency dependency viscous components, the root mean square fitting error for the Voigt model increased from 0.33 to 0.92 (m/s). Individual graphs of the results when viscous components are set to zero can be found in

Section A.2 Figure A.6.

5.6 Discussion

From previous results published in this area it can be seen that there are confounding factors that are complicating the elasticity measurements in kidneys. In these experiments, we have attempted to create a more controlled environment to measure the effects of two of the possible factors, blood pressure with flow and viscosity. From our results, we see that there are pressure and viscous effects on the elastography measurements, and that these are factors that should be taken into consideration when measuring kidney elasticity *in-vivo*.

Unfortunately, even in this controlled environment, it is difficult to control all the possible variables. In a study looking at transducer pressure, Syversveen *et al.* found that transducer pressure was a factor in elasticity measurements [163]. It was difficult to standardize the exact pressure that was placed on the kidney, but care was taken to keep the pressure required to hold the kidney in place constant throughout the measurement process. We used the constant elasticity of the thin silicone to maintain the distance between the transducer face and the kidney, and thus maintain a constant pressure on the kidney. In the future, we would like to add a pressure sensor to our apparatus in order to measure the pressure applied to the kidney during scanning.

In a previous paper describing the effects on elasticity with changes in static pressure, Helfenstein *et al.* also found that increasing input pressure increased the measured elasticity in *ex-vivo* kidneys [61]. Using ARFI imaging, they measured the elasticity as it changed from 0 mmHg to 120 mmHg. Interestingly, the measured elasticity at 120 mmHg was much more variable than that measured at 0 mmHg, with measurements ranging from 8 kPa to 35 kPa. This is similar to our findings, in that the standard deviation in the measurements at 0 mmHg was 3 kPa but at 130 mmHg our measured standard deviation was 9 kPa. They also measured the changes with depth, but found they had trouble measuring the entire depth of the kidney into the collecting system because of the limitation of using ARFI at higher depths. Fortunately, our imaging method, SWAVE, does not suffer from this limitation.

Helfenstein *et al.* noted that the kidney increases in size as perfusion pressure increases; something we noted as well (Figure 5.10). This happens as the kidney expands to hold and filter the blood. As the same organ must now hold more fluid, changes in the tissue result in changes in the measured elasticity. The tissue must stretch to accommodate the extra fluid.

The kidney reacts to the dynamic changes in blood pressure as well. The kidney has an autoregulation mechanism to create constant filtering pressure inside the kidney, such that the changes in blood pressure throughout the heart cycle do not affect the functionality of the kidney [82]. Depending on when during the heart cycle each elasticity measurement is made, the result may vary. These changes may account for the variability in the results of previous papers.

As changes in blood pressure and the dynamic changes in the kidney could affect the elasticity, it becomes reasonable that the measurement timing should be synchronized with one temporal location in the heart cycle. One paper mentioned that synchronizing the measurements of healthy volunteers with the Electrocardiogram (ECG) measurements resulted in better correlation between the EGFR of the volunteers and the measured shear wave velocities [9]. EGFR is used as a measure of the function of the kidney and an estimate of the level of CAN. This only goes to reinforce the idea that ECG synchronizing should become standard when taking elasticity measurements.

Presented here is a preliminary investigation of the effects of changes in blood pressure on the elastography measurements of kidneys within a controlled environment. We have seen that the measured elasticity increases with increasing pressure and in order to consistently use elastography as a method to measure fibrosis and the progression of CAN, the perfusion pressure and flow need to be measured or synchronized.

Looking at the results of the viscous measurements, we have found that the tissue has a viscous component that should be accounted for during elasticity measurements. This also applies when comparing different types of elasticity imaging. These comparisons can be difficult as frequency dependency is not accounted for during the comparisons of shear wave speed or estimated Young's modulus. The measurement of viscous components could also be used in conjunction with other information to make more definitive diagnosis. In Section A.2 Figure A.5, the indi-

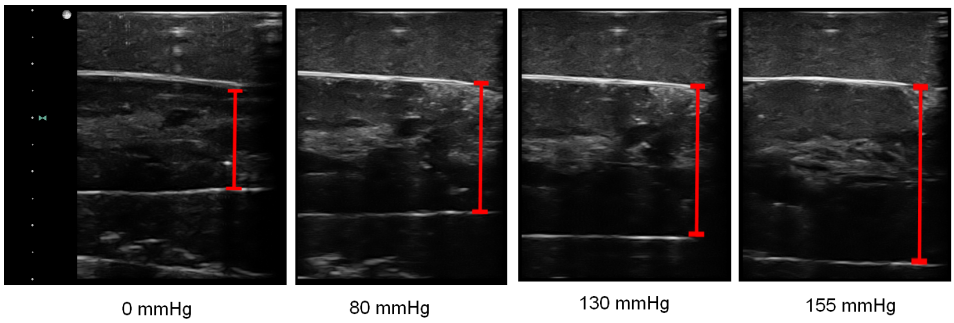

Figure 5.10: Cross-sectional images of the B-mode image of the kidney at different input pressures. The bars on the right side each cross section denote the two surfaces of the kidney. The width of the kidney increases with pressure. The width was measured as 2 cm at 0 mmHg, 2.25 cm at 80 mmHg, 2.75 cm at 130 mmHg and 3.25 cm at 155 mmHg.

vidual graphs for each kidney are shown separately. When looking at these graphs, it is important to note how little difference there is between the fit of the three different models. When looking at the sensitivity to both changes in the data and changes in the final parameters, the Voigt model was least affected by these. When using these models in the future, only the Voigt model will be presented as it is the most representative of the tissue of the three.

In some cases, the slope of the fit is not close to the data as desired. This could be an indication that none of these models are entirely applicable to renal tissue and other models should be considered, such as a poroelastic model [84].

When looking at the results with the Voigt model, the fitted elastic component is about 0.5 kPa, with is considerably lower than all the results reported in literature with any machine. It is also lower than the static elastic component measured with the indenter, as it was about 7 kPa. It is possible that these methods are too simple and that other tissue properties need to be taken into account, such as the porous nature of tissue [84] and compressibility. But it is important that there is a large viscous component in kidney tissue that cannot be taken for granted.

In particular, this viscous component does not just affect the elastography methods where excitation frequency is inherent, such as SWAVE or MRE. The viscous component also affects ARFI and SSI wave speed calculations. The push

pulse used in these methods has a spectrum of frequency components. The resulting wave front speed is measured either by measuring the peak displacement of the tissue some distance away from the push pulse [41], or by measuring the velocity of the tissue motion. When measuring the velocity, the derivative of the displacements is taken. This derivative acts as a high pass filter on the spectrum of the wave, weighting more heavily on higher frequencies and resulting in differences in measured elasticity [126].

During the viscous property testing, we looked at the same data with two different analysis techniques, LFE and FEM and presented the results. We were also able to examine the wave images of the kidney and determine that it is a complicated organ, and careful measurements are required in order to avoid artifacts caused by ultrasound and anatomy.

5.7 Conclusion

An apparatus was created for imaging *ex-vivo* kidney tissue. In doing so, the kidney was imaged at multiple different input pressures and excitation frequencies. A study of how the tissue characteristics change with increasing input kidney pressure was completed. It was found that input pressure does affect the measured elastic properties.

When quantifying the viscous component of the tissue by fitting the measured wave speed to three different mechanical models, it was found that the measured wave speed increases with increasing excitation frequency, showing that the kidney has viscous characteristics. Of the three models used in these experiments, the Voigt model was least sensitive to changes in the data and most sensitive to changes in the final parameters. This model will be used to model tissue in the remainder of this thesis.

Very limited data regarding the kidney is currently available, so it is hoped that the results presented in this chapter will expand the understanding of kidney tissue characteristics.

Chapter 6

Measurements of Transplant Kidneys *in vivo*

6.1 Introduction

The ultimate goal of calculating the elastic properties of the transplanted kidney is to be able to monitor the health of the kidney in a non-invasive manner. It would be of great benefit to the patient to be able to obtain the same information which would be collected from histological interrogation but without the need for biopsy [149].

We have chosen to examine transplant kidney patients specifically due to the fact that transplant recipients are an at risk population, with only a single functional kidney and taking immunosuppressants. This means that these patients could benefit from incremental improvements in monitoring. It has been described in Section 1.2.3, a transplant is preferred to long term dialysis, but transplanted organs have a limited lifetime [131]. It is vital that the transplanted kidney be preserved to avoid the need for repeated transplants, which creates additional demands on the number of available transplants, not to mention an additional procedure for the patient, with all the associated risks. The location of the transplanted kidney, near the surface of the skin, makes them easy to image and locate, in comparison to native kidneys which are more protected by the ribs.

For this preliminary study, our goal was to determine the feasibility of using

SWAVE to measure the wavelength and elasticity of transplanted kidneys *in-vivo* in a range of patients, and compare the results to the patients' current EGFR and latest biopsy findings. Since all patients in this study have recent graft biopsy results, the possible correlation between the level of fibrosis as reported in the biopsy and the initial elastic measurements can be examined in this small patient population. We have started this study with results in 23 patients.

As described in the previous chapter, SWAVE has been used to image the elastic properties of phantoms and *ex-vivo* kidneys. The difficulties and complications of imaging kidneys have been explored and some limitations exposed. In this chapter, this knowledge is now applied to patients who in the future could derive some benefit from this work.

6.2 Patient Populations

Patients were recruited from the Transplant Clinic at VGH. Patients were requested to come for an additional ultrasound elastography scan after their normally scheduled appointment at the Transplant Clinic. Patients were called at least two days ahead of their appointment at VGH. All patients had received at least one kidney transplant, though the time since transplant varied widely. All imaging was performed under the ethics protocol H09-02455 *Elastography in Transplantation*.

Patient characteristics are outlined in Table 6.1. The patient's blood pressure and EGFR were measured on the same day as their Transplant Clinic appointment and elastography scan. Previous work has compared the kidney stiffness to EGFR [8, 103, 115] as well as biopsy, so this variable will be used along with the biopsy results.

6.3 Patient Histology

The gold standard for fibrosis assessment is histology from a biopsy of the kidney. An ultrasound guided biopsy is taken from one or both poles of the kidney. The tissue is then sent to pathology to be stained and examined under a microscope. A biopsy report from the pathologist is submitted and read by the physician to determine the level of fibrosis. Many pathologists use the Banff Scoring system described in Section 1.2.3 [155]. In the event that the pathologist does not explicitly

Table 6.1: Characteristics of the patients in this study.

Patient	Age (Years)	BMI	Blood Pressure	eGFR	Time Since Transplant (Days)	Banff Score
1	57	30.1	148/87	95	406	0
2	55	31.5	148/85	56	7987	2
3	56	22.5	138/75	26	470	0
4	52	30.4	126/60	45	2378	0
5	34	18.3	156/94	11	2935	2
6	73	26.5	132/62	81	5258	1
7	77	20.0	110/79	41	4392	0
8	43	28.1	119/89	5	2340	2
9	64	23.4	140/64	26	29	1
10	56	33.3	120/72	39	26	1
11	37	21.8	120/70	45	1956	0
12	48	21.5	118/74	31	422	0
13	50	25.0	110/78	5	3083	1
14	47	23.6	120/83	38	120	1
15	66	26.3	155/76	46	135	1
16	54	21.6	132/78	70	358	0
17	78	29.2	117/62	41	1470	0
18	32	20.0	100/69	106	494	0
19	45	17.7	105/70	57	46	0
20	64	21.4	157/89	17	2537	2
21	40	32.2	138/82	72	64	0
22	71	26.1	140/72	54	40	0
23	60	21.6	118/70	45	38	2

use this system, the level of fibrosis according to the Banff system is determined from the pathologist's notes and comments.

The recruitment for this study is ongoing, and additional patients will be included in the future. The results of the most recent biopsy will be used for comparison in this and future studies. In the case in which the patients were coming in for routine appointments, the most recent biopsy was used. For these patients with stable grafts, it was assumed no major changes have occurred between the most recent biopsy and the elastography scan. For patients who had very recently received their transplant, results from the implant biopsy will be used during the comparison.

6.4 Imaging Procedure

Each patient was asked to lie in a supine position on the exam bed. The kidney was first located and imaged with clinical ultrasound imaging software using a C4-7 transducer and an Ultrasonix Touch ultrasound machine. This transducer is a curvilinear transducer often used for abdominal scans. Once an optimal location for the ultrasound transducer had been identified, the ultrasound transducer was fixed in place using a Civco Positioning Arm mounted on the side of the bed. At this time the optimal depth of imaging was also determined. It was desired that the entire kidney be visible within the image. It is important that the wave pattern throughout the graft be seen, to be certain there was adequate wave propagation during image acquisition. All patients were imaged at depths between nine and twelve centimeters, depending on the size of the patient and location of the transplanted kidney. In the cases of these patients, the kidney was not seen to move excessively with breathing, so patients were not instructed to hold their breath. Each scan of 25 frames required about 20 seconds to acquire.

Each kidney was imaged along its two major axes. The first position of the transducer creates an image showing the long axis of the kidney, which allows for a visible distinction between the cortex and the collecting system. The second position of the transducer images the kidney in cross-section. Figure 6.1 shows two of the optimal kidney ultrasound images from these patients.

The shaker was placed on the patient's skin as close as possible to the trans-

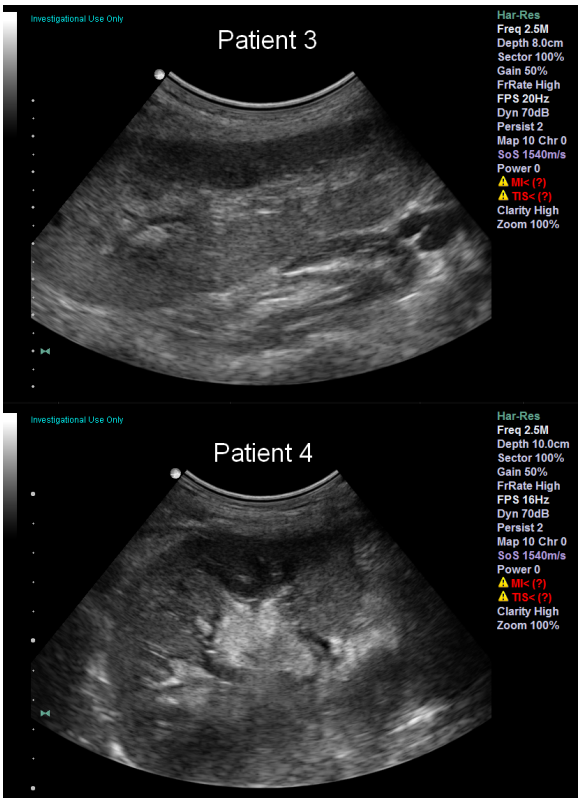

Figure 6.1: Two example ultrasound images of the transplant kidneys, long axis views. Top: Patient 3. Bottom: Patient 4.

ducer to allow for the most possible wave displacement within the kidney. Several placements of the shaker were tested around the transducer to determine where the most consistent waves were produced. The waves were monitored in real time using the eScan software. A lateral placement of the shaker with respect to the transducer was typically best as this maximizes components of the shear wave motion in the plane of the ultrasound image.

A series of images were collected from each patient. Each set of images included 25 frames. Three sets of 25 frames were collected at each frequency and each kidney was imaged at 50, 75, 100 and 125 Hz. In total, 600 2D images were collected of each kidney.

Due to issues with motion during acquisition, the frames were filtered and those

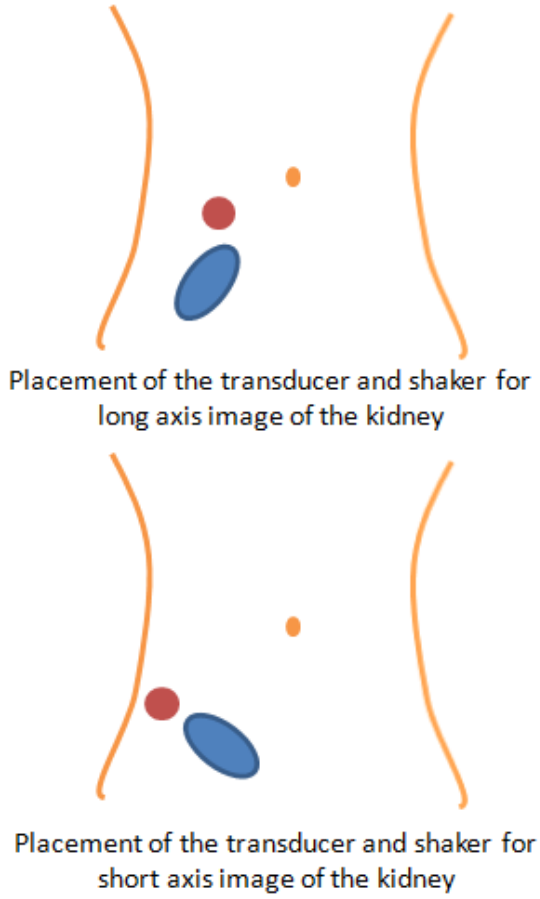

Figure 6.2: An example sketch of the placement of the ultrasound transducer (blue oval) and shaker (red circle) on the lower abdomen of the patient for both the long axis and short axis views.

showing motion artifacts were discarded. Motion artifacts were created when the patient shifted position, coughed, or took an unusually deep breath. Patients were instructed to try to hold still during image acquisition, but this was not always possible.

The cortex and collecting system of the kidney were manually segmented from the B-mode images. Although automated and semi-automated segmentation algorithms exist for ultrasound images [18], it was more efficient in this case to segment the B-mode images manually, as most would have required manually seeding. Be-

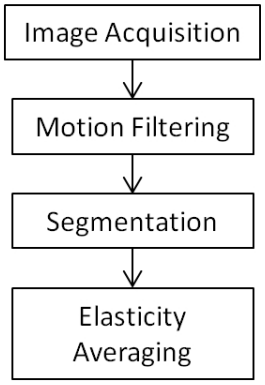

Figure 6.3: A flow chart describing the steps of image processing.

cause the measured stiffness in the cortex and the collecting system of the kidney could be quite different, the cortex and the collecting system of the kidney were manually segmented separately.

The elasticity within the kidney area was calculated using LFE methods [105] and averaged across all the 2D images of that frequency that did not show motion artifacts [Figure 6.3]. These elasticity values were then compared to each patient's health characteristics and to the results of other studies.

As discussed in Chapter 5, the kidney is not an entirely elastic tissue, but also has viscous properties. To compare the results of the *ex-vivo* studies with these *in-vivo* studies, the measurements were fit to the same Voigt model described in Figure 5.7.

6.5 Patient Results

The results of the elasticity measurements using LFE were compared to a variety of different patient characteristics including the patient histology as defined by the Banff Score, EGFR and patient blood pressure. Figure 6.4 shows that the general trend from pervious literature holds true, that patients with higher Banff Scores, also have lower filtration rates.

Figure 6.5 shows the relationship between the measured Young's modulus (estimated at 85 Hz) and the patient's EGFR.

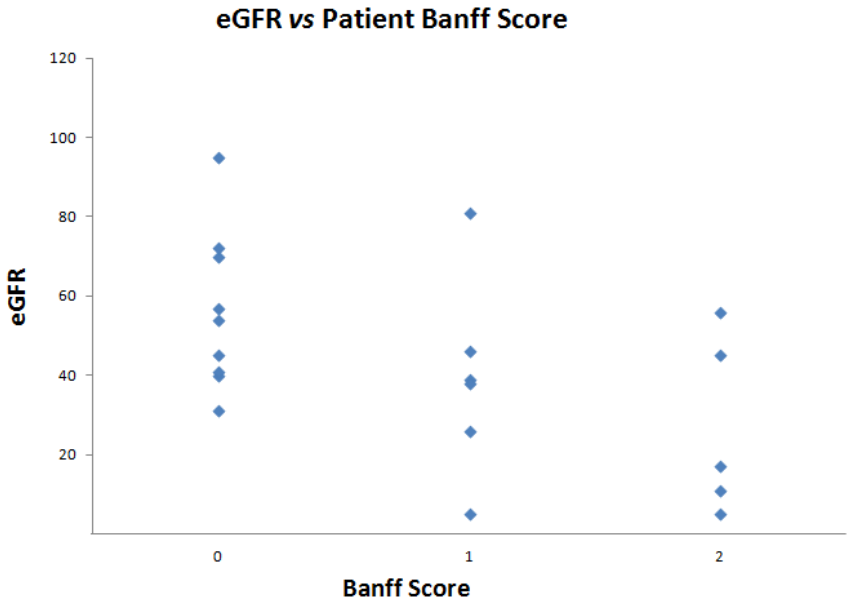

Figure 6.4: The patients' estimated glomerular filtration rate vs the Banff Score from the most recent biopsy.

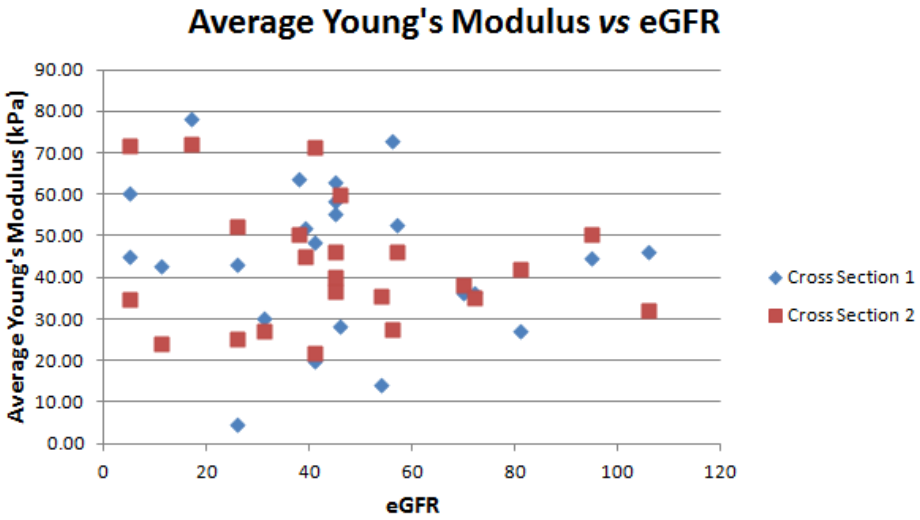

Figure 6.5: The average measured Young's modulus *vs* the estimated GFR for both cross sectional views for all patients.

Because some of the waves patterns within the kidney changed depending on their location with respect to the anatomical structures of the kidney, the phasor (wave) images of Patient 4 are presented in Figure 6.6. It is possible to see the differences between the waves within the cortex of the kidney and those of the collecting system. The outline of the cortex and the collecting system are defined in the B-mode image and then overlaid onto the phasor images at each frequency. It can be seen the wavelength in the collecting system is much shorter than the wavelength in the cortex. Also, as expected, the wave pattern within the kidney changes with increasing frequency.

The shorter wavelength in the collecting system causes a change in the measured Young's modulus, creating a softer region within the center of the kidney. This was most apparent in the long axis view of the kidney, where more of the collecting system was visible in the ultrasound image. In Figure 6.7, the average Young's modulus for the cortex and collecting system at each excitation frequency are shown. Using only the results from the long axis view of the kidney, a T-test was performed ($p = 0.07$).

It was found that the measured Young's modulus for the transplant kidneys generally increased with excitation frequency (Figure 6.7). This indicates that the kidney exhibit some viscous properties, similar to what was found in the *ex-vivo* studies.

The resulting elasticity measurements were fit to the Voigt model in order to estimate the viscous properties of the kidney tissue (Chapter 5) and outlined in Table 6.2. And the fitting error is defined as follows:

$$\xi = \sqrt{\frac{1}{6}\sum_{i=1}^{4}(c_s(\omega_i, X) - \hat{c}_s(\omega_i))^2} \tag{6.1}$$

The individual model fitting graphs for each patient are found in Appendix A.2.

As the blood pressure was one aspect measured in the *ex-vivo* studies, the patient's blood pressure was compared to the measured Young's modulus. Figure 6.8 shows how the patient's blood pressure corresponds with the measured Young's modulus. The patients' systolic, diastolic, Mean Arterial Pressure (MAP) and the difference between systolic and diastolic (Delta P) are shown.

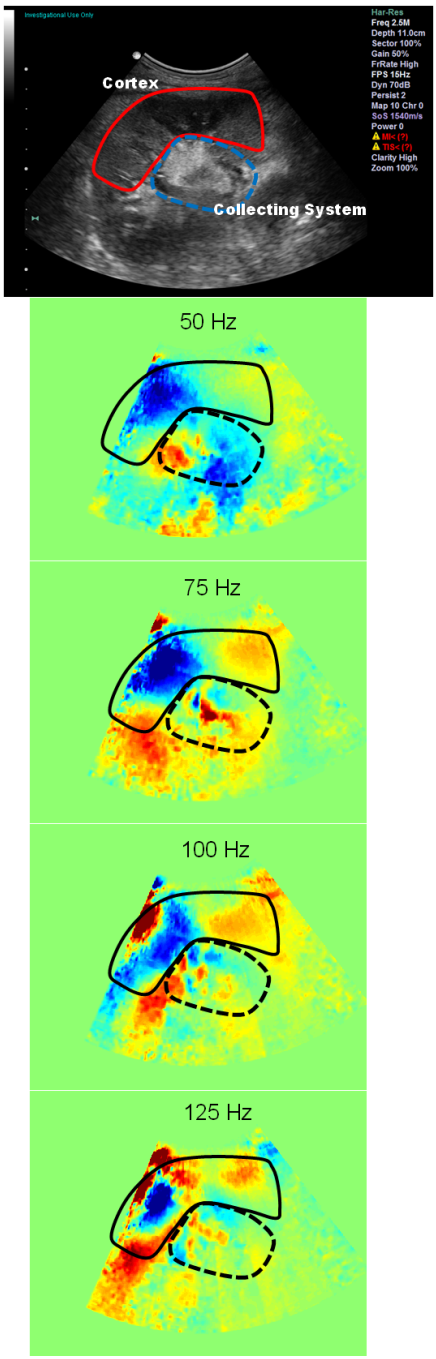

Figure 6.6: B-mode and wave images of Patient 4 at each frequency used in this study. The outline of the cortex (solid line) and collecting system (dotted line) have been overlaid on the images.

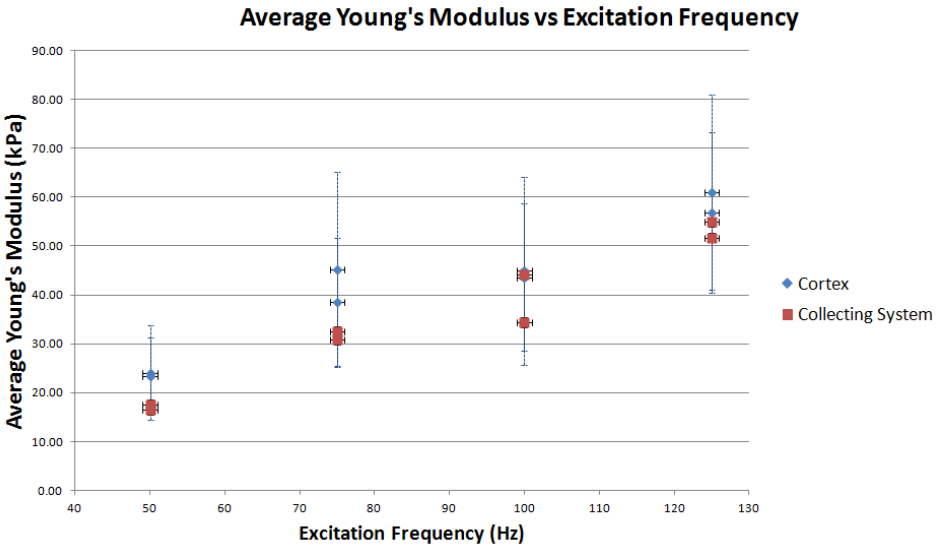

Figure 6.7: The measured Young's modulus of the cortex and collecting system *vs* the excitation frequency.

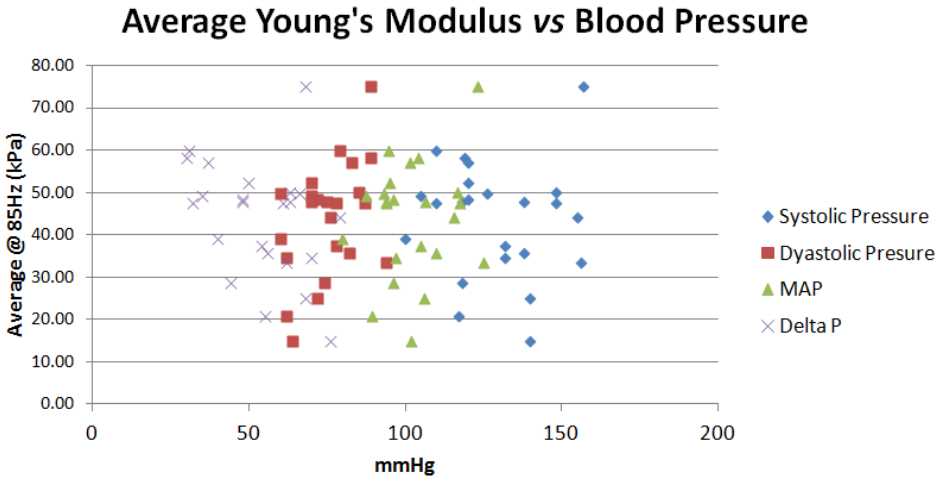

Figure 6.8: The patient results measured Young's modulus as compared to the patients' blood pressure taken on the day of the ultrasound scan.

Table 6.2: The Voigt model fitting results for patients. Each cross sectional view for each patient is represented separately. The top half of the table represents the long axis view and the lower half represents the short axis view of the kidney.

Patient	μ (kPa)	η (Pa s)	Fitting Error (m/s)
1	1.3	15.8	0.29
3	2.2	16.2	0.27
4	6.4	13.7	0.60
5	7.5	16.1	0.50
7	13.2	12.9	0.52
8	1.9	16.5	0.30
10	13.1	15.4	0.59
12	1.4	11.3	0.44
14	13.8	22.2	0.50
15	4.5	11.0	0.30
16	7.9	12.6	0.44
18	7.7	17.5	0.74
19	2.6	19.6	0.15
21	10.3	8.8	0.49
22	4.0	14.1	0.39
23	9.4	13.2	0.06
Mean	6.7 ± 4.2	14.8 ± 3.2	0.4

6.6 Discussion

The results here are presented using either the Banff Score or the EGFR as an indicator of kidney heath. Unfortunately, both of these measurements, which are used as a gold standard in practice, have limitations. The Banff Score is given based on biopsy results from the kidney, but only has 4 levels of differentiation. Also, since this score is based on a small sample of the tissue, it is possible that the score does not represent the entirely of the kidney. It may be that the fibroses forms in patches of the kidney and a biopsy could either over represent or under represent the level of fibrosis.

The EGFR also has some limitations. The EGFR is based one of several formulas which include the level creatinine in the blood serum (plasma) and the patient's characteristics, such as age, gender, body size and race. The serum creatinine though, can be affected by other factors, not directly related to kidney function, including the muscle mass of the patient and even whether the patient has eaten a large amount of red meat that day. A more accurate measure of glomerular filtration rate would require taking a complete urine collection over a 24-hour period, which is also difficult and prone to error.

When looking at the differences between the Young's modulus in the cortex with compared to the collecting system, the collecting system was on average 10 kPa softer than the cortex. Although the difference in the measurements were not statistically significant ($p = 0.07$), this difference in measurements shows that these two tissue types are distinct.

Unfortunately not all the patients could be scanned at 125 Hz excitation frequency due to problems with wave propagation. In the patients with high BMI, the distance between the excitation source and the kidney was greater than the wave penetration. In this case, insufficient displacements were induced in the cortex of the kidney. Only those patients with all four excitation frequencies were included in the model fitting.

It is interesting to note the differences in Table 6.2 with the model fitting results of the *ex-vivo* kidneys. The average elastic parameter, μ, was 0.82 kPa and 5.45 Pa s for the viscous parameter η for the *ex-vivo* kidneys. In comparison, the results of fitting the *in-vivo* kidney resulted in 6.7 kPa and 14.8 Pa s. The differences in these parameters may be attributed to the fact that the kidneys measured *in-vivo* were influenced by uncontrolled variables such as abdominal pressure, bladder pressure and potential changes in perfusion. These differences could also be attributed to differences between porcine and human kidneys.

These *in-vivo* results were also calculated from 2D images, where as the *ex-vivo* results used 3D volumes. It was assumed that most of the shear wave motion was confined to the plane of the ultrasound image, but this may not have been strictly the case. With only a 2D image of the wave motion, it is difficult to compare the results of the measured Young's modulus as an absolute measure.

6.7 Conclusions

We have shown that at least in our limited patient study, we were able to generate and image shear waves in transplanted kidneys, in a safe and comfortable manner, through the use of a small mechanical shaker placed on the skin of the patient.

After optimization of the quality factor, the most reliable frequency range was determined to be between 50 Hz and 125 Hz. This range is higher than the typical range used for liver imaging, 45-60Hz, but closer to the range used for kidney imaging in previous MRE papers. This range provided a compromise in the tradeoff between the resolution of the imaging (higher frequency is better) and the wave propagation and penetration (lower frequency is better). At 50 Hz, the wavelength approximate the length of the kidney, resulting in possible inaccurate wavelength estimation. While at 125 Hz, there were challenges with wave propagation throughout the kidney, especially in larger patients, as wave attenuation could be quite high, and the distance between the patients skin and the kidney, quite large.

This study showed that the *in vivo* kidney, not surprisingly, also exhibits viscous properties like those found in *ex-vivo* porcine kidneys. These properties should be taken into account in future examinations and when comparing results of different methods and excitation frequencies.

Chapter 7

Conclusions and Future Work

7.1 Overview

This chapter provides an overview of work presented throughout this thesis and puts it in context of current research. The contributions to the field and the limitations of this approach are also described. The chapter concludes with a description of the future directions for this work.

7.2 Summary of Findings

Chapter 2 presented the use of the intra-operative ultrasound transducer designed specifically for use with the da Vinci surgical robot. This chapter looked at the different tracking methods for the transducer, including the use of robot kinematics, electromagnetic sensors and stereo camera tracking. A vessel phantom with embedded targets was used to validate the tracking and 3D reconstructions of each of the three methods. The camera tracking turned out to have the lowest reconstruction accuracy, but may be improved through the use of different stereo camera tracking implementations. Due to overall accuracy and practical considerations, it was decided to use the da Vinci kinematics as the main tracking method moving forward.

The next chapter highlighted the use of the intra-operative ultrasound transducer described in Chapter 2 for use in elastography measurements. Focusing on

measuring the tissue properties of kidney tumours during partial nephrectomy, the transducer allows a surgeon increased autonomy during surgery. Two different methods for collecting elastography images were developed. The first uses the clinical mode on the da Vinci robot, which only allows the kinematics to be read from the robot. This method requires the surgeon to move the transducer very slowly and use the 'clutch' pedal to activate the image collection. The second method leverages the research interface to the robot to automate the transducer motion during image collection. The results of the volumes collected on elastography phantoms using these two different methods were presented here.

In order to move elastography measurements into kidney tissue *in-vivo* it is imperative to understand the results and the limitations of the past work in this area. Chapter 4 takes an in depth look at the different results from different elastography imaging methods including strain imaging, FibroScan, ARFI and MRE. There is a large amount of variation in the presented results both within the methods and between the different imaging types, so other factors are also identified. The possible confounding factors are explored, such as arterial pressure, transducer pressure, and tissue heterogeneity. Two factors were identified to study further. The first is the perfusion pressure of the kidney which has only been studied directly in one study [61]. The second factor to explore further is the tissue viscosity. Tissue viscosity is a known but little studied tissue property that could have large effects on the measured elasticity of the kidney tissue.

Chapter 5 looks at these two factors in more detail using a controlled *ex-vivo* set-up. Fresh porcine kidneys were harvested and flushed according to transplant kidney procedures. An apparatus was designed to hold the *ex-vivo* kidney in a way that was well constrained and repeatable. Using a peristaltic pump and pressure gauge, the input pressure to the kidneys was carefully controlled and it was seen that at increasing arterial pressure, the measured elasticity also increased. This corroborates the earlier papers outlined in Chapter 4 that show some general *in-vivo* trends between the arterial pressure and measured elasticity.

The apparatus also allowed for in depth exploration of the viscous properties of the kidney tissue. The *ex-vivo* kidneys were excited at frequencies from 50 to 250 Hz. From these measurements, an increasing trend of measured elasticity with excitation frequency can be seen. These results were fit to three different

mechanical models in order to identify the viscous and elastic properties of the tissue. It was determined that there are non-negligible viscous properties that likely contributed to the variations seen across previous results. It was also found that the Voigt model was less sensitive small changes in the data and most sensitive to changes in the final parameters than the other two tissue models.

In the last chapter of this thesis, the measurement of kidney elastography was applied to transplanted kidneys *in-vivo*. Although the results of only 23 patients are presented here, it was proved that this type of scanning is possible and can be reliably performed. The SWAVE technique for measuring transplanted kidney elasticity is feasible in this setting and good wave propagation within the kidney was noted. Similar to the findings in *ex-vivo* kidneys, the *in-vivo* kidneys also exhibit strong viscous properties. Within these preliminary patients, there were no strong correlations between measured elasticity and biopsy results.

7.3 Implications

The implications of the work presented in this thesis reach across the spectrum of kidney tissue characterization. The results from Chapter 2 and Chapter 3 may have an impact the surgical work flow of difficult kidney surgeries, while the work presented in Chapters 5 and 6 attempts to explain the widespread variability of elastography results and provide the first steps towards understanding how to standardize kidney imaging.

The ultrasound transducer described in Chapters 2 and 3 provides the surgeon with a tool to extend his/her vision during surgery, specifically during the complicated and time sensitive partial nephrectomy procedure. The tracking and reconstruction accuracy has been determined, such that the transducer can be used during surgery to provide the surgeon with a better understanding of anatomical structures under the surface, which are not visible through the camera. Creating a transducer specifically designed for the da Vinci robot means that ultrasound integration is more streamlined, the surgeon is more autonomous and can be more efficient. Possible registration of preoperative images also provides the surgeon with better context of the patient's anatomy, minimizing errors and increasing the surgeon's confidence.

Adding quantitative ultrasound elastography to the da Vinci robot gives the surgeon additional surgical guidance during robotic surgery. Surgeons can use the information provided with the ultrasound elastography to find the boundaries of the tumours within the kidney, as the tumours are generally stiffer than the healthy tissue. Even when the extent of the tumour is not obvious within the traditional ultrasound image, surgeons would be able to assess the proper cutting planes to increase the probability of positive surgical margins and complete removal of all cancerous tissue. This would lead to better long-term patient outcomes.

The automated implementation of quantitative ultrasound elastography for the da Vinci robot is one step towards the integration within the robotic platform in a way that is acceptable and easy to use for the surgeon. In the lab, it has been seen that creating a freehand 3D elastogram can be tricky and user dependent. The manual forward/automated backward scanning approach allows the surgeon to create an elastogram of a specific user-defined region in a simple and safe way, without needing to understand the particulars of the method. This novel use of the robot capability could be used not only for elastography, but also for general imaging scans in which a slightly corrected trajectory is used for data acquisition.

The implications of our work on patient health are expanded by the application of ultrasound elastography to the characterization of kidney transplants. If elastography is proven to correlate well with kidney health, the health of a patient's transplanted kidney could be monitored more often without the need for additional biopsy, which presents additional risks for the patient.

Looking at previous work in the area, it became clear that a more careful and targeted approach was needed as confounding factors of the imaging were leading to inconclusive results. Of the different factors, the impact of input pressure on elasticity measurements and defining the viscous properties of the kidney tissue was examined in detail. From the experiments presented in this thesis, it has been shown that these have an impact on the measured elasticity and should be considered in kidney tissue models, regardless of the elastography imaging method used. In order for ultrasound elasticity of the kidney to come into more widespread use and regular practice, it is imperative to understand how different factors can affect the resulting measurements. Without a better understanding of what can affect a measurement and how the measurements can be confounded, it becomes impossi-

ble to compare results across patients, elastography imaging methods or platforms to gain an overall understanding of transplant kidney health.

All the factors which were identified to influence the elastic measurements can be applied to both trans-abdominal scanning of kidneys and intra-operative imaging described in Chapters 2 and 3. Understanding renal tissue characteristics will also allow better understand of kidney health during a procedure. These characteristics could also enhance the contrast between the healthy tissue and cancerous tissue, or allow better distinction between benign and malignant tumors.

7.4 Limitations

Although extensive testing in *ex-vivo* setting has taken place on both phantoms and *ex-vivo* tissue, the new ultrasound transducer has not yet been tested in an *in-vivo* setting. It is not expected to change the outcomes of any of the work presented here, but the specific design and expectations for tracking may change as a result of the constraints of an *in-vivo* environment. In this type of setting, the space constraints and lighting may change how the different methods of tracking the transducer are used.

The integration of automated ultrasound elastography into the robotic surgical system is limited by the use of the DVRK, which is not approved for clinical use. This is a proof of concept to show that this type of imaging may be a useful surrogate for the lack of haptic feedback during robotic surgery, providing the surgeon with additional guidance.

During the *ex-vivo* studies, it was difficult to control for the variations of the porcine kidneys used. The kidneys were harvested from pigs used during other studies, and some may have had other unknown diseases which may have changed the kidney. As an example, some of the kidneys had large cysts and were rejected for use in the work presented here. In addition, the original studies were often times invasive training labs for surgical residents. The kidneys may have undergone some type of injury during the study, such as unusually high blood pressure or periods of warm ischemia. All kidneys were harvested very soon after euthanasia, but slight variations in timing were not accounted for. Small changes in the kidneys could have an affect on the results here, but it is felt that all the presented conclusions are

valid.

Another limitation within the *ex-vivo* work was that porcine kidneys were used. Porcine kidneys are often used in the literature as a substitute for human kidneys, but it is possible that the differences in the anatomy could contribute to differences in results compared to human kidneys.

The obvious limitation to the patient study is the number of patients, which will be remedied in the near future. These initial patients were also only imaged in two 2D cross-sectional planes. This changes the measurement of the correct wavelength if there is significant out of plane motion. The vibration source was placed laterally to the ultrasound transducer to limit this effect, but it would be more accurate to take 3D volumes of the kidney. 3D volumes would also allow for more of the kidney to be measured effectively.

7.5 Future Work

The da Vinci transducer, described in Section 1.6.4, has received approval for human trials, and clinical trials are in the planning stages. The accuracy of the tracking within the surgical environment will be tested, also completing 3D reconstructions on the vessel structures of the kidney. From a preoperative CT, the vessels can be segmented and used for registration. The anatomical landmarks such as the vessel bifurcation locations and vessel direction vectors could be used as targets for the registration.

Also, the three tracking methods have only been tested individually. Because some of these methods are more accurate at different stages of a procedure, development of a smart method for integrating all three is needed. Decisions need to be made as to when one method should be trusted more than another, or weighting schemes could be developed. Testing within an *in-vivo* and surgical environment would also provide a better understanding of how each tracking method performs under 'real-world' conditions. For example, blood and smoke can affect the stereo camera tracking, metal instruments cause errors in the EM sensors and large forces applied to the robotic instruments can create apparent kinematic errors. Each of these potential issues should be quantified.

The next step in this project involves how to display the resulting ultrasound

volumes to the surgeon in a way that is understandable and does not distract from their task. The method in which the information is displayed is critical for both surgeon acceptance and the proper interpretation of the information [153]. The use of augmented reality is a popular method for this type of display but challenges still exist as to how best to show the images and which images are best used [70]. These are research areas in which this ultrasound transducer can accelerate the creation of different augmented reality systems since it can provide real-time tracked ultrasound images integrated into a system which already uses a stereo display.

The SWAVE elastography system could be enhanced through the addition of alternate inversion methods, rather than the current LFE method [105]. For example, FEM inversion may be less prone to artifacts within the elastograms. Since frame rate is a limiting factor on the excitation frequency, the use of plane wave imaging to measure the displacements would allow for faster acquisition over the entire plane rather than relying on the sector method currently implemented. This increase in frame rate would also limit the effects of patient motion on the images.

More *ex-vivo* experiments should take place to increase the sample size of the measurements. Further adaptation of the apparatus to hold the *ex-vivo* kidney would allow better control over the direction of the shear waves created within the tissue. Due to the directional nature of the fibers within the kidney cortex, it is important to better understand the magnitude of the effect on the shear wave speed.

It has been shown here that the pressure can affect the measured elasticity of the kidney. In the work presented, the change was large enough to warrant that it be taken into consideration during future studies. One way to do this would be through ECG gating of the image acquisition. An initial study could collect images at different times within the heart cycle to measure the changes in measured elastic properties of the tissue. Once an optimal time within the heart cycle has been determined, image collection could be timed to occur at the same time within the heart cycle and thus be consistent.

Interesting connections between kidney disease and arterial stiffness have been pointed out and also warrant further investigation [51]. The connection between measured kidney stiffness and fibrosis may not be as straightforward as it seems. Many other factors may be contributing to changes in the kidney and need to be better understood before general statements can be made.

In the future work for the patient studies, it is imperative to collect further data from more patients with a greater variety of kidneys. The full spectrum of kidneys should be represented, from newly implanted kidneys to transplant kidneys which have failed to the point where the patient must return to dialysis. Also, additional patients who have had a 'for cause' biopsy will be invited to participate in the study. These are patients who have been referred to the Ultrasound department for biopsy due to some concern or symptoms, such as a rejection episode. Patients will be invited for elasticity scanning about 6 weeks post biopsy, in order to allow any inflammation of the kidney to subside. The short time between the biopsy and scan will provide the most accurate data for this study. If possible, it would also be of interest to scan these patients on the day of biopsy and 6 weeks post biopsy to compare any effects of the possible inflammation. In particular, this would allow the changes due to inflammation to be separated from changes due to fibrosis build up. Inflammation or infection may have a greater effect on the viscosity measurements of the kidney as it increases the fluid within the tissue. If inflammation of the kidney can be reliably detected, changes in patient treatment can be applied soon, to prevent further rejection episodes and the longer term build up of fibrotic tissue.

Overall, any changes in the patients' biomarkers such as biopsy results or EGFR can be compared to elasticity measurements over time. This would give researchers and doctors a better idea of the relation between the patient's health and the measured elasticity.

As was discussed in Chapter 5, the input pressure on the kidney has an effect on the measured elasticity properties. This has not yet been incorporated into the patient scanning procedure, through the use of ECG gating, but will be incorporated within the next months. The time of scanning with respect to the heart cycle can be standardized for each patient.

The current patient data sets were also limited to 2D frames of the transplanted kidney, in two different cross-sections. This limitation was in effect due to the issues with motion artifacts. Through the use of faster imaging techniques and motion compensation, the image capture can be expanded to 3D volumes. With 3D volumes, more accurate elasticity measurements can be taken since the full wavelength in any direction can be measured. In the measurements presented in this sec-

tion, the position of the shaker was specifically positioned in the lateral direction of the ultrasound transducer, to maximize the amount of in-plane displacement.

The differences between elastography imaging methods requires standardization so that it is possible to compare the results from patients across imaging techniques, manufacturers and care centers. In the realm of liver elastography, the Radiological Society of North America is currently attempting to standardize the scanning technique and provide quantification phantoms [17]. These phantoms could be used by all of the ultrasound manufacturers to calibrate their machines and methods, such that all machines output the same quantifiable results. In the future, as the area of kidney elastography matures, similar efforts could be applied for the overall benefit of kidney elastography.

7.6 Conclusion

This thesis presents the work to further the efforts in characterization and quantification of kidney tissue. Through the use of a small intra-operative ultrasound transducer for use with the da Vinci surgical robot, kidney tissue can be better imaged during robot-assisted partial nephrectomy. Accurate 3D ultrasound reconstructions created with the small transducer can be used in future surgical guidance. With the addition of ultrasound elastography to this system, the delineations between healthy and cancerous tissue can be imaged in real-time, allowing for assessment of kidney tumours and more accurate surgical margins.

Ultrasound and ultrasound elastography were then expanded to characterize the tissue of transplant kidneys, where the undetected development of fibrosis can impair function of the graft and shorten its overall life. The kidney is a complicated organ and the work here has provided proof that certain aspects should be taken into consideration during future development of elastography systems for renal tissue.

Bibliography

[1] American cancer society: Cancer facts and figures, 2015. URL https://www.cancer.org/research/cancer-facts-statistics/. [Online; accessed 2016]. → pages 3

[2] J. Abeysekera, R. Rohling, and S. Salcudean. Vibro-elastography: Absolute elasticity from motorized 3d ultrasound measurements of harmonic motion vectors. In *Ultrasonics Symposium (IUS), 2015 IEEE International*, pages 1–4. IEEE, 2015. → pages 94

[3] J. M. Abeysekera. *Three dimensional ultrasound elasticity imaging*. PhD thesis, University of British Columbia, 2016. → pages 13, 55, 94, 102

[4] T. Adebar and *et al*. A robotic system for intra-operative trans-rectal ultrasound and ultrasound elastography in radical prostatectomy. In *Information Processing in Computer-Assisted Interventions*, pages 79–89. Springer, 2011. → pages 58

[5] N. Afsham and *et al*. A generalized correlation-based model for out-of-plane motion estimation in freehand ultrasound. *Medical Imaging, IEEE Transactions on*, 33(1):186–199, 2014. → pages 33

[6] C. Amador, M. W. Urban, J. F. Greenleaf, and L. V. Warner. Measurements of swine renal cortex shear elasticity and viscosity with shearwave dispersion ultrasound vibrometry (sduv). In *2009 IEEE International Ultrasonics Symposium*, pages 491–494. IEEE, 2009. → pages 88, 100

[7] C. Amador, M. W. Urban, L. V. Warner, and J. F. Greenleaf. In vitro renal cortex elasticity and viscosity measurements with shearwave dispersion ultrasound vibrometry (sduv) on swine kidney. In *2009 Annual International Conference of the IEEE Engineering in Medicine and Biology Society*, pages 4428–4431. IEEE, 2009. → pages 88, 100, 112

[8] R. Arndt, S. Schmidt, C. Loddenkemper, M. Grünbaum, W. Zidek, M. Van Der Giet, and T. H. Westhoff. Noninvasive evaluation of renal allograft fibrosis by transient elastography–a pilot study. *Transplant International*, 23(9):871–877, 2010. → pages 79, 80, 81, 89, 118

[9] K. Asano, A. Ogata, K. Tanaka, Y. Ide, A. Sankoda, C. Kawakita, M. Nishikawa, K. Ohmori, M. Kinomura, N. Shimada, et al. Acoustic radiation force impulse elastography of the kidneys is shear wave velocity affected by tissue fibrosis or renal blood flow? *Journal of Ultrasound in Medicine*, 33(5):793–801, 2014. → pages 86, 87, 114

[10] P. Asbach, D. Klatt, U. Hamhaber, J. Braun, R. Somasundaram, B. Hamm, and I. Sack. Assessment of liver viscoelasticity using multifrequency mr elastography. *Magnetic Resonance in Medicine*, 60(2):373–379, 2008. → pages 83

[11] M. Audette, F. Ferrie, and T. Peters. An algorithmic overview of surface registration techniques for medical imaging. *Medical Image Analysis*, 4(3): 201–217, 2000. → pages 38

[12] A. Baghani, A. Brant, S. Salcudean, and R. Rohling. A high-frame-rate ultrasound system for the study of tissue motions. *Ultrasonics, Ferroelectrics and Frequency Control, IEEE Transactions on*, 57(7): 1535–1547, 2010. → pages 14, 16, 58

[13] A. Baghani, S. Salcudean, M. Honarvar, R. Sahebjavaher, R. Rohling, and R. Sinkus. Traveling wave expansion: A model fitting approach to the inverse problem of elasticity reconstruction. *IEEE Medical Imaging*, 30 (99):1–1, 2011. → pages 57, 58, 64, 68

[14] A. Baghani, H. Eskandari, W. Wang, D. Da Costa, M. N. Lathiff, R. Sahebjavaher, S. Salcudean, and R. Rohling. Real-time quantitative elasticity imaging of deep tissue using free-hand conventional ultrasound. In *Medical Image Computing and Computer-Assisted Intervention–MICCAI 2012*, pages 617–624. Springer, 2012. → pages 56, 68, 94, 103

[15] J. R. Banegas, F. Rodríguez-Artalejo, J. J. de la Cruz Troca, P. Guallar-Castillón, and J. del Rey Calero. Blood pressure in spain distribution, awareness, control, and benefits of a reduction in average pressure. *Hypertension*, 32(6):998–1002, 1998. → pages 95

[16] D. Barbot. Improved staging of liver tumors using laparscopic intraoperative ultrasound. *Journal of Surgical Oncology*, 64:63–67, 1997. → pages 20

[17] R. G. Barr, G. Ferraioli, M. L. Palmeri, Z. D. Goodman, G. Garcia-Tsao, J. Rubin, B. Garra, R. P. Myers, S. R. Wilson, D. Rubens, and D. Levine. Elastography assessment of liver fibrosis: Society of radiologists in ultrasound consensus conference statement. *Radiology*, 276(3):845–861, 2015. → pages 139

[18] J. G. Bartlett. *Feature-based registration of preoperative CT to intraoperative 3-D ultrasound in laparoscopic partial nephrectomy using a priori CT segmentation*. PhD thesis, University of British Columbia, 2011. → pages 122

[19] M. A. L. Bell, H. T. Sen, I. Iordachita, and P. Kazanzides. Force-controlled ultrasound robot for consistent tissue pre-loading: Implications for acoustic radiation force elasticity imaging. In *Biomedical Robotics and Biomechatronics (2014 5th IEEE RAS & EMBS International Conference on*, pages 259–264. IEEE, 2014. → pages 71

[20] S. F. Bensamoun, L. Robert, G. E. Leclerc, L. Debernard, and F. Charleux. Stiffness imaging of the kidney and adjacent abdominal tissues measured simultaneously using magnetic resonance elastography. *Clinical imaging*, 35(4):284–287, 2011. → pages 82, 84

[21] J. Bercoff, M. Tanter, and M. Fink. Supersonic shear imaging: a new technique for soft tissue elasticity mapping. *Ultrasonics, Ferroelectrics and Frequency Control, IEEE Transactions on*, 51(4):396–409, 2004. → pages 14, 17

[22] P. Besl and N. McKay. A method for registration of 3-D shapes. *IEEE Transactions on Pattern Analysis and Machine Intelligence*, pages 239–256, 1992. → pages 6, 38

[23] J. Beutel, H. L. Kundel, and R. L. Van Metter. Handbook of medical imaging, volume 1: Physics and psychophysics. 2000. → pages 10

[24] S. Billings, N. Deshmukh, H. Kang, R. Taylor, and E. Boctor. System for robot-assisted real-time laparoscopic ultrasound elastography. In *SPIE Medical Imaging*, 2012. → pages 54

[25] S. Bota, H. Herkner, I. Sporea, P. Salzl, R. Sirli, A. M. Neghina, and M. Peck-Radosavljevic. Meta-analysis: Arfi elastography versus transient elastography for the evaluation of liver fibrosis. *Liver International*, 33(8): 1138–1147, 2013. → pages 74, 78, 85

[26] S. Bota, F. Bob, I. Sporea, R. Şirli, and A. Popescu. Factors that influence kidney shear wave speed assessed by acoustic radiation force impulse elastography in patients without kidney pathology. *Ultrasound in medicine & biology*, 41(1):1–6, 2015. → pages 85

[27] J.-Y. Bouguet. Camera calibration toolbox for matlab. 2004. URL http://www.vision.caltech.edu/bouguetj/calib_doc. → pages 34, 35

[28] R. Budde and *et al*. Endoscopic localization and assessment of coronary arteries by 13MHz epicardial ultrasound. *The Annals of Thoracic Surgery*, 77(5):1586–1592, 2004. → pages 23, 24, 53

[29] R. Budde and *et al*. Robot-assisted 13MHz epicardial ultrasound for endoscopic quality assessment of coronary anastomoses. *Interactive Cardiovascular and Thoracic Surgery*, 3(4):616, 2004. → pages 23, 24

[30] J. Byrn, S. Schluender, C. Divino, J. Conrad, B. Gurland, E. Shlasko, and A. Szold. Three-dimensional imaging improves surgical performance for both novice and experienced operators using the da Vinci Robot System. *The American Journal of Surgery*, 193(4):519–522, 2007. → pages 21

[31] J. Catheline. A comparison of laparoscopic ultrasound versus cholangiography in the evaluation of the biliary tree during laparoscopic cholecystectomy. *European Journal of Ultrasound*, 10(1):1–9, 1999. → pages 20

[32] S.-H. Cha. Comprehensive survey on distance/similarity measures between probability density functions. *Int. J. Math. Models Methods Appl. Sci.*, 4: 300–307, 2007. → pages 38

[33] Z. Chen, A. Deguet, R. Taylor, S. DiMaio, G. Fischer, and P. Kazanzides. An open-source hardware and software platform for telesurgical robotics research. In *Proceedings of the MICCAI Workshop on Systems and Architecture for Computer Assisted Interventions, Nagoya, Japan*, pages 22–26, 2013. → pages 22, 54, 59, 161

[34] P. T. Christopher and K. J. Parker. New approaches to the linear propagation of acoustic fields. *The Journal of the Acoustical Society of America*, 90(1):507–521, 1991. → pages 14

[35] G. Danaei, M. M. Finucane, J. K. Lin, G. M. Singh, C. J. Paciorek, M. J. Cowan, F. Farzadfar, G. A. Stevens, S. S. Lim, L. M. Riley, et al. National, regional, and global trends in systolic blood pressure since 1980: systematic analysis of health examination surveys and epidemiological studies with 786 country-years and 5· 4 million participants. *The Lancet*, 377(9765):568–577, 2011. → pages 95

[36] L. Deane, H. Lee, G. Box, O. Melamud, D. Yee, J. Abraham, D. Finley, J. Borin, E. McDougall, R. Clayman, et al. Robotic versus standard laparoscopic partial/wedge nephrectomy: a comparison of intraoperative and perioperative results from a single institution. *Journal of Endourology*, 22(5):947–952, 2008. → pages 5

[37] M. Desai, I. Gill, A. Ramani, M. Spaliviero, L. Rybicki, and J. Kaouk. The impact of warm ischaemia on renal function after laparoscopic partial nephrectomy. *British Journal of Urology International*, 95(3):377–383, 2005. → pages 5

[38] S. DiMaio and C. Hasser. The da vinci research interface. In *MICCAI Workshop on Systems and Arch. for Computer Assisted Interventions, Midas Journal, Sep*, 2008. → pages 54

[39] S. Ding and *et al*. Tracking of vessels in intra-operative microscope video sequences for cortical displacement estimation. *Biomedical Engineering, IEEE Transactions on*, 58(7):1985–1993, 2011. → pages 6

[40] J. R. Doherty and *et al*. Acoustic radiation force elasticity imaging in diagnostic ultrasound. *Ultrasonics, Ferroelectrics, and Frequency Control, IEEE Transactions on*, 60(4):685–701, 2013. → pages 14, 17, 78

[41] J. R. Doherty, J. J. Dahl, and G. E. Trahey. Harmonic tracking of acoustic radiation force-induced displacements. *IEEE transactions on ultrasonics, ferroelectrics, and frequency control*, 60(11):2347–2358, 2013. → pages 116

[42] P. Edgcumbe and *et al*. Pico lantern: A pick-up projector for augmented reality in laparoscopic surgery. In *Medical Image Computing and Computer-Assisted Intervention–MICCAI 2014*, pages 432–439. Springer, 2014. → pages 26

[43] P. Edgcumbe, C. Nguan, and R. Rohling. Calibration and stereo tracking of a laparoscopic ultrasound transducer for augmented reality in surgery. In *Augmented Reality Environments for Medical Imaging and*

Computer-Assisted Interventions, pages 258–267. Springer, 2013. → pages 34, 40, 47

[44] A. Evans, P. Whelehan, K. Thomson, D. McLean, K. Brauer, C. Purdie, L. Jordan, L. Baker, and A. Thompson. Quantitative shear wave ultrasound elastography: initial experience in solid breast masses. *Breast Cancer Res*, 12(6):R104, 2010. → pages 17

[45] S. Ferguson, J. Bryant, R. Ganz, and K. Ito. The acetabular labrum seal: a poroelastic finite element model. *Clinical Biomechanics*, 15(6):463–468, 2000. → pages 88

[46] M. Feuerstein and *et al*. Magneto-optic tracking of a flexible laparoscopic ultrasound transducer for laparoscope augmentation. In *Medical Image Computing and Computer-Assisted Intervention*, pages 458–466, 2007. → pages 33

[47] K. Fuchs. Minimally invasive surgery. *Endoscopy*, 34(2):154–159, 2002. → pages 19, 32

[48] J. Gao, W. Weitzel, J. M. Rubin, J. Hamilton, J. Lee, D. Dadhania, and R. Min. Renal transplant elasticity ultrasound imaging: correlation between normalized strain and renal cortical fibrosis. *Ultrasound in medicine & biology*, 39(9):1536–1542, 2013. → pages 75, 77

[49] J. Gao, W. He, L.-G. Cheng, X.-Y. Li, X.-R. Zhang, K. Juluru, N. Al Khori, A. Coya, and R. Min. Ultrasound strain elastography in assessment of cortical mechanical behavior in acute renal vein occlusion: in vivo animal model. *Clinical imaging*, 39(4):613–618, 2015. → pages 77, 86

[50] J. Gao, J. M. Rubin, W. Weitzel, J. Lee, D. Dadhania, S. Kapur, and R. Min. Comparison of ultrasound corticomedullary strain with doppler parameters in assessment of renal allograft interstitial fibrosis/tubular atrophy. *Ultrasound in medicine & biology*, 41(10):2631–2639, 2015. → pages 75, 77

[51] A.-S. Garnier and M. Briet. Arterial stiffness and chronic kidney disease. *Pulse*, 3(3-4):229–241, 2016. → pages 87, 89, 137

[52] A. H. Gee and *et al*. Sensorless freehand 3d ultrasound in real tissue: speckle decorrelation without fully developed speckle. *Medical image analysis*, 10(2):137–149, 2006. → pages 33

[53] J.-L. Gennisson and *et al*. Supersonic shear wave elastography of in vivo pig kidney: influence of blood pressure, urinary pressure and tissue anisotropy. *Ultrasound in medicine & biology*, 38(9):1559–1567, 2012. → pages 71, 85, 86

[54] N. Grenier, S. Poulain, S. Lepreux, J.-L. Gennisson, B. Dallaudière, Y. Lebras, E. Bavu, A. Servais, V. Meas-Yedid, M. Piccoli, et al. Quantitative elastography of renal transplants using supersonic shear imaging: a pilot study. *European radiology*, 22(10):2138–2146, 2012. → pages 89, 90

[55] N. Grenier, J.-L. Gennisson, F. Cornelis, Y. Le Bras, and L. Couzi. Renal ultrasound elastography. *Diagnostic and interventional imaging*, 94(5): 545–550, 2013. → pages 74, 78, 79

[56] G. Haber and I. Gill. Laparoscopic partial nephrectomy: Contemporary technique and outcomes. *European urology*, 49(4):660–665, 2006. → pages 19

[57] S. Hariharan, C. P. Johnson, B. A. Bresnahan, S. E. Taranto, M. J. McIntosh, and D. Stablein. Improved graft survival after renal transplantation in the united states, 1988 to 1996. *New England Journal of Medicine*, 342(9):605–612, 2000. → pages 8, 73

[58] W.-Y. He, Y.-J. Jin, W.-P. Wang, C.-L. Li, Z.-B. Ji, and C. Yang. Tissue elasticity quantification by acoustic radiation force impulse for the assessment of renal allograft function. *Ultrasound in medicine & biology*, 40(2):322–329, 2014. → pages 90

[59] O. Helenon, S. Merran, F. Paraf, P. Melki, J.-M. Correas, Y. Chretien, and J.-F. Moreau. Unusual fat-containing tumors of the kidney: a diagnostic dilemma. *Radiographics*, 17(1):129–144, 1997. → pages 29

[60] O. Helenon, J. Correas, C. Balleyguier, M. Ghouadni, and F. Cornud. Ultrasound of renal tumors. *European radiology*, 11(10):1890–1901, 2001. → pages 29

[61] C. Helfenstein, J.-L. Gennisson, M. Tanter, and P. Beillas. Effects of pressure on the shear modulus, mass and thickness of the perfused porcine kidney. *Journal of biomechanics*, 48(1):30–37, 2015. → pages 86, 87, 90, 113, 132

[62] C. R. Hill, J. C. Bamber, and G. ter Haar. *Physical principles of medical ultrasonics*, volume 2. Wiley Online Library, 2004. → pages 10

[63] M. Honarvar. *Dynamic elastography with finite element-based inversion*. PhD thesis, University of British Columbia, 2015. → pages 103, 110

[64] M. Honarvar and *et al*. Direct vibro-elastography fem inversion in cartesian and cylindrical coordinate systems without the local homogeneity assumption. *Physics in medicine and biology*, 60(9):3847, 2015. → pages 94

[65] B. K. Horn, H. M. Hilden, and S. Negahdaripour. Closed-form solution of absolute orientation using orthonormal matrices. *JOSA A*, 5(7):1127–1135, 1988. → pages 164

[66] M. M. Hossain, M. Selzo, R. Hinson, L. Baggessen, R. Detwiler, W. Chong, L. Brubaker, M. Caughey, M. Fisher, S. Whitehead, et al. Evaluation of renal transplant status using viscoelastic response (visr) ultrasound: A pilot clinical study. In *Ultrasonics Symposium (IUS), 2016 IEEE International*, pages 1–4. IEEE, 2016. → pages 88, 100

[67] Q. Hu, X.-Y. Wang, H.-G. He, H.-M. Wei, L.-K. Kang, and G.-C. Qin. Acoustic radiation force impulse imaging for non-invasive assessment of renal histopathology in chronic kidney disease. *PloS one*, 9(12):e115051, 2014. → pages 89

[68] G. Hubens, H. Coveliers, L. Balliu, M. Ruppert, and W. Vaneerdeweg. A performance study comparing manual and robotically assisted laparoscopic surgery using the da Vinci system. *Surgical Endoscopy*, 17(10):1595–1599, 2003. → pages 21, 52

[69] S. Hughes and *et al*. Volume estimation from multiplanar 2D ultrasound images using a remote electromagnetic position and orientation sensor. *Ultrasound in Medicine & Biology*, 22(5):561–572, 1996. ISSN 0301-5629. → pages 34

[70] A. Hughes-Hallett, E. K. Mayer, H. J. Marcus, T. P. Cundy, P. J. Pratt, A. W. Darzi, and J. A. Vale. Augmented reality partial nephrectomy: examining the current status and future perspectives. *Urology*, 83(2): 266–273, 2014. → pages 137, 161

[71] L. Huwart and *et al.* Liver fibrosis: non-invasive assessment with mr elastography. *NMR in Biomedicine*, 19(2):173–179, 2006. → pages 71

[72] L. Huwart and *et al*. Comparison of mr elastography and fibroscan for the non-invasive assessment of liver fibrosis. In *Joint Annual Meeting ISMRM-ESMRMB*, number EPFL-CONF-188693, 2007. → pages 18, 71

[73] V. Jha, G. Garcia-Garcia, K. Iseki, Z. Li, S. Naicker, B. Plattner, R. Saran, A. Y.-M. Wang, and C.-W. Yang. Chronic kidney disease: global dimension and perspectives. *The Lancet*, 382(9888):260–272, 2013. → pages 8

[74] J. Jomier and S. Aylward. Rigid and deformable vasculature-to-image registration: A hierarchical approach. *Medical Image Computing and Computer-Assisted Intervention*, pages 829–836, 2004. → pages 6

[75] M. Jung, P. Morel, L. Buehler, N. Buchs, and M. Hagen. Robotic general surgery: current practice, evidence, and perspective. *Langenbeck's Archives of Surgery*, pages 1–10, 2015. → pages 161

[76] J. Kahn, T. Slowinski, A. Thomas, S. Filimonow, and T. Fischer. Tsi ultrasound elastography for the diagnosis of chronic allograft nephropathy in kidney transplanted patients. *Journal of Ultrasonography*, 13(54):253, 2013. → pages 75, 77

[77] S. Kaul, R. Laungani, R. Sarle, H. Stricker, J. Peabody, R. Littleton, and M. Menon. da Vinci-assisted robotic partial nephrectomy: Technique and results at a mean of 15 months of follow-up. *European Urology*, 51(1): 186–192, 2007. → pages 19

[78] L. Kavan and *et al*. Dual quaternions for rigid transformation blending. *Trinity College Dublin, Tech. Rep. TCD-CS-2006-46*, 2006. → pages 60, 166

[79] P. Kazanzides, Z. Chen, A. Deguet, G. Fischer, R. Taylor, and S. DiMaio. An open-source research kit for the da vinci r surgical robot. In *Proc. IEEE International Conf. on Robotics and Automation (ICRA14)*, 2014. → pages 22, 54, 59, 161

[80] V. Kindratenko. A survey of electromagnetic position tracker calibration techniques. *Virtual Reality*, 5(3):169–182, 2000. → pages 49

[81] H. Knutsson, C.-F. Westin, and G. Granlund. Local multiscale frequency and bandwidth estimation. In *Image Processing, 1994. Proceedings. ICIP-94., IEEE International Conference*, volume 1, pages 36–40. IEEE, 1994. → pages 61

[82] B. Koeppen and B. Stanton. *Renal Physiology*. Elsevier Mosby, Philadelphia, 5th edition, 2013. → pages 2, 86, 114

[83] K. Konishi and *et al*. A real-time navigation system for laparoscopic surgery based on three-dimensional ultrasound using magneto-optic hybrid tracking configuration. *International Journal of Computer Assisted Radiology and Surgery*, 2(1):1–10, 2007. → pages 33

[84] E. E. Konofagou, T. P. Harrigan, J. Ophir, and T. A. Krouskop. Poroelastography: imaging the poroelastic properties of tissues. *Ultrasound in medicine & biology*, 27(10):1387–1397, 2001. → pages 29, 115

[85] M. J. Korsmo, B. Ebrahimi, A. Eirin, J. R. Woollard, J. D. Krier, J. A. Crane, L. Warner, K. Glaser, R. Grimm, R. L. Ehman, et al. Magnetic resonance elastography noninvasively detects in-vivo renal medullary fibrosis secondary to swine renal artery stenosis. *Investigative radiology*, 48(2):61, 2013. → pages 83, 84, 86

[86] T. A. Krouskop, T. M. Wheeler, F. Kallel, B. S. Garra, and T. Hall. Elastic moduli of breast and prostate tissues under compression. *Ultrasonic imaging*, 20(4):260–274, 1998. → pages 22, 29

[87] S. Kruse, M. Dresner, and R. Ehman. Mr elastography of human kidney in vivo: a feasibility study. In *Proceedings of the 12th Annual Meeting of the International Society for Magnetic Resonance in Medicine, Kyoto, Japan*, page 2600, 2004. → pages 82

[88] C. Kut, C. Schneider, N. Carter-Monroe, L.-M. Su, E. Boctor, and R. Taylor. Accuracy of localization of prostate lesions using manual palpation and ultrasound elastography. In *SPIE Medical Imaging*, pages 726128–726128. International Society for Optics and Photonics, 2009. → pages 22

[89] D. Kwartowitz, S. Herrell, and R. Galloway. Toward image-guided robotic surgery: Determining intrinsic accuracy of the da Vinci robot. *International Journal of Computer Assisted Radiology and Surgery*, 1(3): 157–165, 2006. → pages 22, 34, 69, 161, 166

[90] D. M. Kwartowitz, S. D. Herrell, and R. L. Galloway. Update: Toward image-guided robotic surgery: determining the intrinsic accuracy of the davinci-s robot. *International Journal of Computer Assisted Radiology and Surgery*, 1(5):301–304, 2007. → pages 166

[91] J. S. Lam, J. Bergman, A. Breda, and P. G. Schulam. Importance of surgical margins in the management of renal cell carcinoma. *Nature clinical practice Urology*, 5(6):308–317, 2008. → pages 29

[92] T. Lange and *et al*. Augmenting intraoperative 3D ultrasound with preoperative models for navigation in liver surgery. *Medical Image Computing and Computer-Assisted Intervention*, pages 534–541, 2004. → pages 6

[93] T. Lange and *et al*. 3d ultrasound-ct registration of the liver using combined landmark-intensity information. *International journal of computer assisted radiology and surgery*, 4(1):79–88, 2009. → pages 6

[94] A. Lasso and *et al*. Plus: open-source toolkit for ultrasound-guided intervention systems. *IEEE Trans Biomed Eng*, May 2014. doi:10.1109/TBME.2014.2322864. URL http://dx.doi.org/10.1109/TBME.2014.2322864. → pages 35

[95] A. Lasso, T. Heffter, C. Pinter, T. Ungi, T. K. Chen, A. Boucharin, and G. Fichtinger. Plus: An open-source toolkit for developing ultrasound-guided intervention systems. In *4th Image Guided Therapy Workshop*, volume 4, page 103, 2011. → pages 56, 60

[96] W. K. Lau, M. L. Blute, A. L. Weaver, V. E. Torres, and H. Zincke. Matched comparison of radical nephrectomy vs nephron-sparing surgery in patients with unilateral renal cell carcinoma and a normal contralateral kidney. In *Mayo Clinic Proceedings*, volume 75, pages 1236–1242. Elsevier, 2000. → pages 4

[97] C. U. Lee, J. F. Glockner, K. J. Glaser, M. Yin, J. Chen, A. Kawashima, B. Kim, W. K. Kremers, R. L. Ehman, and J. M. Gloor. Mr elastography in renal transplant patients and correlation with renal allograft biopsy: a feasibility study. *Academic radiology*, 19(7):834–841, 2012. → pages 84

[98] D. Lee and *et al*. Non-rigid registration between 3d ultrasound and ct images of the liver based on intensity and gradient information. *Physics in medicine and biology*, 56(1):117, 2011. → pages 6

[99] G. Lee, M. Lee, I. Green, M. Allaf, and M. Marohn. Surgeons physical discomfort and symptoms during robotic surgery: a comprehensive ergonomic survey study. *Surgical Endoscopy*, pages 1–10, 2016. → pages 19

[100] J. Leven and *et al*. da Vinci canvas: A telerobotic surgical system with integrated, robot-assisted, laparoscopic ultrasound capability. *Medical Image Computing and Computer-Assisted Intervention*, pages 811–818, 2005. → pages 23

[101] R. Link, S. Bhayani, and L. Kavoussi. A prospective comparison of robotic and laparoscopic pyeloplasty. *Annals of Surgery*, 243(4):486, 2006. → pages 22

[102] G. Low, N. E. Owen, I. Joubert, A. J. Patterson, M. J. Graves, K. J. Glaser, G. J. Alexander, and D. J. Lomas. Reliability of magnetic resonance elastography using multislice two-dimensional spin-echo echo-planar imaging (se-epi) and three-dimensional inversion reconstruction for assessing renal stiffness. *Journal of Magnetic Resonance Imaging*, 42(3): 844–850, 2015. → pages 82, 84

[103] V. Lukenda, I. Mikolasevic, S. Racki, I. Jelic, D. Stimac, and L. Orlic. Transient elastography: a new noninvasive diagnostic tool for assessment of chronic allograft nephropathy. *International urology and nephrology*, 46 (7):1435–1440, 2014. → pages 80, 81, 118

[104] M. Makuuchi, G. Torzilli, and J. Machi. History of intraoperative ultrasound. *Ultrasound in Medicine & Biology*, 24(9):1229–1242, 1998. → pages 20

[105] A. Manduca, R. Muthupillai, P. Rossman, J. Greenleaf, and R. Ehman. Local wavelength estimation for magnetic resonance elastography. In *International Conference on Image Processing*, volume 3, pages 527–530. IEEE, 1996. → pages 15, 94, 123, 137

[106] Y. K. Mariappan, K. J. Glaser, and R. L. Ehman. Magnetic resonance elastography: a review. *Clinical anatomy*, 23(5):497–511, 2010. → pages 18, 82

[107] A. J. Matas, J. M. Smith, M. A. Skeans, B. Thompson, S. K. Gustafson, D. E. Stewart, W. S. Cherikh, J. L. Wainright, G. Boyle, J. J. Snyder, A. K. Israni, and B. L. Kasiske. Optn/srtr 2013 annual data report: Kidney. *American Journal of Transplantation*, 15(S2):1–34, 2015. ISSN 1600-6143. doi:10.1111/ajt.13195. URL http://dx.doi.org/10.1111/ajt.13195. → pages 8

[108] S. McKinley, A. Garg, S. Sen, R. Kapadia, A. Murali, K. Nichols, S. Lim, S. Patil, P. Abbeel, A. M. Okamura, et al. A single-use haptic palpation probe for locating subcutaneous blood vessels in robot-assisted minimally invasive surgery. In *Automation Science and Engineering (CASE), 2015 IEEE International Conference on*, pages 1151–1158. IEEE, 2015. → pages 53

[109] A. L. McKnight, J. L. Kugel, P. J. Rossman, A. Manduca, L. C. Hartmann, and R. L. Ehman. Mr elastography of breast cancer: preliminary results. *American journal of roentgenology*, 178(6):1411–1417, 2002. → pages 22

[110] M. Mengel, J. Chapman, F. G. Cosio, M. Cavaillé-Coll, H. Haller, P. Halloran, A. Kirk, M. Mihatsch, B. Nankivell, L. Racusen, et al. Protocol biopsies in renal transplantation: insights into patient management and pathogenesis. *American Journal of Transplantation*, 7(3):512–517, 2007. → pages 9, 74

[111] M. S. Menzilcioglu, M. Duymus, S. Citil, G. Gungor, M. Saglam, O. Gungor, S. N. Boysan, A. Sarıca, and S. Avcu. The comparison of resistivity index and strain index values in the ultrasonographic evaluation of chronic kidney disease. *La radiologia medica*, pages 1–7, 2016. → pages 75, 77

[112] L. Mercier and *et al*. A review of calibration techniques for freehand 3-D ultrasound systems. *Ultrasound in Medicine & Biology*, 31(2):143–165, 2005. ISSN 0301-5629. → pages 35

[113] O. Mohareri, A. Ruszkowski, J. Lobo, J. Ischia, A. Baghani, G. Nir, H. Eskandari, E. Jones, L. Fazli, L. Goldenberg, et al. Multi-parametric 3d quantitative ultrasound vibro-elastography imaging for detecting palpable prostate tumors. In *International Conference on Medical Image Computing and Computer-Assisted Intervention*, pages 561–568. Springer, 2014. → pages 94, 103

[114] O. Mohareri, C. Schneider, and S. Salcudean. Bimanual telerobotic surgery with asymmetric force feedback: A davinci® surgical system implementation. In *Intelligent Robots and Systems (IROS 2014), 2014 IEEE/RSJ International Conference on*, pages 4272–4277. IEEE, 2014. → pages 53, 161

[115] T. Nakao, H. Ushigome, T. Nakamura, S. Harada, K. Koshino, T. Suzuki, T. Ito, S. Nobori, and N. Yoshimura. Evaluation of renal allograft fibrosis by transient elastography (fibro scan). In *Transplantation proceedings*, volume 47, pages 640–643. Elsevier, 2015. → pages 80, 81, 118

[116] B. J. Nankivell, R. J. Borrows, C. L.-S. Fung, P. J. OConnell, R. D. Allen, and J. R. Chapman. Natural history, risk factors, and impact of subclinical rejection in kidney transplantation. *Transplantation*, 78(2):242–249, 2004. → pages 9, 73

[117] K. Nightingale, M. Soo, R. Nightingale, and G. Trahey. Acoustic radiation force impulse imaging: in vivo demonstration of clinical feasibility. *Ultrasound in medicine & biology*, 28(2):227–235, 2002. → pages 17

[118] K. R. Nightingale, M. L. Palmeri, R. W. Nightingale, and G. E. Trahey. On the feasibility of remote palpation using acoustic radiation force. *The Journal of the Acoustical Society of America*, 110(1):625–634, 2001. → pages 14, 17

[119] U. of Utah Kidney Transplant Program. Kidney transplant, 2016. URL http://healthcare.utah.edu/transplant/kidney/. [Online; accessed Dec 12th 2016]. → pages xii, 7

[120] A. M. Okamura. Methods for haptic feedback in teleoperated robot-assisted surgery. *Industrial Robot: An International Journal*, 31(6): 499–508, 2004. → pages 53

[121] A. M. Okamura, L. N. Verner, C. Reiley, and M. Mahvash. Haptics for robot-assisted minimally invasive surgery. In *Robotics research*, pages 361–372. Springer, 2011. → pages 53

[122] A. OpenStax College and P. O. CNX. Anatomy and physiology, 2016. URL http://cnx.org/contents/14fb4ad7-39a1-4eee-ab6e-3ef2482e3e22@8.26. [Online; accessed Dec 12th 2016]. → pages xii, 3

[123] J. Ophir, I. Cespedes, H. Ponnekanti, Y. Yazdi, and X. Li. Elastography: a quantitative method for imaging the elasticity of biological tissues. *Ultrasonic imaging*, 13(2):111–134, 1991. → pages 54

[124] E. M. V. Osorio and *et al*. Accurate ct/mr vessel-guided nonrigid registration of largely deformed livers. *Medical physics*, 39(5):2463–2477, 2012. → pages 6

[125] F. Ozkan, Y. C. Yavuz, M. F. Inci, B. Altunoluk, N. Ozcan, M. Yuksel, H. Sayarlioglu, and E. Dogan. Interobserver variability of ultrasound elastography in transplant kidneys: correlations with clinical-doppler parameters. *Ultrasound in medicine & biology*, 39(1):4–9, 2013. → pages 75, 76, 77

[126] M. L. Palmeri, Y. Deng, N. C. Rouze, and K. R. Nightingale. Dependence of shear wave spectral content on acoustic radiation force excitation duration and spatial beamwidth. In *2014 IEEE International Ultrasonics Symposium*, pages 1105–1108. IEEE, 2014. → pages 116

[127] G. Penney and *et al*. Registration of freehand 3D ultrasound and magnetic resonance liver images. *Medical Image Analysis*, 8(1):81–91, 2004. ISSN 1361-8415. → pages 6

[128] P. R. Perriñez, F. E. Kennedy, E. E. Van Houten, J. B. Weaver, and K. D. Paulsen. Modeling of soft poroelastic tissue in time-harmonic mr elastography. *IEEE transactions on biomedical engineering*, 56(3): 598–608, 2009. → pages 88

[129] T. Polascik and *et al*. Intraoperative sonography for the evaluation and management of renal tumors: Experience with 100 patients. *The Journal of Urology*, 154(5):1676–1680, 1995. → pages 20

[130] F. Porpiglia, A. Volpe, M. Billia, and R. Scarpa. Laparoscopic versus open partial nephrectomy: analysis of the current literature. *European Urology*, 53(4):732–743, 2008. → pages 4, 19

[131] F. K. Port, R. A. Wolfe, E. A. Mauger, D. P. Berling, and K. Jiang. Comparison of survival probabilities for dialysis patients vs cadaveric renal transplant recipients. *Jama*, 270(11):1339–1343, 1993. → pages 73, 117

[132] R. Prager and *et al*. Rapid calibration for 3-D freehand ultrasound. *Ultrasound in Medicine & Biology*, 24(6):855–869, 1998. → pages 35, 56

[133] P. Pratt and *et al*. Intraoperative ultrasound guidance for transanal endoscopic microsurgery. In *Medical Image Computing and Computer-Assisted Intervention–MICCAI 2012*, pages 463–470. Springer, 2012. → pages 33, 35

[134] D. N. Reddan, G. V. Raj, and T. J. Polascik. Management of small renal tumors: an overview. *The American journal of medicine*, 110(7):558–562, 2001. → pages 6

[135] D. M. T. Reece. Kidney physiology basics, 2016. URL http://www.medicalsciencenavigator.com/page/4/. [Online; accessed Dec 12th 2016]. → pages xii, 4

[136] I. Reinertsen and *et al*. Validation of vessel-based registration for correction of brain shift. *Medical Image Analysis*, 11(4):374–388, 2007. → pages 6

[137] T. Robinson and G. Stiegmann. Minimally invasive surgery. *Endoscopy*, 36 (1):48–51, 2004. → pages 19, 32

[138] R. Rohling and *et al*. Comparison of relative accuracy between a mechanical and an optical position tracker for image-guided neurosurgery. *Computer Aided Surgery*, 1(1):30–34, 1995. → pages 37, 162

[139] O. Rouvière, R. Souchon, G. Pagnoux, J.-M. Ménager, and J.-Y. Chapelon. Magnetic resonance elastography of the kidneys: feasibility and reproducibility in young healthy adults. *Journal of Magnetic Resonance Imaging*, 34(4):880–886, 2011. → pages 82, 84

[140] A. Ruszkowski, O. Mohareri, S. Lichtenstein, R. Cook, and S. Salcudean. On the feasibility of heart motion compensation on the da vinci surgical robot for coronary artery bypass surgery: Implementation and user studies. In *Proc. IEEE International Conf. on Robotics and Automation*, pages 4432–4439, 2015. → pages 161

[141] J. Schiff, M. Palese, E. Vaughan Jr, R. Sosa, D. Coll, and J. Del Pizzo. Laparoscopic vs open partial nephrectomy in consecutive patients: The cornell experience. *British Journal of Urology International*, 96(6): 811–814, 2005. → pages 19

[142] C. Schneider and *et al*. Robot-assisted laparoscopic ultrasound. *Information Processing in Computer-Assisted Interventions*, pages 67–80, 2010. → pages 23, 33

[143] C. Schneider and *et al*. Intra-operative "pick-up ultrasound for robot assisted surgery with vessel extraction and registration: A feasibility study. *Information Processing in Computer-Assisted Interventions*, pages 122–132, 2011. → pages xiv, 6, 20, 24, 33, 53, 54, 58, 59

[144] C. Schneider, A. Baghani, R. Rohling, and S. Salcudean. Remote ultrasound palpation for robotic interventions using absolute elastography. In *Medical Image Computing and Computer-Assisted Intervention–MICCAI 2012*, pages 42–49. Springer, 2012. → pages 52, 98

[145] C. Schneider, M. Honarvar, R. Rohling, S. Salcudean, and C. Nguan. Apparatus for imaging and model fitting of *ex-vivo* porcine kidney. In *Fifteenth International Tissue Elasticity Conference*. ITEC, 2016. → pages 93

[146] C. Schneider, J. Lobo, M. Honarvar, S. Bidur, R. Rohling, and S. Salcudean. Blood pressure dependent elasticity measurements of porcine kidney *ex-vivo*. In *2016 IEEE International Ultrasonics Symposium*. IEEE, 2016. → pages 93

[147] C. Schneider, C. Nguan, R. Rohling, and S. Salcudean. Tracked pick-up ultrasound for robot-assisted minimally invasive surgery. *IEEE Transactions on Biomedical Engineering*, 63(2):260–268, 2016. → pages 32, 58

[148] C. M. Schneider, S. E. Salcudean, R. N. Rohling, and C. Y. C. Nguan. Ultrasound probe for laparoscopy, 2012. US Patent App. 13/525,183. → pages 26

[149] A. Schwarz, W. Gwinner, M. Hiss, J. Radermacher, M. Mengel, and H. Haller. Safety and adequacy of renal transplant protocol biopsies. *American journal of transplantation*, 5(8):1992–1996, 2005. → pages 8, 73, 117

[150] A. Schwarz, M. Mengel, W. Gwinner, J. Radermacher, M. Hiss, H. Kreipe, and H. Haller. Risk factors for chronic allograft nephropathy after renal transplantation: a protocol biopsy study. *Kidney international*, 67(1): 341–348, 2005. → pages 8, 9, 73

[151] M. R. Selzo and C. M. Gallippi. Viscoelastic response (visr) imaging for assessment of viscoelasticity in voigt materials. *IEEE transactions on ultrasonics, ferroelectrics, and frequency control*, 60(12):2488–2500, 2013. → pages 88, 100

[152] M. Shah. Solving the robot-world/hand-eye calibration problem using the kronecker product. *Journal of Mechanisms and Robotics*, 5(3): 031007(1–7), 2013. → pages 36

[153] T. Sielhorst, M. Feuerstein, and N. Navab. Advanced medical displays: A literature review of augmented reality. *Journal of Display Technology*, 4 (4):451–467, 2008. → pages 137

[154] R. Sinkus and *et al*. Mr elastography of breast lesions: understanding the solid/liquid duality can improve the specificity of contrast-enhanced mr mammography. *Magnetic Resonance in Medicine*, 58(6):1135–1144, 2007. → pages 18, 29, 71

[155] K. Solez et al. International standardization of criteria for the histologic diagnosis of renal allograft rejection: the banff working classification of kidney transplant pathology. *Kidney international*, 44(2):411–422, 1993. → pages 9, 79, 118

[156] C. Sommerer, M. Scharf, C. Seitz, G. Millonig, H. K. Seitz, M. Zeier, and S. Mueller. Assessment of renal allograft fibrosis by transient elastography. *Transplant International*, 26(5):545–551, 2013. → pages 79, 81, 90

[157] M. Spaliviero and I. Gill. Laparoscopic partial nephrectomy. *British Journal of Urology International*, 99(5b):1313–1328, 2007. → pages 4, 32

[158] P. Stolka, M. Keil, G. Sakas, E. McVeigh, M. Allaf, R. Taylor, and E. Boctor. A 3D-elastography-guided system for laparoscopic partial nephrectomies. In *SPIE Medical Imaging*, 2010. → pages 54

[159] D. Stoyanov, G. Mylonas, F. Deligianni, A. Darzi, and G. Yang. Soft-tissue motion tracking and structure estimation for robotic assisted MIS procedures. *Medical Image Computing and Computer-Assisted Intervention*, pages 139–146, 2005. → pages 22

[160] K.-J. Streitberger, J. Guo, H. Tzschätzsch, S. Hirsch, T. Fischer, J. Braun, and I. Sack. High-resolution mechanical imaging of the kidney. *Journal of biomechanics*, 47(3):639–644, 2014. → pages 84

[161] S. E. Sutherland, M. I. Resnick, G. T. Maclennan, and H. B. Goldman. Does the size of the surgical margin in partial nephrectomy for renal cell cancer really matter? *The Journal of urology*, 167(1):61–64, 2002. → pages 6

[162] T. Syversveen, K. Brabrand, K. Midtvedt, E. H. Strøm, A. Hartmann, J. A. Jakobsen, and A. E. Berstad. Assessment of renal allograft fibrosis by acoustic radiation force impulse quantification–a pilot study. *Transplant International*, 24(1):100–105, 2011. → pages 89

[163] T. Syversveen, K. Midtvedt, A. E. Berstad, K. Brabrand, E. H. Strøm, and A. Abildgaard. Tissue elasticity estimated by acoustic radiation force impulse quantification depends on the applied transducer force: an experimental study in kidney transplant patients. *European radiology*, 22 (10):2130–2137, 2012. → pages 88, 94, 113

[164] T. L. Szabo. *Diagnostic ultrasound imaging: inside out*. Academic Press, 2004. → pages 13

[165] A. Talasaz and R. V. Patel. Integration of force reflection with tactile sensing for minimally invasive robotics-assisted tumor localization. *IEEE Transactions on Haptics*, 6(2):217–228, 2013. → pages 53

[166] A. Talasaz, A. L. Trejos, S. Perreault, H. Bassan, and R. V. Patel. A dual-arm 7-degrees-of-freedom haptics-enabled teleoperation test bed for minimally invasive surgery. *Journal of Medical Devices*, 8(4):041004, 2014. → pages 53

[167] L. Taylor, B. Porter, D. Rubens, and K. Parker. Three-dimensional sonoelastography: principles and practices. *Physics in medicine and biology*, 45(6):1477, 2000. → pages 18

[168] R. Ternifi, J.-L. Gennisson, M. Tanter, and P. Beillas. Effects of storage temperature on the mechanical properties of porcine kidney estimated using shear wave elastography. *Journal of the mechanical behavior of biomedical materials*, 28:86–93, 2013. → pages 90, 95

[169] R. H. Thompson, B. R. Lane, C. M. Lohse, B. C. Leibovich, A. Fergany, I. Frank, I. S. Gill, M. L. Blute, and S. C. Campbell. Every minute counts when the renal hilum is clamped during partial nephrectomy. *European urology*, 58(3):340–345, 2010. → pages 5

[170] S. Thompson, M. James, N. Wiebe, B. Hemmelgarn, B. Manns, S. Klarenbach, M. Tonelli, A. K. D. Network, et al. Cause of death in patients with reduced kidney function. *Journal of the American Society of Nephrology*, pages ASN–2014070714, 2015. → pages 73

[171] G. Treece, R. Prager, and A. Gee. Regularised marching tetrahedra: improved iso-surface extraction. *Computers & Graphics*, 23(4):583–598, 1999. → pages 38

[172] M. Urban, S. Chen, and M. Fatemi. A review of shearwave dispersion ultrasound vibrometry (sduv) and its applications. *Current medical imaging reviews*, 8(1):27–36, 2012. → pages 88, 100

[173] M. Van Veelen, E. Nederlof, R. Goossens, C. Schot, and J. Jakimowicz. Ergonomic problems encountered by the medical team related to products used for minimally invasive surgery. *Surgical Endoscopy*, 17(7): 1077–1081, 2003. → pages 19

[174] C. Våpenstad and *et al*. Laparoscopic ultrasound: A survey of its current and future use, requirements, and integration with navigation technology. *Surgical Endoscopy*, pages 1–10, 2010. → pages 20

[175] D. Wang, F. Bello, and A. Darzi. Augmented reality provision in robotically assisted minimally invasive surgery. In *International Congress Series*, volume 1268, pages 527–532, 2004. → pages 22

[176] L. Wang, P. Xia, K. Lv, J. Han, Q. Dai, X.-m. Li, L.-m. Chen, and Y.-x. Jiang. Assessment of renal tissue elasticity by acoustic radiation force impulse quantification with histopathological correlation: preliminary experience in chronic kidney disease. *European radiology*, 24(7): 1694–1699, 2014. → pages 89

[177] L. Warner, M. Yin, K. J. Glaser, J. A. Woollard, C. A. Carrascal, M. J. Korsmo, J. A. Crane, R. L. Ehman, and L. O. Lerman. Noninvasive in vivo assessment of renal tissue elasticity during graded renal ischemia using mr elastography. *Investigative radiology*, 46(8):509, 2011. → pages 83, 84, 86

[178] W. F. Weitzel, K. Kim, J. M. Rubin, R. C. Wiggins, H. Xie, X. Chen, S. Y. Emelianov, and M. O'DONNELL. Feasibility of applying ultrasound strain imaging to detect renal transplant chronic allograft nephropathy. *Kidney international*, 65(2):733–736, 2004. → pages 77

[179] R. Yakoubi, R. Autorino, H. Laydner, J. Guillotreau, M. A. White, S. Hillyer, G. Spana, R. Khanna, W. Isaac, G.-P. Haber, et al. Initial laboratory experience with a novel ultrasound probe for standard and single-port robotic kidney surgery: increasing console surgeon autonomy and minimizing instrument clashing. *The International Journal of Medical Robotics and Computer Assisted Surgery*, 8(2):201–205, 2012. → pages 53

[180] T. Yamamoto, B. Vagvolgyi, K. Balaji, L. L. Whitcomb, and A. M. Okamura. Tissue property estimation and graphical display for teleoperated robot-assisted surgery. In *Robotics and Automation, 2009. ICRA'09. IEEE International Conference on*, pages 4239–4245. IEEE, 2009. → pages 53

[181] M. Yin and *et al*. Assessment of hepatic fibrosis with magnetic resonance elastography. *Clinical Gastroenterology and Hepatology*, 5(10): 1207–1213, 2007. → pages 71

[182] M. Yin, L. Warner, L. Lerman, A. Manduca, and R. Ehman. Assessment of kidney stiffness in a swine model of renal arterial stenosis with 3-d mr elastography. *Proceedings of the International Society for Magnetic Resonance in Medicine. April 18Y24*, 2009. → pages 84, 86, 87

[183] M. Yin, K. Glaser, A. Kolipaka, L. Warner, J. Talwalkar, A. Manduca, and R. Ehman. Influence of perfusion on tissue stiffness assessed with mr elastography. In *Proceedings of the International Society for Magnetic Resonance in Medicine*, volume 18, 2010. → pages 84, 86, 87

[184] P. Yohannes, P. Rotariu, P. Pinto, A. Smith, and B. Lee. Comparison of robotic versus laparoscopic skills: Is there a difference in the learning curve? *Urology*, 60(1):39–45, 2002. → pages 21

[185] M. Zaffanello and C. Bruno. Clinical perspective on renal elasticity quantification by acoustic radiation force. *World Journal of Clinical Urology*, 4(3):100–103, 2015. → pages 78

[186] M. Zaffanello, G. Piacentini, C. Bruno, M. Brugnara, and V. Fanos. Renal elasticity quantification by acoustic radiation force impulse applied to the evaluation of kidney diseases. *Journal of Investigative Medicine*, 63(4): 605–612, 2015. → pages 78

[187] R. Zahiri-Azar and S. Salcudean. Motion estimation in ultrasound images using time domain cross correlation with prior estimates. *Biomedical Engineering, IEEE Transactions on*, 53(10):1990–2000, 2006. → pages 18, 60

Appendix A

Supporting Materials

A.1 dVRK and its Accuracy

The DVRK [75] controllers are an "open source mechatronics platform consisting of hardware, firmware and software components [33], [79] and are being installed at multiple centers for telerobotics in medicine research. With the expansion of the use of these controllers and software, is imperative to understand the accuracy and precision of the system as compared to the da Vinci classic and S (and Si) systems that are used clinically. Previously, Kwartowitz *et. al* has investigated the accuracy and precision of the clinical API associated with the da Vinci classic and S robots [89].

These controllers are being used to implement new haptic interfaces [114] and even an implementation of a control system to compensate for the motion of a beating heart [140]. Future research could also include augmented reality [70]. Each of these applications requires that the location of the tools be known accurately in the framework of the robot.

In our lab, the teleoperation system is based on the components from the open source CISST/SAW libraries [33], a common implementation for the controllers. The controllers are implemented using a da Vinci Classic robot.

In these experiments, the Certus OptoTrak was used to validate the dVRK position. The OptoTrak Certus Motion Capture System (Northern Digital Inc., Ontario, Canada), a tracking system that uses active IR LEDs has an accuracy of 0.1 mm

and resolution of 0.01 mm over its working volume [138]. An OptoTrak stylus was used to localize the points in the OptoTrak frame. The position of the robot tool control point is reported by the dVRK with respect to the base of the activated joints of the arm.

Legos were used to create a repeatable and stable platform for the target localization. A custom Lego was designed and 3D printed for these experiments. The custom Lego was designed to have a semi circle hole for the OptoTrak stylus tip, 3mm in diameter, and a divot, 1mm $\times$ 1.5mm to fit the tip of the Black Diamond Mirco Forceps^{TM}, the da Vinci tool used in this experiment. The tool was chosen for its very small tip which can be the most accurately localized. Because the dVRK reports the control point of the tool, discussed later, other, similar tools are expected to have the same accuracy results, given that the tip offset is known or calibrated.

The difference in position between the dVRK divot point and the OptoTrak pivot point needs to be corrected using the known geometry of the custom built Lego. A coordinate frame was defined for the Lego blocks using the axis of the Lego locations ($Lego$). The OptoTrak points ($Opto_{points}$) were transformed into the Lego frame and the difference in positions between the dVRK and the OptoTrak ($Lego_{offset}$) were then applied to the OptoTrak positions. The transformed OptoTrak points were then transformed back into their original coordinate frame. The positions of the dVRK and OptoTrak are then correlated.

$$O = ((Lego * Opto_{points}) * Lego_{offset}) * (Lego^{-1})$$

Another offset must be applied in order to locate the tip of the tool exactly. The tool location, or control point, as defined by the dVRK is not located at the tip of the tool, but near the base of the jaws [Figure A.2]. The offset between the control point and the tool tip is known from the tool geometry. Each position reported by the dVRK ($Reported$) is multiplied by this offset to find the 3D location of the actual tool tip.

$$dVRKpoints = Reported * Tool_{offset}$$

The custom Lego was placed in 36 locations in a rectangle with dimensions

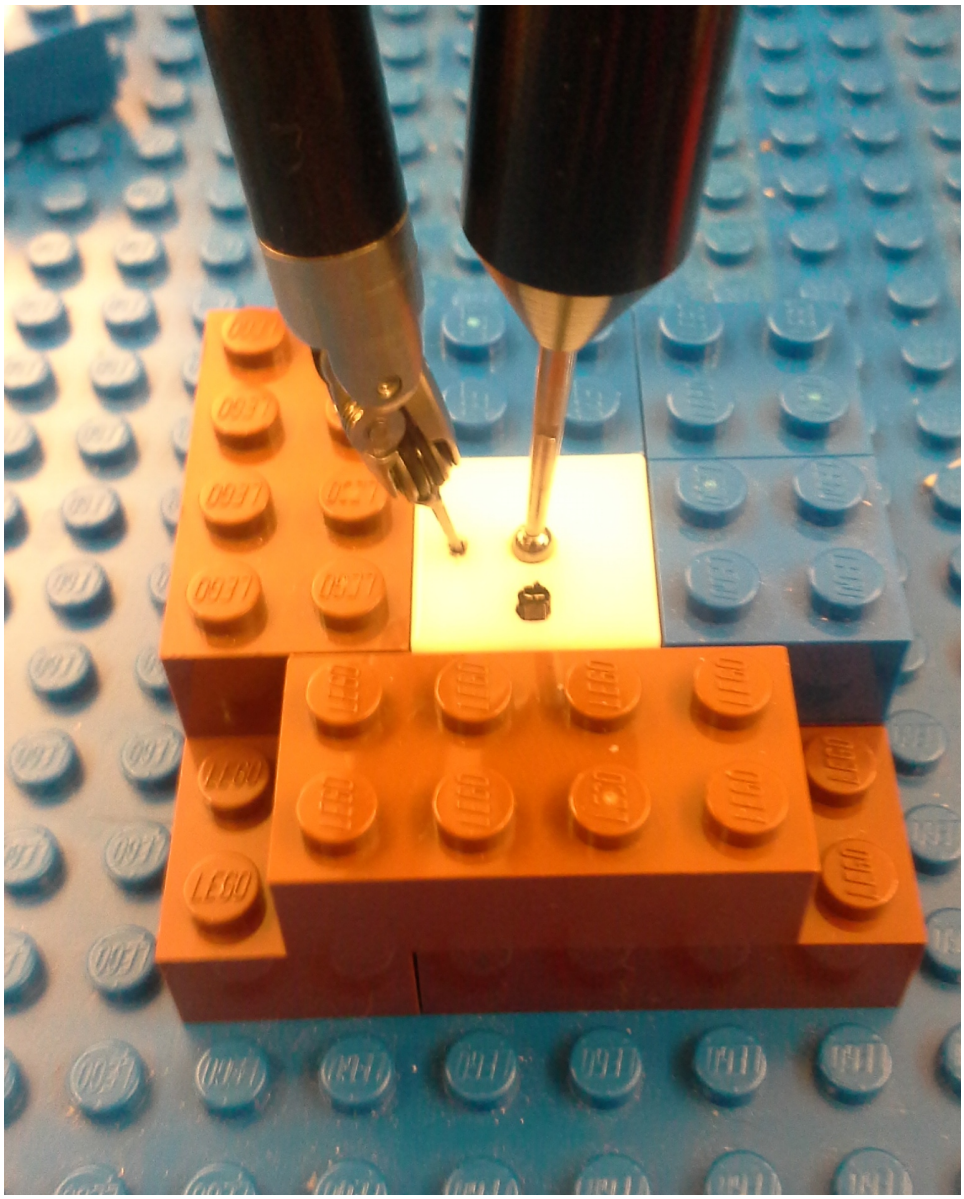

Figure A.1: An image of the experimental setup. The OptoTrak stylus was placed in a divot in the center of the custom Lego, while the Micro Forceps were placed in a divot to the left.

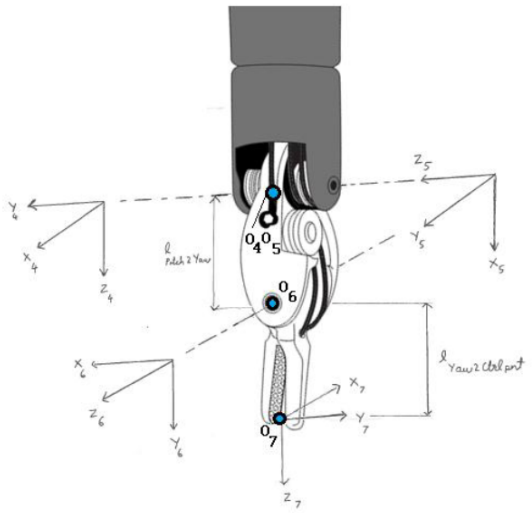

Figure A.2: A sketch of the tip of a da Vinci Instrument and the transforms that describe the transforms that describe the orientation of the tool. The control point is located at $O6$. This image is taken from the DVRK user guide.

16cm $\times$ 6.3cm $\times$ 2cm which mimics the general workspace of the robot. At each location, the tool tip was placed in the divot five times. The OptoTrak stylus was placed into the semi-circular divot three times.

The mean location for both the DVRK locations and OptoTrak were calculated and used in future registrations. The Target Localization Error (TLE) was calculated as the Cartesian distance between the mean location for each Lego location and each of the points for that location. Outliers were defined to be points that lay more than 2.5 mm from the mean location of each target. These points were discarded and mean location of each target was recalculated with the remaining points. Let it be noted that only 2 points were removed out of the 180 collected points from the calculations.

The OptoTrak points and the dVRK points were then registered. The OptoTrak points are used as ground truth in this registration. 50 registrations were completed using Horns method [65]. For each registration 30 of the 36 points were used as input, and then the remaining 6 points were used as testing data. The 36 Lego

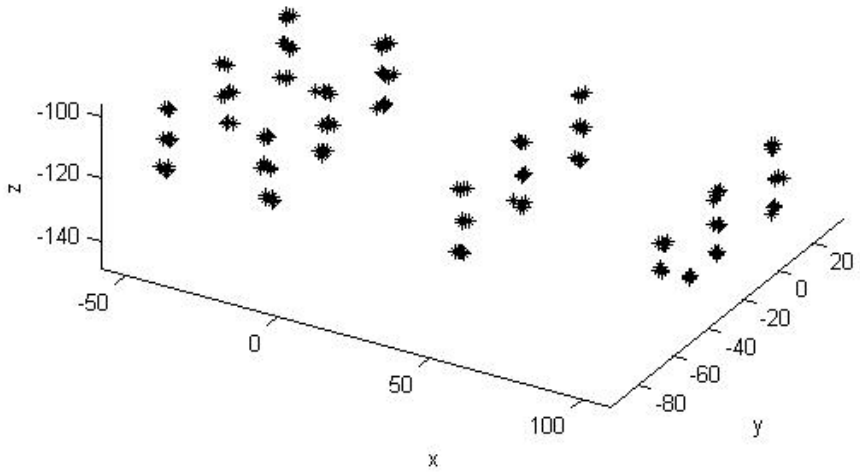

Figure A.3: Point distributions of the locations defined by the DVRK.

locations are randomly assigned to the training or testing data for each round of registration.

dVRK Accuracy Results and Discussion:

The resulting TLE for each location in the dVRK and the OptoTrak is shown in Table A.1 and A.2. An example of the points from the dVRK is shown in Figure A.3. The variance in the locations of the OptoTrak points was very small, with a mean TLE of 0.085 mm.

The mean and standard deviation of the training and testing data for these 50 registrations is shown in Table A.3. The error is defined as the mean Cartesian distance between the OptoTrak point and the resulting dVRK location. These are averaged over the 30 training points or 6 testing points and then averaged over the 50 registration rounds. Figure 2.4 shows the average resulting registration. The

Table A.1: TLE for Lego locations 1-10

	Mean and Standard Deviation of TLE	
Target Number	dVRK Targets	OptoTrak Targets
1	0.71 ± 0.30	0.127 ± 0.035
2	1.21 ± 0.31	0.123 ± 0.051
3	1.29 ± 0.73	0.113 ± 0.064
4	1.12 ± 0.73	0.309 ± 0.138
5	1.10 ± 0.58	0.146 ± 0.062
6	0.54 ± 0.17	0.055 ± 0.013
7	1.09 ± 0.73	0.031 ± 0.023
8	1.48 ± 0.46	0.088 ± 0.038
9	1.02 ± 0.23	0.055 ± 0.022
10	1.01 ± 0.51	0.128 ± 0.051

transform from each of the 50 registration rounds was saved and then averaged using dual quaternions [78]. The red stars in Figure A.4 represent the Lego locations defined by the OptoTrak and the black diamonds represent the DVRK locations after being multiplied by this average transform.

We have completed a test of the dVRKs precision and accuracy when compared to the OptoTrak motion capture system. Using Legos as repeatable and stable localization platform, we showed that the errors in the dVRK are on par with those described by Kwartowitz et al. [89] and with other tracking systems used within a surgical environment. Kwartowitz reports that the Standard robot has a mean TLE of 1.31 mm and 1.35 mm using two calculation methods. They also report an expected localization error of 1.02 mm, assuming infinite number of localization trials. In an update, Kwartowitz updates the results for the S robot [90]. The S robot has an updated robot structure and they report an expected localization error of 1.05 mm, which is not significantly different than what was found for the original system.

Using 36 points and 5 repetitions, we found a mean TLE of 1.16 mm. When registering the DVRK data to the OptoTrak mean TRE of 1.24 mm for the testing data was calculated. This is very similar to what has been found in previous ex-

Table A.2: TLE for Lego locations 11-36

11	1.32 ± 0.66	0.056 ± 0.021
12	1.00 ± 0.65	0.019 ± 0.011
13	1.61 ± 0.80	0.093 ± 0.048
14	0.56 ± 0.22	0.080 ± 0.034
15	0.90 ± 0.33	0.108 ± 0.031
16	1.25 ± 0.27	0.118 ± 0.043
17	0.94 ± 0.39	0.075 ± 0.024
18	1.46 ± 0.69	0.082 ± 0.029
19	1.61 ± 0.41	0.070 ± 0.023
20	1.59 ± 0.20	0.131 ± 0.045
21	0.67 ± 0.28	0.106 ± 0.057
22	1.61 ± 0.78	0.104 ± 0.040
23	1.26 ± 0.68	0.098 ± 0.050
24	1.54 ± 0.69	0.109 ± 0.058
25	1.27 ± 0.35	0.046 ± 0.022
26	1.38 ± 0.55	0.029 ± 0.019
27	1.39 ± 0.41	0.077 ± 0.048
28	0.85 ± 0.29	0.083 ± 0.019
29	1.43 ± 0.62	0.042 ± 0.005
30	0.87 ± 0.55	0.038 ± 0.002
31	0.96 ± 0.32	0.065 ± 0.027
32	1.36 ± 0.52	0.055 ± 0.017
33	1.25 ± 0.17	0.054 ± 0.032
34	0.90 ± 0.20	0.063 ± 0.028
35	1.09 ± 0.40	0.073 ± 0.033
36	1.17 ± 0.41	0.019 ± 0.007
	Mean	Mean
	1.16 ± 0.46	0.085 ± 0.035

Table A.3: The mean and standard deviation of the training and testing data for these 50 registrations

Size of Training data	Results of Training Data	Size of Test Data	Results of Test Data
30	1.18 ± 0.51	6	1.24 ± 0.52

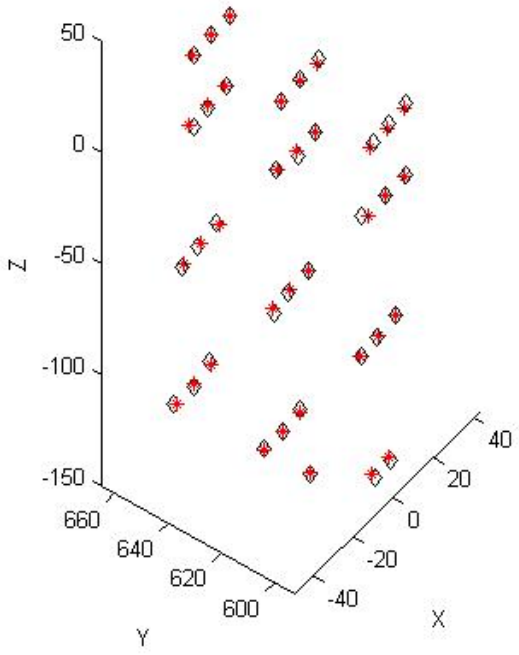

Figure A.4: Resulting registration, in the OptoTrak coordinate frame. The red stars represent the Lego locations defined by the OptoTrak and the black diamonds represent the DVRK locations after being multiplied by this average transform.

periments. The additional points collected in this experiment could have led to the smaller TLE.

The control point that is reported by the DVRK, and located near the pitch and yaw joints of the tool. The offset between the control point and the tool tip, which is most often the location that desired, can be found from the geometry of any tool with that general joint kinematics.

Because of the distance between the control point and the tool tip there is some

lever arm effect. This will increase the error of the calculated tool tip location. Most of the da Vinci tools that use this style kinematics and thus the estimated errors found here can be applied to other tools such as the Large Needle Driver, a commonly used tool for both research and clinical purposes.

A.2 Individual Model Fitting Results

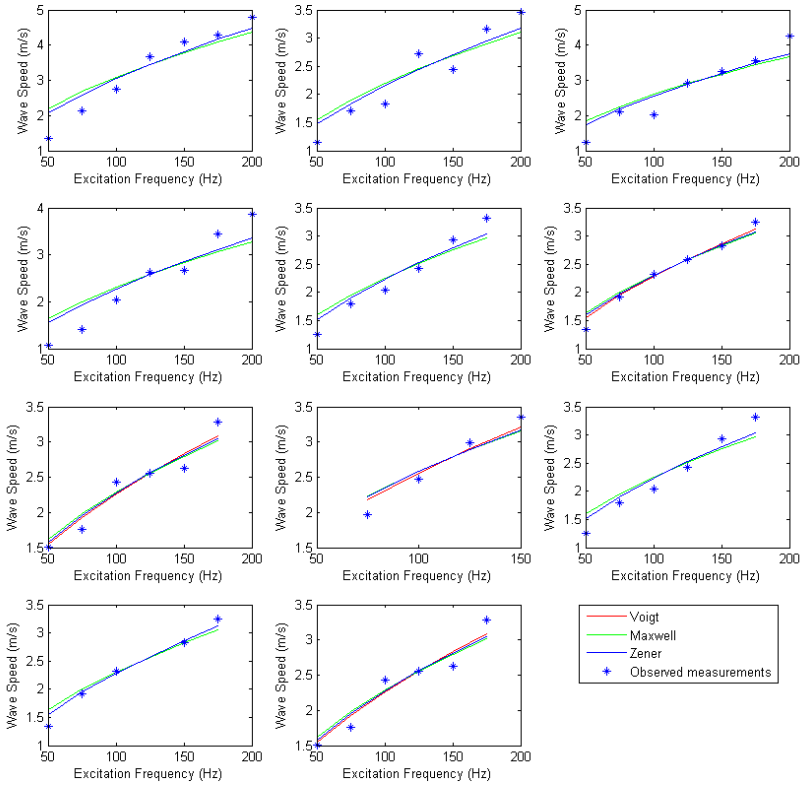

Figure A.5: Individual model fitting results for each of the *ex-vivo* kidneys used in the study.

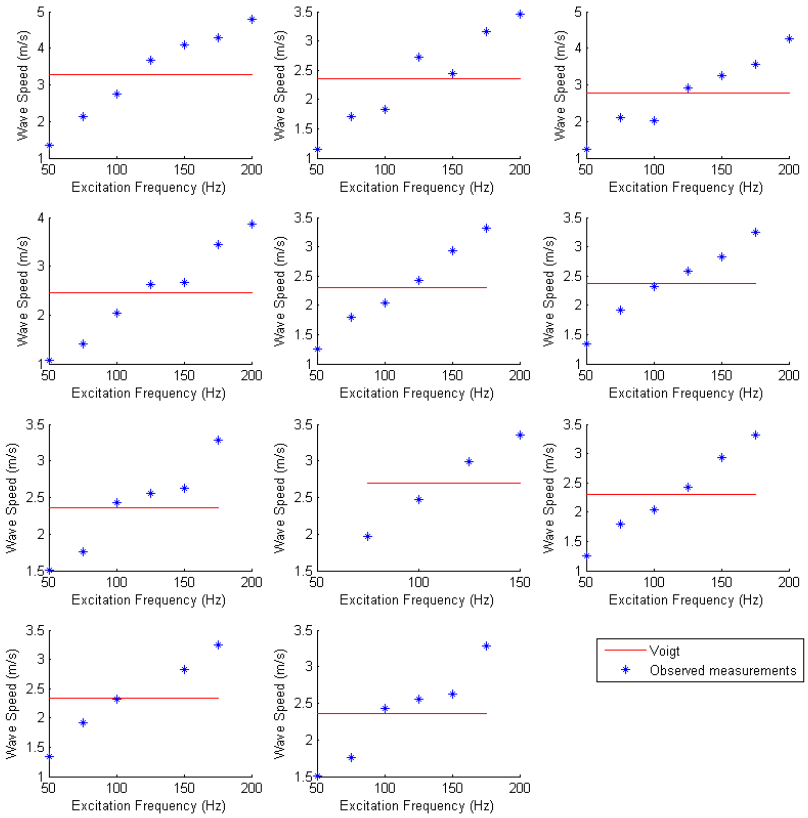

Figure A.6: Individual model fitting results for each of the *ex-vivo* kidneys used in the study when viscous components are set to zero.

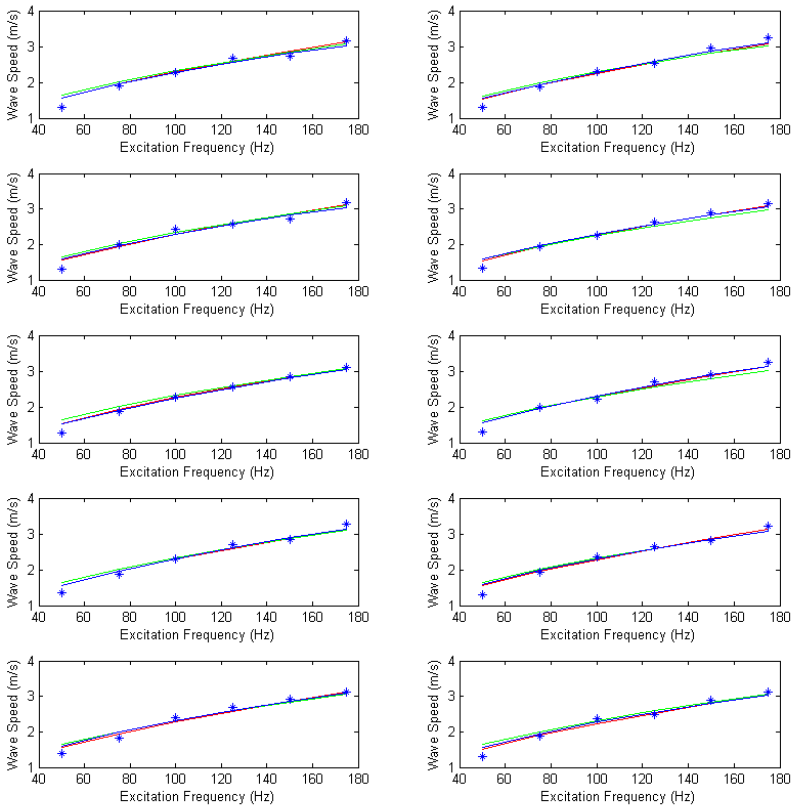

Figure A.7: Individual model fitting results for each 10 perturbation trials.

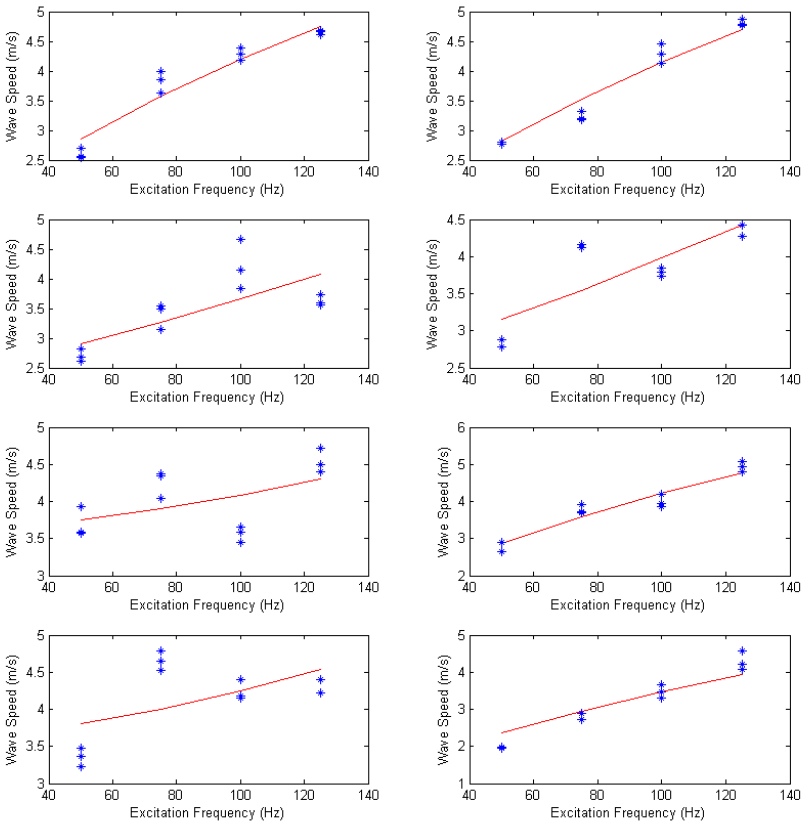

Figure A.8: Individual model fitting results for each patient in the study (First 8).

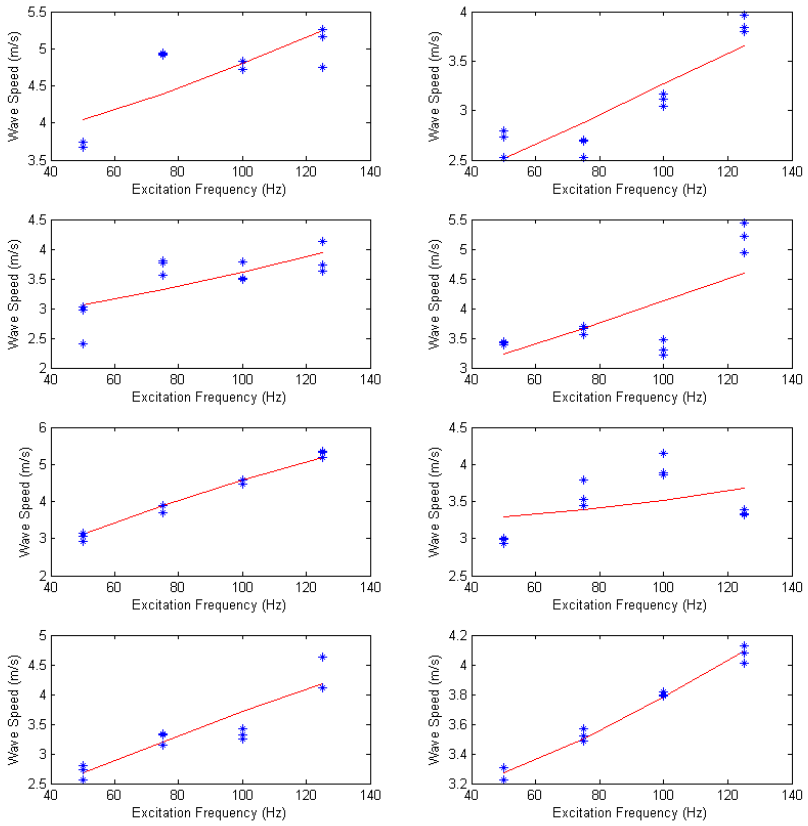

Figure A.9: Individual model fitting results for each patient in the study (Second 8).